


November 2017

## **Solution-Based Assembly of Conjugated Polymers into Nanofibers for Organic Electronics**

Daniel E. Acevedo Cartagena  
*University of Massachusetts Amherst*

Follow this and additional works at: [https://scholarworks.umass.edu/dissertations\\_2](https://scholarworks.umass.edu/dissertations_2)

 Part of the [Nanoscience and Nanotechnology Commons](#), [Polymer and Organic Materials Commons](#), and the [Semiconductor and Optical Materials Commons](#)

---

### **Recommended Citation**

Acevedo Cartagena, Daniel E., "Solution-Based Assembly of Conjugated Polymers into Nanofibers for Organic Electronics" (2017). *Doctoral Dissertations*. 1046.  
[https://scholarworks.umass.edu/dissertations\\_2/1046](https://scholarworks.umass.edu/dissertations_2/1046)

This Open Access Dissertation is brought to you for free and open access by the Dissertations and Theses at ScholarWorks@UMass Amherst. It has been accepted for inclusion in Doctoral Dissertations by an authorized administrator of ScholarWorks@UMass Amherst. For more information, please contact [scholarworks@library.umass.edu](mailto:scholarworks@library.umass.edu).

**SOLUTION-BASED ASSEMBLY OF CONJUGATED POLYMERS INTO NANOFIBERS  
FOR ORGANIC ELECTRONICS**

A Dissertation Presented

by

DANIEL ENRIQUE ACEVEDO CARTAGENA

Submitted to the Graduate School of the  
University of Massachusetts Amherst in partial fulfillment  
of the requirements for the degree of

DOCTOR OF PHILOSOPHY

September 2017

Department of Polymer Science and Engineering

© Copyright by Daniel Enrique Acevedo Cartagena 2017

All Rights Reserved

**SOLUTION-BASED ASSEMBLY OF CONJUGATED POLYMERS INTO NANOFIBERS  
FOR ORGANIC ELECTRONICS**

A Dissertation Presented

by

DANIEL ENRIQUE ACEVEDO CARTAGENA

Approved as to style and content by:

---

Ryan C. Hayward, Chair

---

Todd Emrick, Member

---

Michael Barnes, Member

---

E. Bryan Coughlin, Department Head  
Department of Polymer Science and Engineering

## **DEDICATION**

To my wife, Lisa A. Hernandez-Alicea for her unconditional love and support.

## ACKNOWLEDGMENTS

I am extremely grateful for all the great minds that helped me achieved this huge milestone in my career and shaped me into a better person, without these people all my achievements would not have been possible.

Special thanks to my advisor and mentor Professor Ryan C. Hayward, who believed in me from start. Professor Hayward motivated me to incessantly search for evidence to prove/refute a hypothesis and helped me become a critical thinker. With his guidance and patience, I could conduct research that passionate me, present my work in national conferences and undergo in international research endeavors. I am also thankful for my thesis committee, Professor Todd Emrick and Professor Michael Barnes, both of whom helped me achieved my PhD by providing constructive feedback in my projects. I would like to thank the faculty in the Polymer Science and Engineering department for providing me the fundamental tools to understand and conduct polymer science and engineering. The Class of 2011 became my family that year, thus thanks for welcoming me and helping me with my struggles in class.

I am greatly thankful for my collaborators. Firstly, Professor Alejandro Briseño for allowing me to fabricate graphene and making the characterization of my transistors possible. Also, Professor Briseño, I greatly enjoyed sharing ideas with you and appreciate your unconditional support in my professional career. A major roadblock in one of my projects was solved by Professor Stephen Nonnenmann and Jiaxin Zhu milestone. Infinite thanks for teaching me atomic force microscopy like no other. In 2015, I traveled to South Korea and worked with Professor Kilwon Cho. Thanks for hosting me in your group, Professor Cho, during the summer and teaching me about x-ray absorption and solar cells. Special thanks to Jinsung Kim for being my buddy during that summer. Also, Professor Cho made my experiments at the Pohang Accelerator Laboratory (PAL) possible. At PAL, I got to collaborate with a great scientist and friend, and now Ph.D., Dr. Hyeongjun Kim. Thanks for helping me with the experiments at PAL

and for making P3HT research fun. In the final stages of my PhD, I had the pleasure of working with Aditi Naik. Thanks to her talent in fabricating graphene electrodes we could construct transistors from the first attempt. This last portion of my work would not have been possible without Dr. David Leonardo Gonzalez (Leo). Thanks to Leo's creativity, the graphene research resulted into a workable transistor.

Throughout my PhD I had the pleasure of being a mentor for multiple undergraduate students Matt Gurney, Elvira Travanino and Cyprian Gyamfi. I am grateful for working smart and talented people in the Hayward Research Group. It was fun. Specially, Nakul Bende for always having an advice on how to make things better and Felicia Bokel for building and teaching me the essentials of my project.

I own much of my professional development to my mentor Dr. Anesia Auguste. Anesia will always be an inspiration for me. Also, my professional career was greatly enhanced by the great people at the Office of Professional Development and Corning Incorporated. Infinite amount of thanks to my mentors from Corning, Manuela Ocampo and Boh Ruffin. Gregory Thomas and Professor Sandra Petersen (Sandy) made the UMass/Corning Mentoring Program possible. I enormously treasure the way you helped grow professionally. One of the main reasons for me to come to UMass is the welcoming family environment that I found. Thanks to Sandy and Shana Passonno's resourcefulness, we always found a solution to my problems. Transitions into new careers are always challenging, and there was no one better than Alysia Birkholz to help ease me through them and become successful in finding the right alternatives.

A huge deal of thanks go to my family in Puerto Rico for letting me fly away from home to pursue my dreams; specially to my mother, Dalma E. Cartagena, for planting a growing piece wisdom that kept me warm during cold times. I greatly appreciate my friends' support through the good and challenging times inside and outside of work: Marcos Reyes, Madhura Pawar, Edwin Murenzi, Amilcar Gonzalez, Jose Alvarez and Bryan Salas.

Above all, I owe an immeasurable and indescribable amount of thanks to my wife and best of everything, Lisa, for your unconditional love and support. Thank you for making this possible.



## ABSTRACT

### SOLUTION-BASED ASSEMBLY OF CONJUGATED POLYMERS INTO NANOFIBERS FOR ORGANIC ELECTRONICS

SEPTEMBER 2017

DANIEL ENRIQUE ACEVEDO CARTAGENA, B.S., UNIVERSITY OF PUERTO RICO  
MAYAGUEZ

M.S., UNIVERSITY OF MASSACHUSETTS AMHERST

Ph.D., UNIVERSITY OF MASSACHUSETTS AMHERST

Directed by: Professor Ryan C. Hayward

Solution-based crystallization of conjugated polymers offers a scalable and attractive route to develop hierarchical structures for electronic devices. The introduction of well-defined nucleation sites into metastable solutions provides a way to regulate the crystallization behavior, and therefore the morphology of the material. A crystallization method for generating metastable solutions of poly(3-hexylthiophene) (P3HT) was established. These metastable solutions allow P3HT to selectively crystallize into nanofibers (NFs) on graphene-coated surfaces. It was found that the crystallization kinetics is faster with increasing P3HT molecular weight and concentration. Through *in situ* atomic force microscopy, it was confirmed that NFs grow vertically in a face-on chain orientation (*i.e.*, the  $\pi$  orbitals parallel to the substrate normal) from highly oriented pyrolytic graphite and graphene. Moreover, the P3HT crystal structure observed on the surface of graphene was identified to be the same one formed by solution crystallization. However, as confirmed by X-ray scattering and scanning electron microscopy the crystals transitioned from face-on to edge-on orientation (*i.e.*, the  $\pi$  orbitals perpendicular to the substrate normal) as the film grew thicker. As determined by X-ray scattering, the initial face-on conformation was partially preserved by embedding the P3HT structures in an indene C<sub>60</sub> bisadduct matrix when compared to pristine P3HT films. The resulting organic field effect transistors had hole mobilities ( $\mu = 20 \times 10^{-3} \text{ cm}^2 \text{ V}^{-1} \text{ s}^{-1}$ ) two orders of magnitude higher than the

devices fabricated from spin casted P3HT ( $\mu = 0.9 \times 10^{-3} \text{ cm}^2 \text{ V}^{-1} \text{ s}^{-1}$ ). The solution-processable fabrication of electrodes and semiconductors is potentially scalable and amenable to roll-to-roll manufacturing.

## TABLE OF CONTENTS

	Page
ACKNOWLEDGMENTS .....	v
ABSTRACT.....	viii
LIST OF TABLES.....	xii
LIST OF FIGURES .....	xiii
CHAPTER	
1. BACKGROUND .....	1
1.1 Motivation.....	1
1.2 Morphology considerations the performance of organic electronics .....	2
2. CRYSTALLIZATION OF P3HT NANOFIBERS FROM GRAPHENE SURFACES .....	6
2.1 Abstract.....	6
2.2 Introduction.....	7
2.3 Material fabrication.....	10
2.3.1 Poly(3-hexyl thiophene) (P3HT) synthesis.....	10
2.3.2 Graphene fabrication.....	10
2.4 Results and discussion .....	13
2.4.1 Stability of supersaturated solutions of P3HT .....	13
2.4.2 Nanofiber formation on multilayer graphene.....	16
2.4.3 Effects of the underlying substrate on the formation of P3HT nanofibers .....	23
2.4.4 Seeded Crystallization .....	28
2.5 Conclusions.....	33
3. FORMATION MECHANISM OF P3HT NANOFIBERS CRYSTALLIZED FROM GRAPHENE.....	35
3.1 Abstract.....	35
3.2 Introduction.....	36
3.3 Experimental procedures .....	38
3.3.1 Synthesis of poly(3-hexyl thiophene) .....	38
3.3.2 Crystallization experiments .....	40
3.3.3 Absorption coefficient of P3HT nanofibers.....	41
3.4 Results and discussion .....	43

3.4.1 Hysteresis in the crystallization of P3HT .....	43
3.4.2 Crystallization mechanism.....	47
3.4.3 Transition in the orientation of P3HT nanofibers .....	56
3.4.4 Alternative materials for graphene templated crystallization .....	64
3.5 Conclusions.....	71
4. SELECTIVE CRYSTALLIZATION OF P3HT NANOFIBERS FOR GRAPHENE-BASED ELECTRONICS.....	73
4.1 Abstract.....	73
4.2 Introduction.....	73
4.3 Experimental procedure.....	76
4.3.1 Materials .....	76
4.3.2 Film thickness growth.....	76
4.3.3 Graphene electrodes fabrication .....	76
4.3.4 Graphene fabrication.....	78
4.3.5 Transistor characterization.....	79
4.3.6 Selective crystallization .....	79
4.4 Results and discussion .....	80
4.4.1 Selective crystallization of P3HT for field effect transistors.....	80
4.3.2 Graphene as an electrode for photovoltaic cells .....	95
4.4 Conclusions.....	98
5. SUMMARY AND OUTLOOK.....	100
5.1 Crystallization of P3HT nanofibers from graphene surfaces.....	100
5.2 Formation mechanism of P3HT nanofibers crystallized from graphene .....	101
5.3 Selective crystallization of P3HT nanofibers for graphene-based electronics.....	102
BIBLIOGRAPHY .....	105

## LIST OF TABLES

Table	Page
1. Physical properties of the P3HT used in this study are listed below. The molecular weights given in polystyrene equivalent were measured by GPC and the regioregularity was determined from NMR. ....	38
2: Avrami parameters summary. ....	49
3: Electronic characteristics of P3HT films crystallized from BLG on MoO <sub>3</sub> . ....	59
4: Dichroic ratio values for the P3HT films. ....	61
5: Intensity ratios, obtained from GIWAXS, for the specified reflections of P3HT crystallized from graphene. ....	64
6. OFET properties as a function of crystallization time. The values represent an average of ten devices. ....	93
7: Averaged open circuit voltage ( $V_{oc}$ ), short circuit current ( $I_{sc}$ ), fill factor and power conversion efficiency (PCE) of 9 photovoltaic devices. ....	98

## LIST OF FIGURES

Figure	Page
1: Schematic of a cross-section of an organic photovoltaic cell (a). Typical chain configuration for poly(3-hexyl thiophene) (b). .....	3
2: Schematic illustrating the cross-section of a transistor with a bottom-gate bottom-contact architecture.....	4
3: Typical methods for crystallizing P3HT in solution. UV-vis spectra of dissolved P3HT (orange) and crystalline P3HT in solution (purple) (left). Transmission electron microscopy image of P3HT nanofibers (right).....	9
4: Graphene thickness. Typical optical profilometry measurement of graphene on ITO (a) and the thickness profile along indicated above (b). Raman spectrum of graphene transferred onto Si (c). .....	12
5: Determination of the mass absorption coefficients of the dissolved ( $\epsilon_a$ ) and crystalline ( $\epsilon_f$ ). Determination of $\epsilon_a$ using the absorbance at 454 nm for solutions of dissolved P3HT (a). UV-vis absorbance spectra of P3HT crystallized first at -5 °C and subsequently incubated at the indicated temperatures (b), along with UV-vis spectra following filtration to determine the remaining concentration of dissolved polymer $c_a$ after crystallization (c). Determination of $\epsilon_f$ from a plot of the absorbance at 602 nm of the crystallized solutions against $c_a$ (d).....	15
6: The hysteresis between crystallization and melting of P3HT NFs. UV-vis spectra of 0.50 mg/mL solution of P3HT in <i>m</i> -xylene during (a) cooling and (b) heating, along with (c) the temperature profile employed (the sample was held for at least 10 min at each temperature), and (d) the degree of aggregation $x_f$ measured during the temperature cycle. ....	16
7: Selective crystallization of NFs from different MLG coated substrates. UV-vis absorbance spectra of P3HT films grown on MLG on ITO at different times of incubation in a metastable solution of P3HT (a). The inset shows a photograph of a film of P3HT NFs grown for 120 h on ITO coated with MLG only on the right side. Thicknesses of P3HT films as function of incubation time determined by AFM for MLG on Si (red) and HOPG (black), and by optical profilometry for MLG on ITO (green) (b). Error bars represent one standard deviation based on 10 measurements. SEM images of the interface between MLG-coated regions (top) and the bare substrate (bottom) after 24 h of growth using ITO (c) and Si (d) substrates. Scale bars: 200 nm. ....	18
8: AFM images of the Si/graphene interface with P3HT grown for 24h along with the thickness profile along the indicated black line, across a single NF. ....	18
9: Determination of $\epsilon_s$ from a plot of absorbance at 602 nm of solid films against measured thickness (a). Normalized absorbance spectra of P3HT NFs in solution (black) and in a film (red) (b). ....	20

10: Normalized UV-vis absorbance spectra of metastable solutions of P3HT incubated with graphene coated ITO substrates at room temperature for the lengths of time indicated in the legend. The curves are offset vertically for clarity. ....	20
11: SEM images of P3HT films formed from a 0.5mg/mL solution by drop casting (a) on HOPG and spin casting on graphene coated Si (b). The images observed are like those for the respective bare substrates. Scale bar: 100 nm. ....	22
12: AFM images of MLG deposited on Si (a), and following crystallization of P3HT for 30 min (b), 1 h (c), 3 h (d), 6 h (e), 24 h (f), 72 h (g), and 120 h (h), along with the respective thickness profiles along the indicated black lines. ....	23
13: AFM images of P3HT crystallization on HOPG for 1 h (a), 3 h (b), 24 h (c), 79 h (d), and 120 h (e), along with the respective thickness profiles along the indicated black lines.....	23
14: SEM images of P3HT crystallized from a metastable solution on different substrates HOPG for 5 min (a) and 3 h (b); MLG on Si for 0.5 h (c) and 3 h (d); MLG on ITO for 3 h and (e) 24 h. (g) Scale bar = 100 nm. The inset in (c) shows an individual short NF.....	25
15: SEM images of P3HT NFs grown from a metastable solution from 120 h on MLG .....	26
16: Schematic illustration of nanofibers grown in solution before (left) and after (right) removing the substrate from the fluid, with their respective chain orientations.....	26
17: AFM images taken during solution crystallization of a 0.5 mg/mL solution of P3HT-12k from HOPG (a) and with their respective line profiles (b). In-plane orientation angle of the lateral long axis of the NF with respect of an arbitrary angle of the HOPG surface (c).....	27
18: TEM images of P3HT NFs in m-xylene .....	29
19: Seeded crystallization kinetics as characterized by UV-vis of unimers. incubated with different amount of seeds in solution for 6days: 8% (a), 14% (b), and 24% (c) out of the total P3HT in solution seeded crystallization.....	31
20: NF fraction as function of time. Unimers (a). incubated with different amount of seeds in solution for 6days: 8%, 14%, and 24% out of the total P3HT in solution .....	32
21: TEM images of P3HT seeds initially (a). Different amount of seeds incubated with the same amount of unimers in solution for 6days: 8% (b), 14% (c), and 24% (d) seeds out of the total P3HT in solution.....	32
22: P3HT-b-P3TEGT (1.85:1, $M_n = 18$ kg/mol) NFs formed in a chlorobenze:methanol (4:1) solution at 1mg/mL before (a) and after (b) sonication for 3 h at 5 °C. ....	33

23: GPC traces obtained using tetrahydrofuran at room temperature (a) and tri-chlorobenzene at 140 °C (b). The background signal was subtracted for better visualization of the traces. ....	39
24: NMR spectra of P3HT with different regioregularity.....	39
25. P3HT crystallized on a graphene flake. ....	41
26: UV-vis of P3HT crystallized for different at different period of times (a) and after filtration (b). ....	42
27: Calibration curves of dissolved (a) and crystallized P3HT in <i>m</i> -xylene (b). ....	43
28: Melting ( $T_m$ ) and crystallization ( $T_c$ ) temperatures with the corresponding hysteresis window ( $T_m - T_c$ ) of highly regioregular P3HT(a). Correlation between the hysteresis window chain folding by comparing the fiber width against the polymer contour length as function of molecular weight (b). The chain contour length was determined from the corrected molecular weight by dividing the overestimated GPC molecular weight by 1.7. <sup>71,99</sup> .....	45
29: TEM images of P3HT with different molecular weights measured in polystyrene equivalent: 6 kg/mol (a), 10 kg/mol (b), 12 kg/mol (c), 22 kg/mol (d), crystallized at their respective crystallization temperatures when cooled at 1 °C/min from 80°C. ....	46
30: Melting point and hysteresis window as a function of regioregularity (a) and concentration (b) of P3HT.....	47
31: Kinetics of crystallization of pristine P3HT at 0.5 mg/mL as characterized by UV-vis spectroscopy and upon addition of graphene flakes (a). Crystallization kinetics fitted to the Avrami model (b). ....	49
32: P3HT crystallizing on HOPG as characterized by AFM <i>in situ</i> and visualized using the height channel (a) and the amplitude channel (b). The segmented lines indicate the interchain distance (16 Å) in along the <i>a</i> axis. An amplitude profile from the rectangular area on (b) shows the steps on the NFs (c).....	51
33: P3HT ( $M_n = 23$ kg/mol) crystallizing on HOPG as characterized by AFM <i>in situ</i> and visualized using the height channel (a) and the amplitude channel (b).....	53
34: Phase channel of <i>in situ</i> AFM showing P3HT chains on the surface of a nanofiber nucleus (a) with the phase contrast profile obtained from the rectangular area averaged between red lines (b) as illustrated on (a). ....	54
35: <i>In situ</i> AFM illustrating P3HT nucleus forming on HOPG from an ordered monolayer domain (a) into a nanofiber nucleus (b). ....	55
36: Raman spectroscopy spectrum of BLG deposited on glass substrate pre-coated with MoO <sub>3</sub> /ITO (a). UV-vis spectrum of BLG deposited on graphene (b). ....	57



37: AFM images of BLG as transferred on a silicon oxide substrate (a); MoO <sub>3</sub> exposed surface (b) and BLG after 72 h of incubation in a P3HT solution (c). UV-vis absorbance of P3HT crystallized from BLG on MoO <sub>3</sub> to different extends (d). .....	58
38: UPS spectra of P3HT crystallized from BLG on MoO <sub>3</sub> at the secondary electron cutoff region (a) and their respective valance bands (b). Schematic representation of the energy levels of the different layers of the sample (c).....	59
39: Spectra obtained from NEXAFS operated on partial electron yield mode of BLG on MoO <sub>3</sub> (a); P3HT crystallized for 1 h (b), 24 h (c) and 72 h (d). Linear fittings of the 1s → π* C=C resonance intensity as a function of incident angle (e). .....	61
40: 2D GIWAXS measurements of P3HT films crystallized for 6 days from graphene on Si as prepared (a) and embedded in a ICBA matrix during solvent evaporation (b) with their respective spectra along the out-of-plane (b, e) and the in-plane directions (c, f). .....	63
41: 2D GIWAXS measurements of P3HT films crystallized for 6 days from graphene on Si with a ICBM layer on top prepared with the spectra along the out-of-plane (b) and the in-plane directions (c). .....	63
42: The hysteresis between crystallization and melting of PBTTT NFs. UV-vis spectra of 0.05 mg/mL solution of PBTTT in ODCB during cooling and (a) heating (b), along with the temperature profile employed (c), and absorbance of aggregated PBTTT at 600 nm (d).....	66
43: PBTTT crystallizing on HOPG as characterized by AFM <i>in situ</i> and visualized using the height channel (a) and the phase channel (b). In-plane orientation angle of the lateral long axis of the NF with respect of an arbitrary angle of the HOPG surface (c).....	68
44: High-resolution AFM characterization <i>in situ</i> of PBTTT NFs crystallizing on HOPG and visualized using the height channel (a) and the phase channel (b).....	70
45: High-resolution AFM characterization <i>in situ</i> of PBTTT crystallizing on HOPG into organized domains visualized using the height channel (a) and the phase channel (b).....	70
46: SEM image of PBTTT crystallized from graphene on ITO (a) in a 0.05 mg/mL metastable solution of ODCB for 24 h. GIWAXS out-of-plane cut of PBTTT crystallized from graphene on Si (b). The inset in (a) shows the film selectively crystallized on graphene.....	71
47: AFM of graphene electrodes.....	78
48: Schematic illustrating the cross-section of a transistor with a bottom-gate bottom-contact architecture used in this study.....	79
49: P3HT crystallizing on graphene electrodes as characterized by AFM <i>in situ</i> and visualized using the amplitude channel (top) and the height channel (bottom). .....	80

50: Kinetics of P3HT crystallized on HOPG into films from solution at low molecular ( $M_n = 12$ kg/mol) weight and high molecular weight ( $M_n = 22$ kg/mol) (a). The effects of concentration on high molecular weight P3HT crystallized from HOPG (b). The reported thickness and standard error values were measured by AFM.....	83
51: <i>In situ</i> AFM showing the formation of nuclei of P3HT NFs on the surface of graphene electrodes at 198 min (a) and 200 min (b) during the exposure to the P3HT metastable solution.....	85
52: Imprinted graphene electrodes on SiO <sub>2</sub> wafers incubated in metastable (2 mg/mL) P3HT solutions for 5 min (a), 10 min (b) and 15 min (c), with their respective bare silicon wafers (d-f) exposed to the same conditions.....	86
53: AFM of bare SiO <sub>2</sub> substrates exposed to metastable P3HT solutions (2 mg/mL) for 5 min (a), 10 min and (b) 15 min (c).....	87
54: SEM showing the P3HT morphology on graphene electrodes when crystallized for 5 min (a), 10 min (b), 15 min (c). The NF morphology is shown from the area depicted by the green rectangle on the right of (c).....	89
55: SEM showing the P3HT morphology in the channel of a set of graphene electrodes as spin casted from a <i>m</i> -xylene (2 mg/mL) solution.....	90
56: Formation kinetics of P3HT NFs crystallized from graphene flakes spin casted on glass (a) as characterized by UV-vis spectroscopy. Film thickness of P3HT as characterized by optical profilometry (b).....	91
57: Transfer characteristics of OFET of P3HT spin casted (a), and crystallized for different crystallization periods: 5 min (b), 10 min (c), 15 min (d) on graphene electrodes. A $V_{DS} = -100$ V was applied to all devices with a bottom-gate and bottom-contact geometry on a SiO <sub>2</sub> /Si wafer.....	93
58: OFET output characteristics of P3HT spin casted (a) and crystallized for different times in a supersaturated solution for 5 min (b), 10 min (c) and 15 min (d) on graphene electrodes. The gate voltage was varied from 40 V to -100 V in 10 V steps.....	94
59: Hysteresis behavior in the devices prepared from P3HT spin casted (a) and P3HT crystallized for different times in a supersaturated solution for 5 min (a), 10 min (b) and 15 min (c) on graphene electrodes. A $V_{DS} = -100$ V was applied to all devices with a bottom-gate and bottom-contact geometry on a SiO <sub>2</sub> /Si wafer.....	95
60: Schematic illustrating a typical OPV cell using a graphene based anode with a P3HT:PCBM (1:1) mixture as active layer (a) with its respective I-V curve (b).....	98
61: Schematic illustrating the architecture of an OPV cell based on a bilayer active film that uses graphene as a hole extraction layer to template for P3HT NFs.....	98

# CHAPTER 1

## BACKGROUND

### 1.1 Motivation

Increasing concern about the detrimental effects of burning fossil fuels on human health and on the environment, have led to the necessity of developing inexpensive and cleaner energy alternatives with more efficient electronic devices. The Sun is a vast source of energy. In 2011 Jacob and coworkers calculated that 6,500 trillion watts (TW) are available for energy harvesting from the sun, while at the same time 12.5 TW are required to satisfy global energy demands.<sup>1</sup> However, the United State Department of Energy (DoE) reported that for the same year only 0.05% of the total electricity production was based on solar energy. In response to this situation the DoE created the SunShot Initiative, which has made the electricity produced from solar energy cost-competitive (\$0.06 per kilowatt-hour) with other non-renewable forms of electricity. By 2020 SunShot aims to reduce it to \$0.04 per kilowatt-hour by 2030.

Currently, the electronic market is led by silicon-based technology. Single crystal silicon panels can reach a power conversion efficiency (PCE) of 25.6%,<sup>2</sup> yet their efficiency has plateaued over the past decade according to the most recent report of the Best-Research Cell Efficiency from the National Renewable Energy Laboratory report. However, electricity produced from solar energy remains more expensive than non-renewable sources (\$ 0.04 per kilowatt-hour)<sup>3</sup>. Interestingly, the Shockley–Queisser caps the PCE of a single p-n junction to 30%<sup>4</sup>. The promise of low cost production and large-scale availability offered by organic photovoltaics makes them a potentially transformative platform for affordable solar energy conversion.<sup>2,5–10</sup> Although overwhelming research progress have allowed the PCE of these organic solar cells to achieve values up to 11.2%,<sup>11</sup> further investigation is required to fully optimize the device performance. Morphology within the active layer of solar cells plays a key

role in device performance.<sup>12</sup> Despite the overwhelming advances in optimizing the morphology, an optimum morphology has not been fabricated and the principles that govern these processes are still in early stages.<sup>13,14</sup>

Another major concern is the efficient usage of the electric current generated. From its invention in 1947, the transistor has revolutionized the field of electronic devices due to its ability to amplify signals by modulating the electric current. In principle, the lower operating voltage and higher charge mobility in a device, the better its performance. Silicon technology has achieved outstanding advances in increasing the performance electronic devices by doubling the number of transistors in integrated circuits, as postulated in Moore's Law.<sup>15</sup> Although polymers cannot substitute silicon based transistors, they represent a lower cost alternative given their ability to be processed at low temperature from solutions. It has been seen that the crystallinity increases in the performance of organic transistors. Therefore, it is important to better understand polymer crystallization and its effects on organic transistors.

This work focuses on controlling the morphology of conjugated polymers to assemble structures suitable for electronic devices, while offering insight of the principles behind it. More specifically, this work aims to control and orient the crystal growth of model donor-type conjugated polymer, poly(3-hexyl thiophene) (P3HT), into structures that would be suitable for photovoltaic cells and transistors.

## **1.2 Morphology considerations the performance of organic electronics**

Organic photovoltaic (OPV) cells commonly employ an easily processable blend of electron donor and acceptor materials in a heterojunction structure, which was patented by Sariciftci and Heeger to improve the performance of solar cells based on bilayer structures.<sup>16</sup> As seen in Figure 1, the active layer is located between electrodes, which are selected to match the molecular levels of the semiconductors at the top and bottom of the device, commonly composed

of transparent indium tin oxide (ITO) and aluminum (Al), respectively. The physical mechanism for charge generation in OPV cells has been the subject of a vast number of studies.<sup>17–22</sup> The accepted mechanism<sup>21</sup> consists of generating an excited state upon light absorption, charge separation and charge transport to the electrodes. In the formation of a localized excited state upon photon absorption, called Frankel exciton (i.e. bound electron–hole pair), the binding is higher than  $k_B T$  thus it requires the exciton to diffuse 10–20 nm to the interface to be separated into individual charge carriers before recombination.<sup>23</sup> Finally, the charge carriers require a continuous pathway that possesses high crystallinity to reach the respective electrode. This mechanism provides the guidelines to generate an optimal structure for device performance, which requires continuous, interpenetrating and highly crystalline nano-scale domains that allow efficient charge generation.<sup>12</sup> A cross-section of a interpenetrating structure of donor and acceptor materials is shown in Figure 1, where the pillars are on the order of 20 nm in diameter expanding all the way to the respective electrode, and a wetting layer on the respective electrode transport.

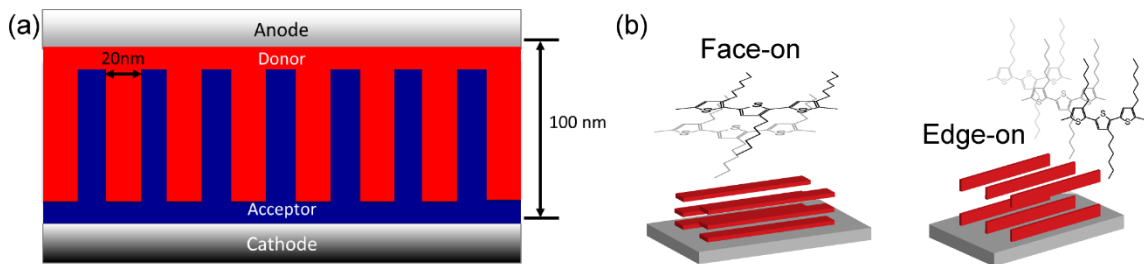


Figure 1: Schematic of a cross-section of an organic photovoltaic cell (a). Typical chain configuration for poly(3-hexyl thiophene) (b).

Attaining the proper direction of molecular orientation within device active layers can significantly improve charge mobility along the relevant direction (i.e., towards electrodes).<sup>20,24–26</sup> In conjugated polymers, high charge mobility is realized along the polymer chain backbone through its conjugation length, and through overlapping  $\pi$  orbitals between neighboring backbones of adjacent chains where the charges hop between chains, while charge transport is the minimum through the direction parallel to the alkyl chains.<sup>24</sup> Therefore, an edge-on orientation (with the  $\pi$  planes of the polymer

oriented perpendicular to the substrate, as seen on the right of Figure 1b) is beneficial for field effect transistors, which require good in-plane mobility,<sup>20</sup> while face-on orientation ( $\pi$  planes of the backbone parallel to the substrate, as seen on the left of Figure 1b) is sought to increase out-of-plane charge transport.<sup>25</sup>

To achieve control over the morphology, material considerations must be taken from the molecular level to the macroscopic scale. Through synthetic approaches the packing ability of the semiconductor have been modified to improve charge transport.<sup>27-30</sup> For example, block copolymers have been employed to segregate each block into well-defined structures.<sup>31-33</sup> However, these materials incorporate insulating components that hamper the final performance of the device, and the morphology of the material is highly dependent on the processing conditions.<sup>20,34</sup> Commonly thermal annealing is employed to modify the morphology after film deposition to enhance its crystallinity. Annealing blends of P3HT and phenyl-C61-butyric acid methyl ester (PC<sub>61</sub>BM) significantly improves the performance of the device by crystallizing the polymer into nanofibers (NFs).<sup>35</sup> It has been proposed that partial miscibility of PC<sub>61</sub>BM in amorphous P3HT prevent PC<sub>61</sub>BM crystallization, which establishes a delicate balance between temperature and time of annealing necessary for preventing macrophase separation.<sup>36</sup> A wide variety of studies have illustrated morphology modification during and after film casting employing solvent additives and solvent annealing, respectively.<sup>8,35,37</sup> However, reproducible morphological control with high degrees of crystallinity is necessary for the viability of these processes.<sup>8</sup>

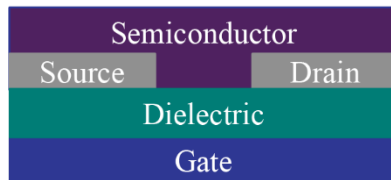


Figure 2: Schematic illustrating the cross-section of a transistor with a bottom-gate bottom-contact architecture.

As for OPV devices, organic field effect transistors (OFETs) based on P3HT benefit from highly crystalline films.<sup>38</sup> Figure 2 illustrates a typical architecture (e.g. bottom-gate bottom-contact architecture) for OFETs, where the source and the drain electrodes are buried in the semiconductor film. Essentially, an OFET operates as a capacitor. One of the plates is provided by the conductive channel formed in the organic semiconductor between two ohmic contacts (e.g. the source and drain electrodes). The density of carriers is modulated by the voltage applied in second plate called the gate electrode.

Not surprisingly, the processing technique chosen to fabricate OFETs affects the formation mechanism. As found by Sirringhaus<sup>20</sup> drop casted films showed mobilities up to one order of magnitude higher than spin casted films, due to a higher edge-on orientation content for the former when compared to the latter. In a separate study, Zhang and coworkers<sup>39</sup> systematically increased the molecular weight of P3HT to study the morphology impact on OFETs. It was found that the lateral width of the NF increases with molecular weight, which was correlated to an exponential increment in the mobility of the films. Albeit the mechanism behind this relation is not completely understood, these results confirm the importance of the morphology of the polymer for OFETs.

The following chapters describe a solution-based crystallization method, based on saturated solutions, to tailor the nanostructure of semiconducting polymers and deliver more efficient electronic devices such as transistor and solar cells. These supersaturated solutions crystallize selectively into NFs from nucleating agents such as graphene. Crystallization of NFs from graphene electrodes was established as a processing technique capable of increasing the charge transport by two orders of magnitude, when compared to more traditional spin casted films. Moreover, the P3HT crystal structure observed on the surface of graphene was identified to be the same one formed by crystallization in free solution.

## CHAPTER 2

### CRYSTALLIZATION OF P3HT NANOFIBERS FROM GRAPHENE SURFACES\*

#### 2.1 Abstract

We demonstrate that graphene surfaces provide highly selective nucleation of poly(3-hexyl thiophene) (P3HT) nanofibers (NFs) from supersaturated solutions. Solvent conditions are identified to give rise to a wide hysteresis between crystallization and melting, centered around room temperature, yielding metastable solutions that are stable against homogeneous nucleation for long periods of time but that allow for heterogeneous nucleation by nucleating agents. Selective growth of P3HT crystals is found for multilayer graphene (MLG) supported on either Si or ITO substrates, with nucleation kinetics that are more rapid for MLG on Si but slower in both cases than for highly oriented pyrolytic graphite (HOPG). Although the NFs grow vertically from the substrate with face-on orientation of P3HT chains, we observe edge-on orientation in dried films, presumably due to capillary forces that cause collapse of the NFs onto the substrate during solvent evaporation. Moreover, to control the NF length, long NFs with large length dispersity were sonicated to deliver short NFs to be used in seeded crystallization. Subsequently, these short NFs are extended in a metastable solution of the polymer. However, the resulting extended NFs have a wide distribution of lengths possibly attributed to aggregation of the seeds. Results show that seeds based on poly(3-hexyl thiophene)-b-poly(3-triethyleneglycol thiophene) (P3HT-P3TEGT) may provide more stable seeds to prevent aggregation.

---

\* Adapted with permission from Acevedo-Cartagena, D. E.; Zhu, J.; Trabanino, E.; Pentzer, E.; Emrick, T.; Nonnenmann, S. S.; Briseno, A. L.; Hayward, R. C. *ACS Macro Lett.* **2015**, *4* (5), 483–487. Copyright (2015) American Chemical Society.



## 2.2 Introduction

As polymer-based heterojunction photovoltaic cells often benefit from interpenetrating arrangements of crystalline domains of two semiconducting materials,<sup>13,40</sup> one dimensional (1D) crystalline nanostructures are excellent building blocks for the device active layer. Approaches using top down techniques such as nanoimprinting and lithography have successfully produced active layers with vertically aligned structures from the micron to the nanoscale over wide areas. However, it is difficult to tailor the features near the dimensions of the exciton diffusion length (~10 nm).<sup>13</sup> Solution-based assembly of conjugated organic materials represents a simple and scalable route to tailored crystalline nanostructures from the bottom-up.<sup>10</sup> Ongoing efforts using solution-state processes to assemble nanostructures possessing the desired molecular ordering and orientation include the use of techniques such as dip coating,<sup>41</sup> substrate rubbing,<sup>42</sup> zone casting,<sup>43</sup> and substrate-directed epitaxial growth.<sup>44</sup>

An elegant approach to provide consistent control over the morphology is the employment of pre-formed crystalline nanofibers (NFs) prior to film formation. Previous studies have demonstrated the structural benefit of NFs in the performance of solar cells.<sup>18,45</sup> The NFs dimensions are highly sensitive to the polymer regioregularity, molecular weight, polydispersity, solvent and even processing conditions.<sup>30</sup> The width dependence of P3HT structures obtained through solution crystallization was demonstrated by Liu and coworkers.<sup>46</sup> Nanowhiskers (with widths of 7-13 nm) evolve into nanoribbons (with widths of 50-250 nm) by increasing the supersaturation of P3HT in anisole, only if the chains are shorter than the chain-folding threshold of 10 kg/mol (PS equivalents by GPC). Moreover, the NFs crystallized in solution possess different lengths due to comparable rates of nucleation and growth.<sup>47</sup> If the nucleation rate is regulated, precise control of the lengths of P3HT crystals is obtained, as shown by Rahimi et al<sup>48</sup>. Aggregates are homogeneously melted by heating the solutions close to the dissolution temperature. Consequently, in a self-seeding approach, the least defective crystals are preserved

and subsequently employed to seed dissolved material at a lower crystallization temperature, yielding large single crystals that are homogenous in length. Winnik and Manners<sup>49–52</sup> have shown exquisite control over the nanostructure of a gamma of crystalline block copolymer. These copolymers, including polyferrocenylsilane and P3HT based polymers, form one-dimensional structures termed “cylindrical micelles” through crystallization in solution. In their seeded crystallization method, short cylindrical micelles called “seeds” are first generated from longer ones using ultrasound or by the addition of a good solvent, which upon addition of dissolve polymer termed “unimers” are homogenously extended. However, these block copolymers incorporate groups that are insulators, which are not ideal for organic electronics. We use NFs from pristine P3HT and fully conjugated polymers to overcome this disadvantage and potentially employ these structures into organic electronic devices.

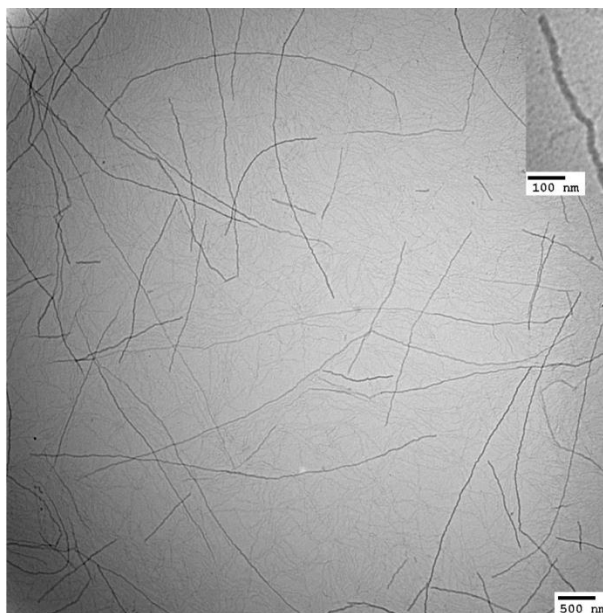
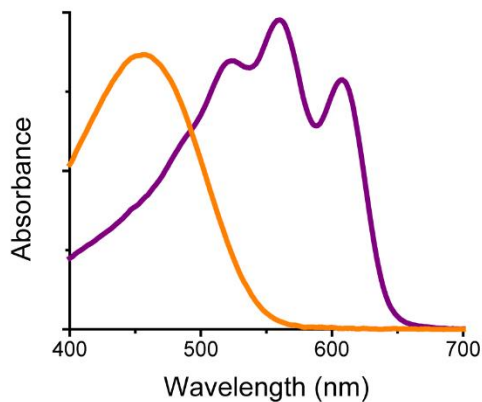
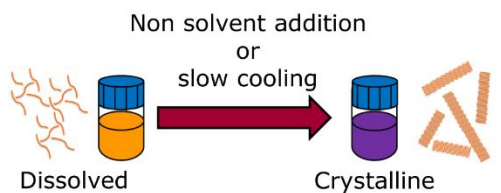


Figure 3: Typical methods for crystallizing P3HT in solution. UV-vis spectra of dissolved P3HT (orange) and crystalline P3HT in solution (purple) (left). Transmission electron microscopy image of P3HT nanofibers (right). As depicted on Figure 3, NF formation is induced when

dissolved P3HT is cooled in a marginal solvent, or a non-solvent is added. The P3HT crystallization is characterized by UV-vis spectroscopy (see Figure 3), where the evolution of a single peak from the dissolved material, with a maximum absorbance at  $\sim 454$  nm, evolves into a series of vibronic peaks at  $\sim 600$  nm,  $\sim 550$  nm,  $\sim 520$  nm due to the increasing  $\pi$ - $\pi$  interactions between chains, signature of solid-state P3HT.<sup>53</sup> As shown in Figure 3 the NFs possess high aspect ratios with widths in the order of  $\sim 20$  nm, which is roughly the exciton diffusion length. However, as seen in Figure 3, after being deposited the NFs crystallized in this matter have an edge-on orientation as they lay horizontally on the surface of the carbon film. Graphene<sup>54,55</sup> represent attractive platform to overcome this situation and direct organization of P3HT into 1D nanostructures, where  $\pi$ - $\pi$  and van der Waals interactions between molecules are known to drive face-on adsorption of crystallized chains.<sup>25,56</sup> Moreover, graphene offers a potential alternative to ITO (indium tin oxide) as a transparent conductive electrode for photovoltaic devices,<sup>57</sup> which can enable graphene surfaces to directly nucleate and orient structures within the active layer of the device. However, while graphene has been shown to nucleate P3HT NFs in suspension<sup>54</sup> and modify crystal orientation in thin films,<sup>25,56</sup> the use of graphene electrode surfaces to direct solution growth of conjugated polymer nanostructures has not been reported.

Here, we present a simple method for selective growth of P3HT NFs directly onto multilayer graphene (MLG) coated Si and ITO substrates, as well as on highly oriented pyrolytic graphite (HOPG). Similarly, this method was used to extend short NFs. To achieve selective crystallization on these nucleating surfaces, a metastable P3HT solution was prepared for which the level of supersaturation is sufficient to allow heterogeneous nucleation but insufficient to induce homogeneous nucleation.

## 2.3 Material fabrication

### 2.3.1 Poly(3-hexyl thiophene) (P3HT) synthesis

Poly(3-hexyl thiophene) (P3HT) was prepared by Grignard metathesis polymerization (GRIM). The monomer, 2,5-dibromo-3-hexyl thiophene was prepared as previously reported,<sup>58</sup> and polymerized following standard protocol.<sup>59</sup> Briefly, 2,5-dibromo-3-hexyl thiophene (1 g) was dissolved in anhydrous THF (24 mL) in a 2-neck round-bottom flask containing a magnetic stir bar and equipped with a reflux condenser. After addition of *tert*-butyl magnesium chloride (2.15 mL of a 1.95 M solution in diethyl ether) the solution was heated to reflux for 2 h, then cooled to room temperature followed by addition of 1,3-bis(diphenylphosphino)propane dichloronickel (II) (Ni(dppp)Cl<sub>2</sub>, 19.5 mg). The mixture became dark red, and was stirred for 20 min. Then, the septum was removed and the mixture was poured into methanol (200 mL). The precipitated polymer was isolated by centrifugation, filtered into a cellulose extraction thimble, and purified by Soxhlet extraction (sequentially in methanol, hexanes, and chloroform). The chloroform fraction was collected and the solvent removed under reduced pressure to yield the desired product. <sup>1</sup>H NMR (300 MHz, CHCl<sub>3</sub>-d<sub>3</sub>, δ): 0.9 (t, 3H), 1.41-1.45 (m, 6H), 1.67-1.72 (m, 2H), 2.55-2.82 (t, 2H), 7.0 (s, 1H). Regioregularity = 93% (NMR), M<sub>n</sub>=11.9k and Đ = 1.28 (polystyrene equivalent by GPC.).

### 2.3.2 Graphene fabrication

The graphene film was grown on both sides of copper foil by chemical vapor deposition at 1000 °C with methane as the carbon source following standard protocol.<sup>60</sup> The reaction system was evacuated with a mechanical pump to 10<sup>-3</sup> mbar. Then, the graphene film on copper foil was transferred onto a cleaned substrate for crystallization using a common wet-chemistry transfer method: spin coating of poly (methyl methacrylate) (PMMA) sacrificial layer, oxygen plasma treatment to etch one side of graphene, and treatment with a copper etchant to remove the copper

foil. The PMMA sacrificial layer was then removed using acetone. Thermal treatment at 300 °C under N<sub>2</sub> flow was performed to remove PMMA residue left during the transfer procedure. For the indium tin oxide layer (ITO), annealing was performed at 250 °C to avoid damaging ITO. Finally, the substrate was washed with acetone and dried with flowing N<sub>2</sub>(g). Prior to transferring graphene, the substrates were cleaned in an ultrasound bath in three steps, using: 1:1 v/v of purified water and Versa Cleaner (Fisherbrand), acetone, and isopropanol. Subsequently, the substrates were dried with flowing N<sub>2</sub>(g) and subjected to UV-ozone cleaning for 10 min. The graphene deposited on Si was characterized by Raman spectroscopy as depicted in Figure 4c. The ratio between intensity of the G peak (1580 cm<sup>-1</sup>) to the 2D (G') peak (2700 cm<sup>-1</sup>) indicates that multilayer graphene (MLG) composed of 2 layers is obtained. Optical profilometry (Figure 4a, b) indicated that the MLG deposited on ITO was 1 ± 0.3 nm thick, corresponding to 2-4 graphene layers.

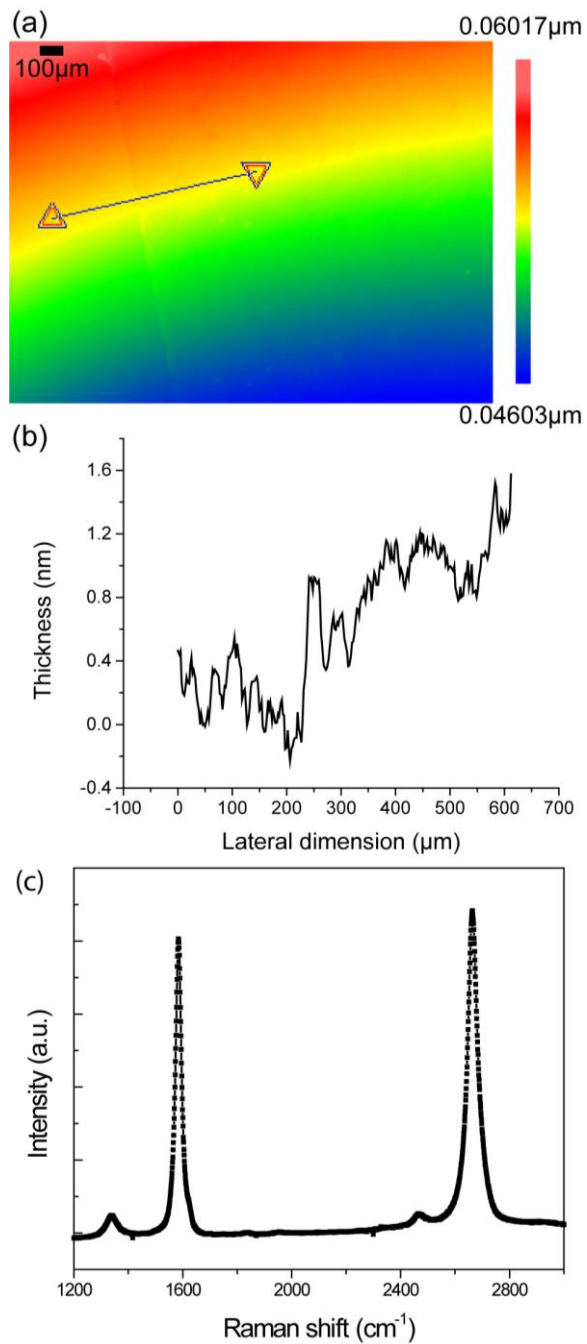


Figure 4: Graphene thickness. Typical optical profilometry measurement of graphene on ITO (a) and the thickness profile along indicated above (b). Raman spectrum of graphene transferred onto Si (c).

## 2.4 Results and discussion

### 2.4.1 Stability of supersaturated solutions of P3HT

As a solvent, we choose *m*-xylene, which was found by Oh et al<sup>47</sup> to provide a high degree of crystallinity and a wide hysteresis window between crystallization and melting temperatures for P3HT NFs. With a relatively low molecular weight P3HT ( $M_n = 12$  kg/mol), as shown below, a hysteresis window centered around room temperature is observed, thereby facilitating NF growth experiments.

The degree of P3HT aggregation is assessed using a Hitachi U-3010 UV-vis spectrometer. Note that reported absorbance values reflect a base-10 logarithm. Firstly, to calculate the concentration of dissolved P3HT  $c_a$  the absorption coefficient at 454 nm  $\epsilon_a$  was determined, using solutions of known concentration prepared by serial dilution (Figure 4a), while fixing the absorbance of pure solvent at zero. To determine the absorption coefficient at 602 nm for the NFs  $\epsilon_f$ , four solutions each with a concentration of dissolved P3HT of  $c = 0.50$  mg/mL were first held for 10 min at  $-5$  °C to initiate crystallization, followed by aging for 10 min at either  $-5$  °C,  $0$  °C,  $10$  °C, or  $20$  °C, then finally allowed to rest at room temperature for 1 d. The amount of crystalline material was found to depend on the aging temperature used, as seen in Figure 5b. These solutions were then filtered using a PTFE membrane ( $0.2$   $\mu$ m pore size), which removed the aggregated portion (Figure 5c), allowing the concentration of dissolved polymer remaining in these solutions  $c_a$  to be quantitatively determined using the previously-measured value of  $\epsilon_a$ . Plotting the absorbance from the 0-0 transition in the unfiltered suspension  $A_{602}$  against the dissolved concentration  $c_a$  (Figure 5Figure 4d) finally allowed for a determination of  $\epsilon_f$  using the Beer-Lambert Law, as follows:

$$A_{602} = \epsilon_f l (c - c_a) \quad [1]$$

where  $l$  is the path length for the UV-vis measurement. The best-fit value of  $c = 0.51 \pm 0.06$  mg/mL agrees with the initial concentration of the prepared solution (0.50 mg/mL), providing further confidence in the method.

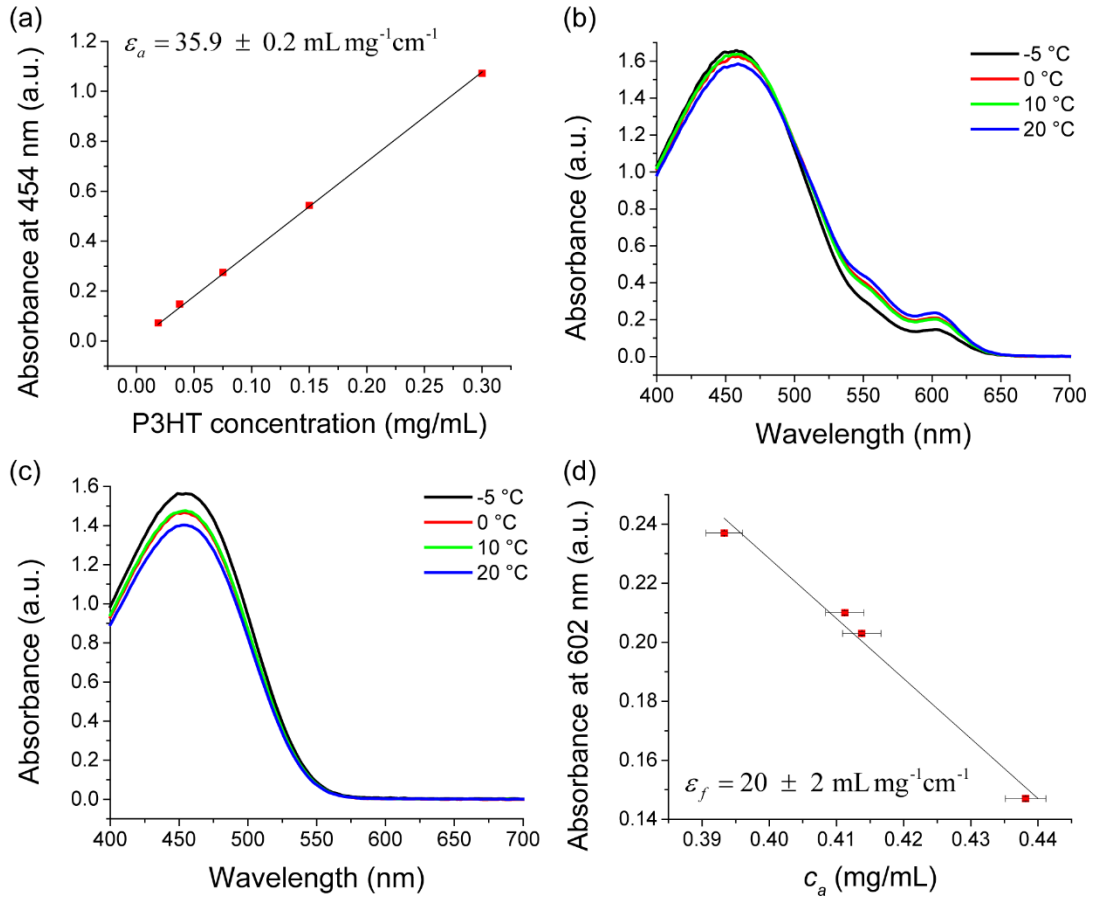




Figure 5: Determination of the mass absorption coefficients of the dissolved ( $\epsilon_a$ ) and crystalline ( $\epsilon_f$ ). Determination of  $\epsilon_a$  using the absorbance at 454 nm for solutions of dissolved P3HT (a). UV-vis absorbance spectra of P3HT crystallized first at  $-5^\circ\text{C}$  and subsequently incubated at the indicated temperatures (b), along with UV-vis spectra following filtration to determine the remaining concentration of dissolved polymer  $c_a$  after crystallization (c). Determination of  $\epsilon_f$  from a plot of the absorbance at 602 nm of the crystallized solutions against  $c_a$  (d). To study the stability of the supersaturated solutions of P3HT, a vial containing P3HT dissolved in *m*-xylene with a concentration of 0.5 mg/mL was kept inside a recirculating water bath to control the temperature and aliquots of the solution were taken to measure the absorbance in the spectrometer, which were immediately returned to the vial. From the UV-vis spectrum of a given sample with known total P3HT concentration,  $c$ , a direct measurement of the aggregated fraction,  $x_f$ , can be calculated from the Beer-Lambert law, i.e.,  $x_f = A_{602}/(\epsilon_f c l)$ . We note that the value of  $x_f$  is likely larger than the crystalline fraction  $x_c$ , since the NFs are not single crystals and likely possess amorphous regions,<sup>61</sup> but nonetheless provides an excellent proxy for the degree of crystallization.

The hysteresis between crystallization and melting of P3HT NFs with changes in temperature can be clearly seen in Figure 6d. No aggregation is observed at room temperature on a time scale of  $\sim 10$  min, but upon cooling below  $0^\circ\text{C}$ , P3HT rapidly crystallizes into NFs that remain stable until they are heated to  $40^\circ\text{C}$ . Curiously,  $x_f$  increases while heating from  $-5^\circ\text{C}$  to  $20^\circ\text{C}$ , which may reflect slow crystallization kinetics at lower temperatures, or perhaps melting of some fraction of the crystals formed at low temperature as they warm to room temperature during UV-vis measurements. Regardless, the data in Figure 6d clearly demonstrate that at room temperature a sizeable thermodynamic driving force for crystallization exists, while the rate of crystal nucleation in solution is negligible. Therefore, these solutions exist in a metastable state at room temperature.

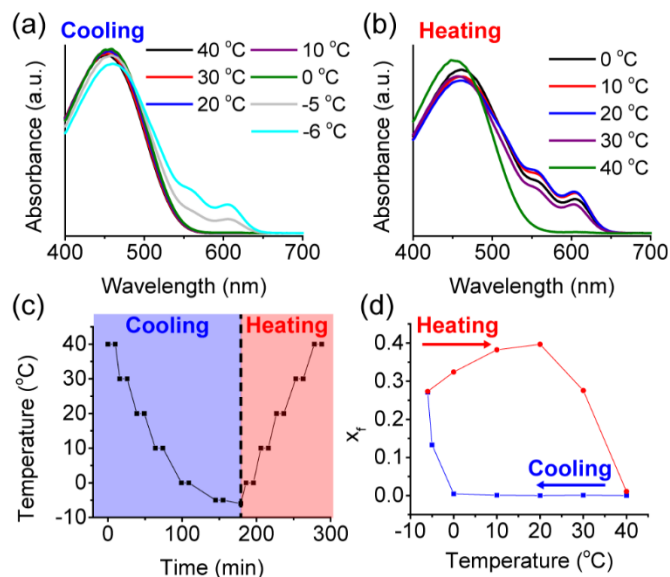


Figure 6: The hysteresis between crystallization and melting of P3HT NFs. UV-vis spectra of 0.50 mg/mL solution of P3HT in *m*-xylene during (a) cooling and (b) heating, along with (c) the temperature profile employed (the sample was held for at least 10 min at each temperature), and (d) the degree of aggregation  $x_f$  measured during the temperature cycle. **2.4.2 Nanofiber formation on multilayer graphene**

Remarkably, incubation of ITO substrates partially coated with MLG in the metastable solution at room temperature leads to highly selective crystallization of P3HT, as clearly seen by the purple color in the MLG-coated area, while the uncoated portion remains colorless (Figure 7a). The absorbance spectra of these deposited films show vibronic peaks characteristic of crystalline P3HT, monotonically increases with time due to the increased growth of NFs. Similarly, atomic force microscopy (AFM)/optical profilometry measurements reveal a slow increase in the average film thickness with time, up to  $5.4 \pm 0.8$  nm after 120 h of incubation (Figure 7b).

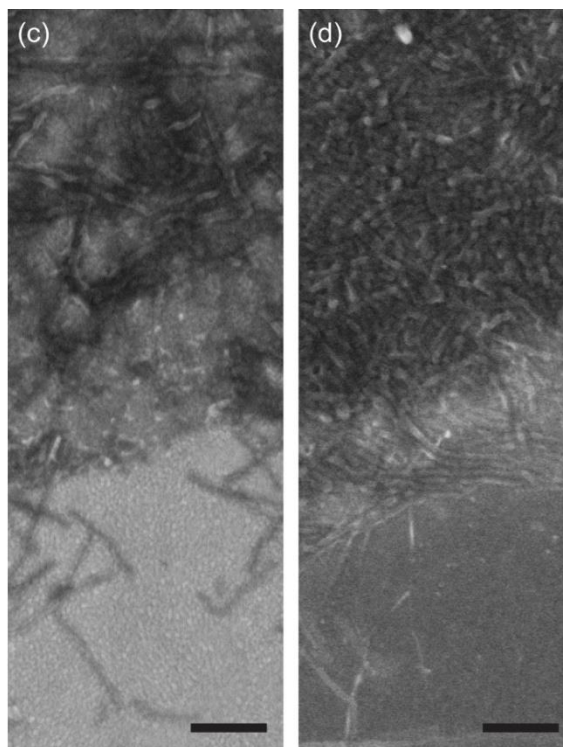
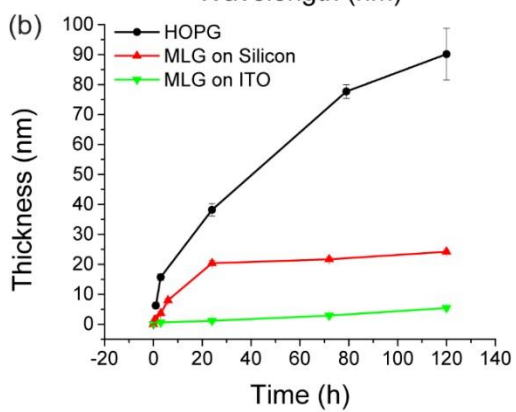
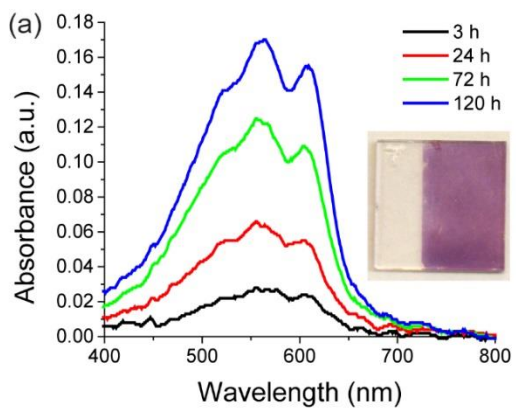


Figure 7: Selective crystallization of NFs from different MLG coated substrates. UV-vis absorbance spectra of P3HT films grown on MLG on ITO at different times of incubation in a metastable solution of P3HT (a). The inset shows a photograph of a film of P3HT NFs grown for 120 h on ITO coated with MLG only on the right side. Thicknesses of P3HT films as function of incubation time determined by AFM for MLG on Si (red) and HOPG (black), and by optical profilometry for MLG on ITO (green) (b). Error bars represent one standard deviation based on 10 measurements. SEM images of the interface between MLG-coated regions (top) and the bare substrate (bottom) after 24 h of growth using ITO (c) and Si (d) substrates. Scale bars: 200 nm. Surprisingly, as seen in Figure 7b, the rate of crystallization is substantially faster when a

silicon wafer is used as the underlying substrate instead of ITO, leading to an average film thickness of 20 nm within 24 h, followed by much slower growth. Examination of the interface between the graphene-coated regions and the bare substrates with scanning electron microscopy (SEM) (Figure 7c, d) reveals that the P3HT films are composed of NFs with lengths over 100 nm.

For MLG on Si, the surface is completely covered by NFs, while for ITO as an underlying substrate, the density of NFs is lower and some portions of the MLG surface remain exposed. These observations are consistent with the measured average film thicknesses of  $1.2 \pm 0.6$  nm for MLG on ITO and  $20 \pm 0.9$  nm for MLG on Si following 24 h of growth, since the individual NFs are  $3 \pm 0.9$  nm thick (Figure 8). P3HT crystallization remains highly selective to MLG on both substrates; while NFs that presumably nucleated on the graphene surface stretch several hundred nanometers away from the interface onto the bare substrate surface (Figure 7 and Figure 8), no sign of NFs is observed further from the interface.

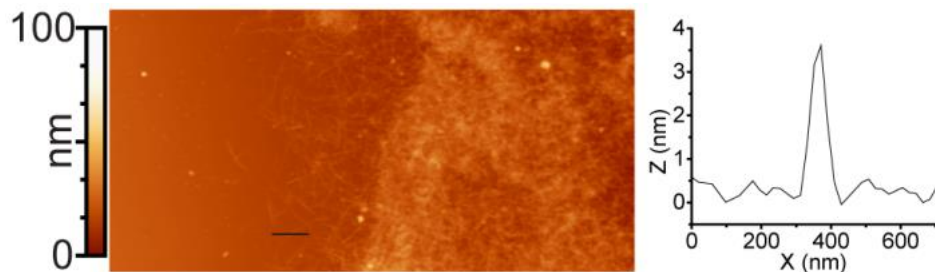


Figure 8: AFM images of the Si/graphene interface with P3HT grown for 24h along with the thickness profile along the indicated black line, across a single NF.

Amazingly, freshly cleaved HOPG allows P3HT to crystallize into a  $90 \pm 8.6$  nm thick film.

Assuming a density of 1.1 g/mL for P3HT,<sup>62</sup> the film thicknesses from graphene on ITO can

be compared to the UV-Vis spectra (Figure 7a) to determine an absorption coefficient at 602 nm for the solid films ( $\epsilon_s$ ). Interestingly, the value of  $\epsilon_s = 270 \pm 30 \text{ mL cm}^{-1} \text{ mg}^{-1}$  is more than an order of magnitude larger than the value of  $\epsilon_f$  for the suspended NFs. Since the electric transition dipole of P3HT is oriented along the chain axis,<sup>63</sup> orientation of NFs within the solid film should lead to a 3-fold increase in absorption of light with normal incidence, compared to a randomly oriented suspension.<sup>64</sup> Additionally, the dried film shows a more intense absorption for the 0-0 transition relative to the 0-1 and 0-2 peaks (Figure 9b), corresponding to increased intrachain planarity (J-aggregate character) in the dried NFs compared to those in suspension.<sup>53</sup>

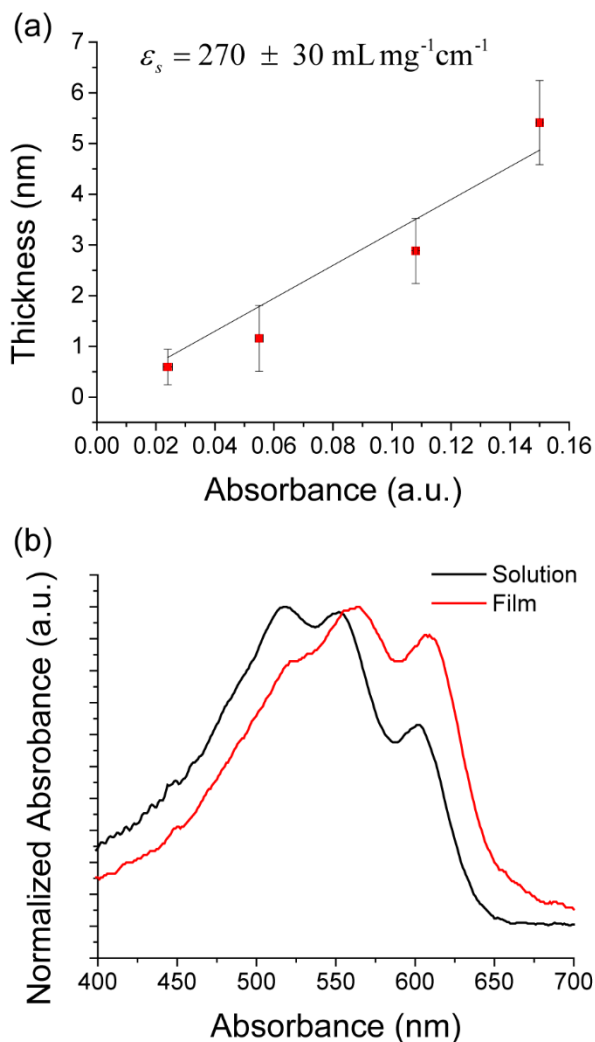


Figure 9: Determination of  $\epsilon_s$  from a plot of absorbance at 602 nm of solid films against measured thickness (a). Normalized absorbance spectra of P3HT NFs in solution (black) and in a film (red) (b). The experimental conditions were carefully chosen to prevent adsorption of crystals on the substrate surface. The metastable solution was prepared by heating 0.5 mg of P3HT in 1 mL of *m*-xylene to 80 °C, beyond its melting point, using a water bath. After the polymer was dissolved, the solution was left to cool inside a water bath reaching room temperature in approximately 2 h. The substrate (e.g., graphene coated Si) was incubated in solution at room temperature (22 °C) with mild agitation on an orbital shake plate for the desired time for P3HT crystallization. The metastable solutions showed no evidence of NF formation by UV-vis (Figure 10), even after 120 h of aging at room temperature, thus the occurrence of NFs on MLG clearly results from surface-driven nucleation rather than adsorption of solution-nucleated structures.

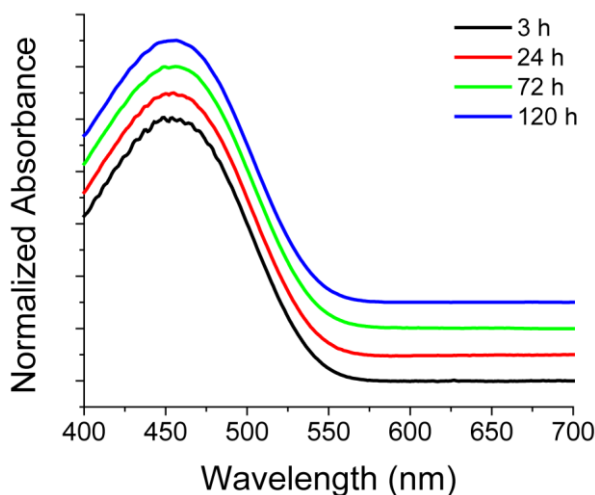


Figure 10: Normalized UV-vis absorbance spectra of metastable solutions of P3HT incubated with graphene coated ITO substrates at room temperature for the lengths of time indicated in the legend. The curves are offset vertically for clarity.

To discard the possibility that dissolved P3HT may crystallize during solvent drying, the samples were gently rinsed with fresh *m*-xylene. Furthermore, two control experiments were performed to verify that the observed NFs were not formed during solvent evaporation: a solution of P3HT at 0.5 mg/mL in *m*-xylene was (Figure 11a) drop casted on a HOPG flake, and (Figure 11b) spin casted on a MLG coated Si. As seen in Figure 11, no evidence of NFs was found in either case, as the features and contrast observed are inherent to the bare substrates.

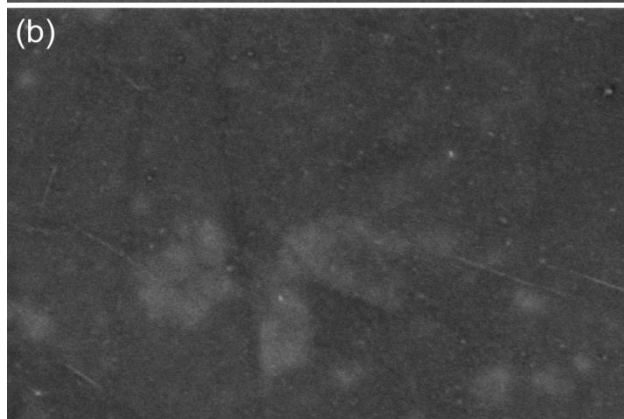
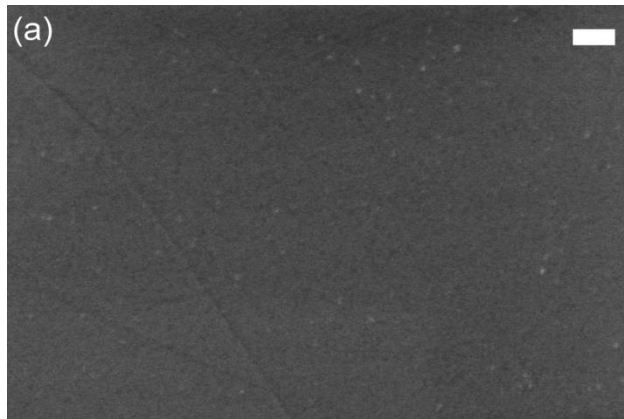


Figure 11: SEM images of P3HT films formed from a 0.5mg/mL solution by drop casting (a) on HOPG and spin casting on graphene coated Si (b). The images observed are like those for the respective bare substrates. Scale bar: 100 nm. The film thicknesses were measured using a

NewView 7300 white light interferometer (optical profilometer) and a Veeco Dimension 3100

AFM operated in tapping mode. At least 10 measurements were collected at the interface between

P3HT and ITO using optical profilometry to determine the thickness of the P3HT films grown

from MLG on ITO. A representative measurement of the thickness of graphene on ITO is

illustrated in Figure 4. AFM images of P3HT crystallized from MLG on Si and HOPG were

collected (Figure 12 and Figure 13, respectively), and from each one at least 10 thickness profiles

were measured to determine the film thickness of the respective sample. In the case of HOPG, the

surface was partially covered with polyacrylic acid (PAA) sacrificial layer by drop casting from

methanol. After growing P3HT NFs, the PAA sacrificial layer was removed by soaking the

substrate in methanol overnight to allow the P3HT film thickness to be measured.

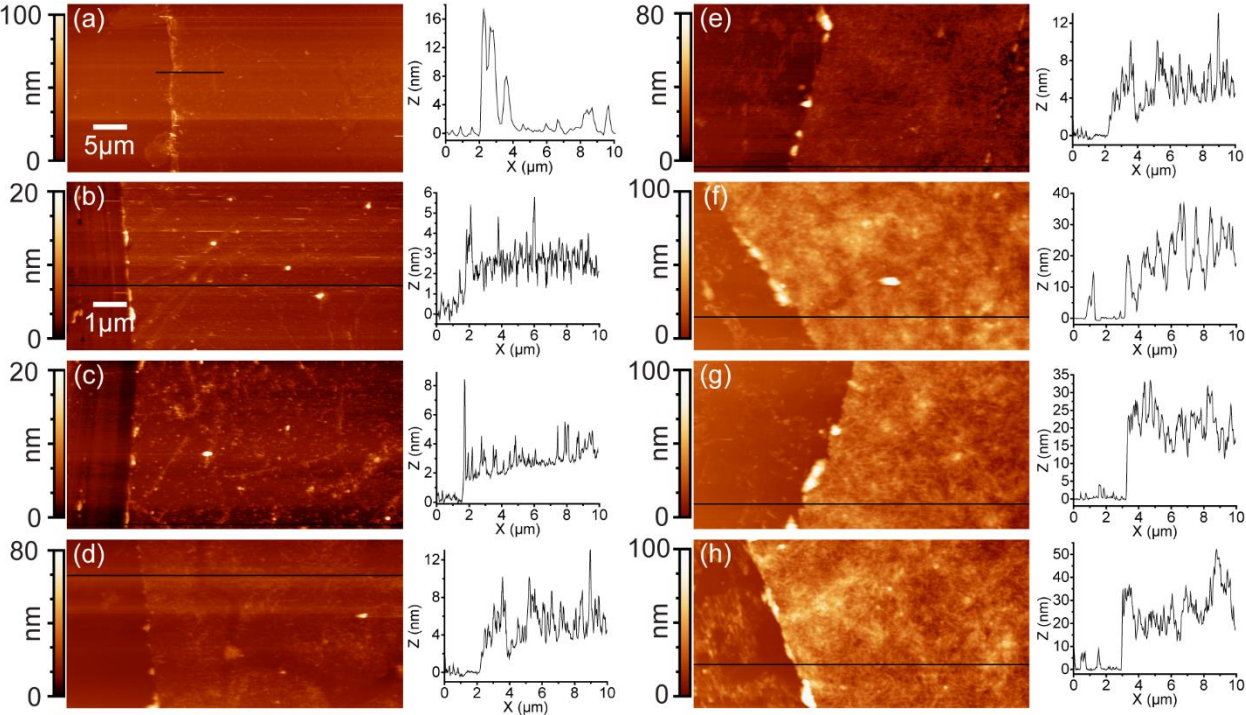




Figure 12: AFM images of MLG deposited on Si (a), and following crystallization of P3HT for 30 min (b), 1 h (c), 3 h (d), 6 h (e), 24 h (f), 72 h (g), and 120 h (h), along with the respective thickness profiles along the indicated black lines.

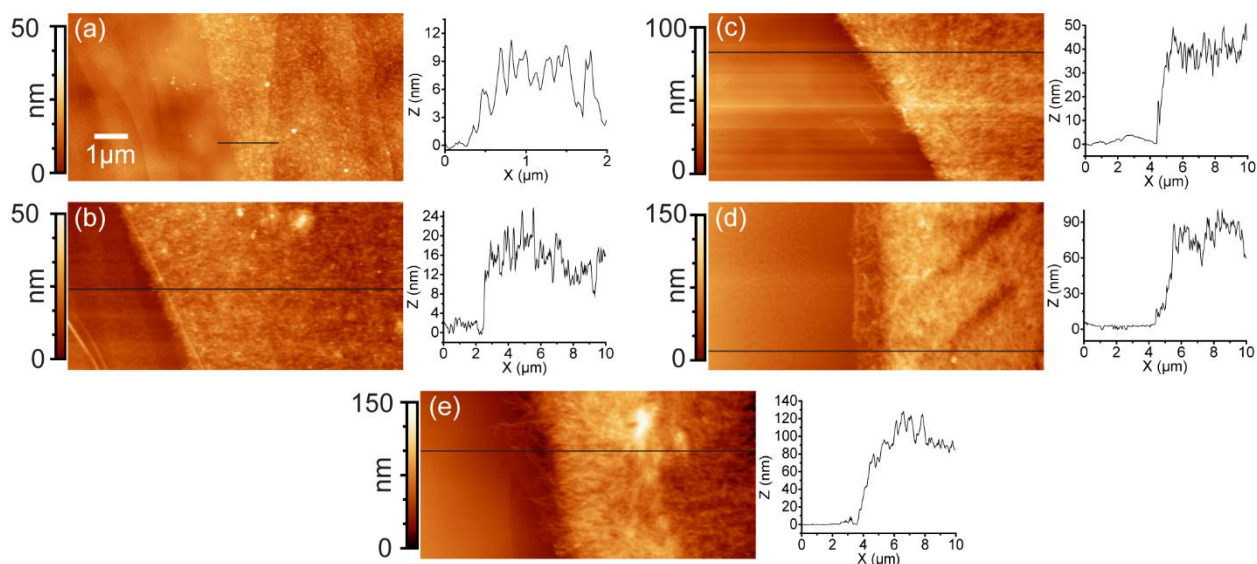


Figure 13: AFM images of P3HT crystallization on HOPG for 1 h (a), 3 h (b), 24 h (c), 79 h (d), and 120 h (e), along with the respective thickness profiles along the indicated black lines.

### 2.4.3 Effects of the underlying substrate on the formation of P3HT nanofibers

The film thickness of P3HT NFs grown on MLG on Si and on HOPG seems to saturate, or at least slow down considerably in the later stages of growth, as seen in Figure 7. Since the solutions are agitated throughout growth, this is apparently not due to a diffusion-limited process. Instead, we suspect that this behavior reflects self-poisoning of the NFs growth caused by the accumulation of defects, or by the competing crystallization between folded and extended chains,<sup>65</sup> since the molecular weight of P3HT used ( $M_n = 12$  kg/mol) is close to the threshold for chain folding (10 kg/mol).<sup>46</sup> Moreover, the observed sensitivity of crystallization kinetics to the underlying substrate may arise from several factors. Van der Waals interactions with the substrate likely represent an important contribution, and should be stronger for Si than for ITO (respective estimated polarizability values of  $3.76 \text{ \AA}^3$  and  $0.58 \text{ \AA}^3$  based on the Clausius-Mossotti relation and dielectric constants of 12.1 for Si<sup>66</sup> and 3.68 for ITO,<sup>67</sup> ignoring the influence of the native oxide layer on Si). The higher polarizability of HOPG compared to MLG (also invoked by

Shokri, et al<sup>68</sup> to explain stronger adsorption of substituted aromatic molecules on HOPG) may be responsible for the high rates of growth on HOPG, although making a direct comparison is complicated by the relatively high defect density of MLG grown by chemical vapor deposition, as employed here. Substrate roughness may also play a role: as seen in Figure 7c, ITO is composed of grains with average sizes of 15 nm, which is comparable to the contour length of P3HT chains,<sup>69</sup> possibly impeding crystal nucleation compared to the smoother Si surface (Figure 7d). Additionally, since the interaction between P3HT and graphene involves a degree of charge transfer,<sup>70</sup> the impact of the underlying substrate on the electronics of graphene could further influence the nucleation rates.

Additional insight into how graphene and HOPG substrates influence P3HT NF growth is provided by SEM images showing the evolution of film morphology with time. During the initial stages of growth on HOPG and MLG on Si (Figure 14a, c), individual P3HT NFs with lengths below 50 nm and widths of  $16 \pm 2$  nm are observed. For MLG on Si, the short NFs in Figure 14c are observed after approximately 0.5 h, while for HOPG a high density of short NFs can already be seen after only 5 min (Figure 14a). At 3 h (Figure 14b, d) HOPG is completely covered with NFs, and MLG on Si shows long NFs. However, for MLG on ITO (Figure 14e, f), no evidence of NFs is seen at 3 h, while after 24 h, long NFs are observed. These results are consistent with a similar rate of growth of NFs on each substrate, but a nucleation rate that increases from MLG on ITO, to MLG on Si, to HOPG. Based on *in situ* measurements showing that P3HT possibly adsorbs with epitaxial registry on HOPG,<sup>71</sup> the nucleation observed here is likely epitaxial.

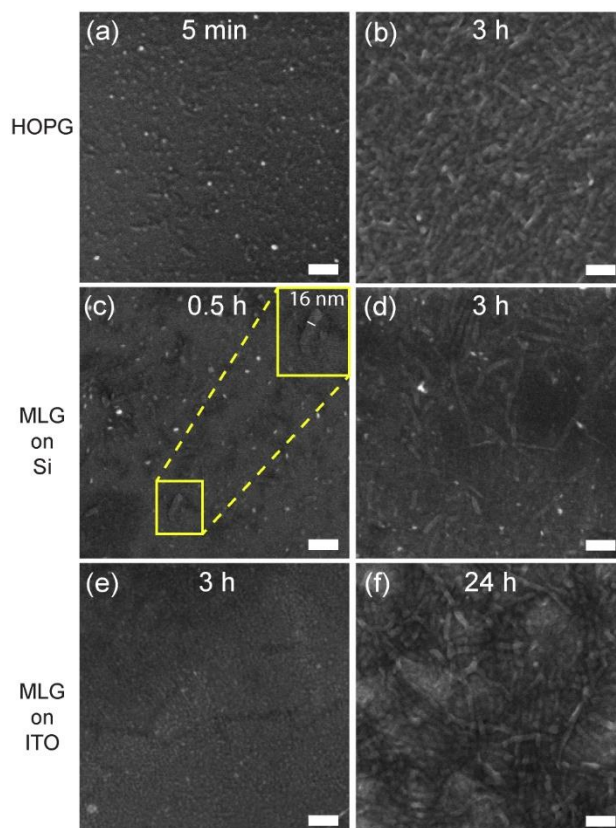


Figure 14: SEM images of P3HT crystallized from a metastable solution on different substrates HOPG for 5 min (a) and 3 h (b); MLG on Si for 0.5 h (c) and 3 h (d); MLG on ITO for 3 h and (e) 24 h. (g) Scale bar = 100 nm. The inset in (c) shows an individual short NF.

Since P3HT chains have been reported to adsorb with face-on orientation on MLG<sup>56</sup> and HOPG,<sup>71</sup> and the direction of  $\pi$ -stacking is along the long axis of the fibers, we expect that the NFs would grow perpendicular to the substrate. However, the NFs observed by SEM in the dried films orient parallel to the substrate, even at the longest time studied (120 h), as seen in Figure 15. Moreover, grazing incidence wide angle X-Ray scattering (GIWAXS) measurements reveal strong ( $h00$ ) reflections and no clear (010) reflection along the out-of-plane direction  $q_z$ , with much weaker ( $h00$ ) reflections and a clear (010) peak along the in-plane direction  $q_{xy}$ , further confirming the edge-on orientation of crystalline NFs in the dried films (Figure 15d).

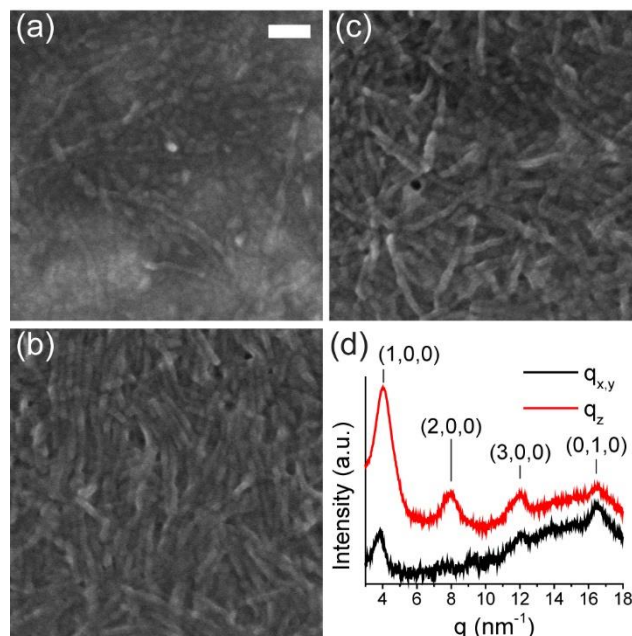


Figure 15: SEM images of P3HT NFs grown from a metastable solution from 120 h on MLG on ITO (a), MLG on Si (b) and HOPG (c). Scale bar = 100 nm. (d) Grazing incidence wide angle X-ray scattering from P3HT films grown for 120 h on MLG on Si.

However, if NFs crystallize along the substrate in an edge-on orientation, we would expect the film thickness to plateau around the thickness of an individual NF ( $\sim 3$  nm), rather than growing to 25 nm in the case of MLG on Si, or to 90 nm in the case of HOPG. Instead, we suspect that the observed edge-on orientation is the result of capillary collapse during solvent removal as illustrated in Figure 16.

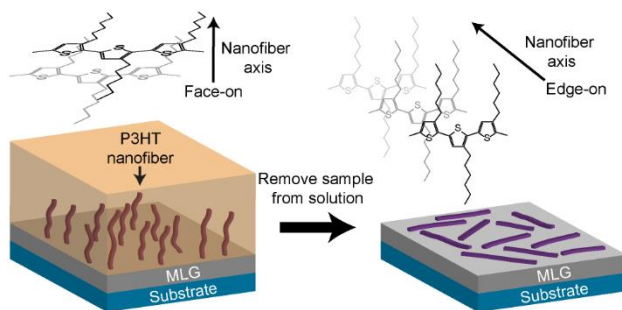


Figure 16: Schematic illustration of nanofibers grown in solution before (left) and after (right) removing the substrate from the fluid, with their respective chain orientations.

Note that for a ribbon with thickness  $t$ , width  $w$ , and bending stiffness,  $B = Et^3w/12$ , surface tension  $\gamma$  will cause buckling beyond a critical length<sup>72</sup>:

$$l_c = \sqrt{\frac{B\pi^2}{8\gamma(t+w)}} \quad [2]$$

using measured values of  $t = 3$  nm and  $w = 16$  nm, along with the surface tension  $\gamma = 0.029$  N/m for *m*-xylene, and an plain-strain modulus for P3HT of  $E = 1.2$  GPa<sup>73</sup>, we estimate a value of  $l_c = 10$  nm. Thus, the flexibility of the thin NFs means that surface tension is sufficient to cause collapse of NFs oriented vertically in solution into a consolidated film with predominantly in-plane orientation.

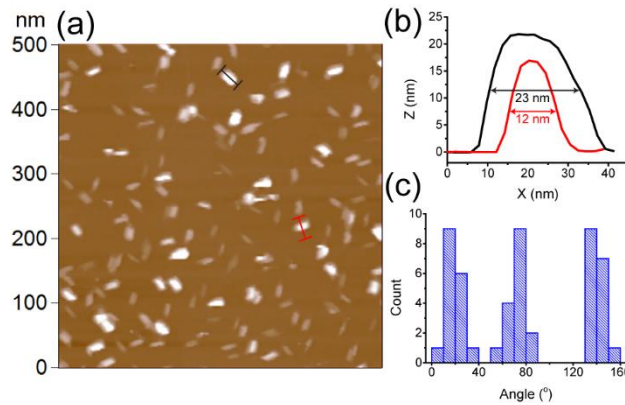


Figure 17: AFM images taken during solution crystallization of a 0.5 mg/mL solution of P3HT-12k from HOPG (a) and with their respective line profiles (b). In-plane orientation angle of the lateral long axis of the NF with respect of an arbitrary angle of the HOPG surface (c).

The NF growth was examined in-situ using AFM as seen in Figure 17. To visualize the NF growth, HOPG was employed as nucleating substrate because it was found to provide the fastest crystallization kinetics. A 0.5 mg/mL solution was injected into the substrate located in the isolated sample chamber (perfusion chamber) of a Cypher ES AFM. Using tapping mode, the solid/liquid interface was imaged as seen in Figure 17. Remarkably, the HOPG surface was covered with features 1-14 nm tall  $10 \pm 3$  nm wide and  $25 \pm 3$  nm in length. Although there is a convolution error on the exact values a tip radius of  $\sim 9$  nm permit visualization of the NF lateral dimensions, demonstrating that the NFs are orientated at  $0^\circ \pm 3^\circ$ ,  $62^\circ \pm 7^\circ$ ,  $120^\circ \pm 6^\circ$  along the three crystallographic axes of HOPG. This suggests that the P3HT epitaxially adsorbs on HOPG. This method provides a route to characterize the crystallization mechanism of P3HT NFs *in situ*.

#### 2.4.4 Seeded Crystallization

The NFs widths of 10 – 20 nm are ideal for the diffusion and dissociation of excitons. However, controlling crystal nucleation vs. growth kinetics remains key, as uncontrolled crystallization can lead to unintentional defects and charge traps.<sup>45</sup> As previously described, conditions have been identified for generating metastable solution of P3HT ( $M_n = 12$  kg/mol) in *m*-xylene, thus opening the door to seeded crystallization using pre-formed P3HT crystals. NFs are formed by crystallizing at low temperature (e.g. 2 °C), where the super-cooling is sufficient to drive nucleation on time-scales of several hours. Once formed the NFs are subjected to centrifugation to remove any free polymer from solution. Two cycles of centrifugation at 10 krpm for 1 h were enough to remove most of the free polymer in the supernatant. The resulting fibers, with average lengths of  $800 \pm 100$  nm are then shortened to  $80 \pm 10$  nm by ultrasonication at 5°C, as shown in Figure 18. Constant low temperatures helped to dissipate the heat generated during sonication, thus preventing melting and recrystallization of NFs.

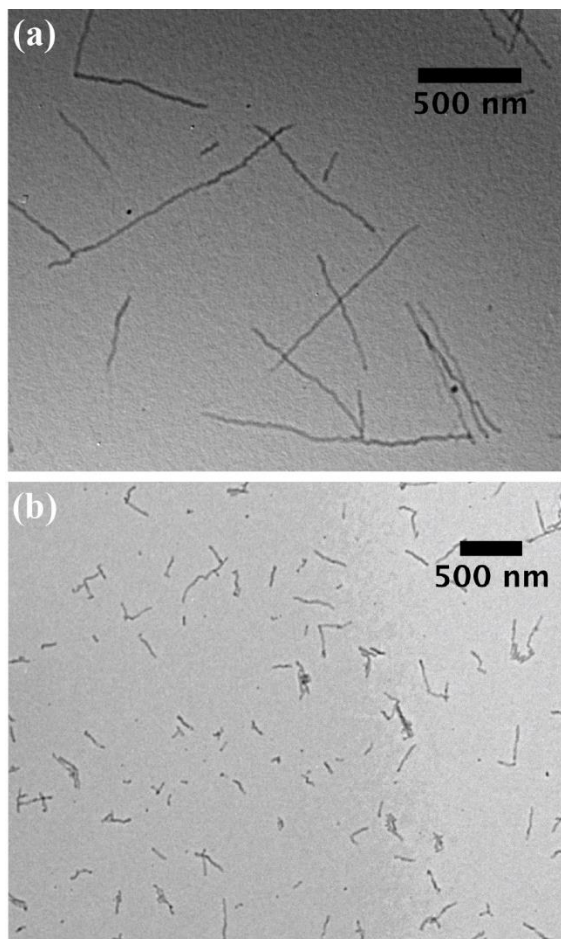


Figure 18: TEM images of P3HT NFs in m-xylene as centrifuged (a) and after 3 h (b) of sonication at 5 °C.

Injecting higher amount of these seeds into solutions with a constant unimer (i.e. dissolved polymer) concentration increased the crystallization kinetics (as judged by UV-vis spectroscopy, Figure 19 and Figure 20). It was noticed that the container walls turned purple, which indicates that P3HT can adsorb or crystallize on the container walls. Given that the total concentration of P3HT  $c$  is decreasing over time the relation  $x_f = c_f / (c_f + c_a)$  was used to calculate the fraction of NFs in solution  $x_f$ . Since the individual absorption coefficients of the pristine fibers and the dissolved polymer are known, the  $c_a$  can be determined subtracting the contribution of  $c_f$  (i.e., calculated from the absorbance at 602 nm) from the total absorbance of the solution. Interestingly, high amounts of seeds led saturation of the growth kinetics and to undesired aggregation, possibly because pre-aggregated seeds promoted more aggregation. As determined by TEM (Figure 21), the seeds do



increase in length, indicating that seeded crystallization is to some degree successful. However, the resulting crystals still exhibit a broad dispersity in length, and in some cases, appear to be aggregated, indicating that further work is needed if seeded growth is to provide length control over P3HT nanostructures.

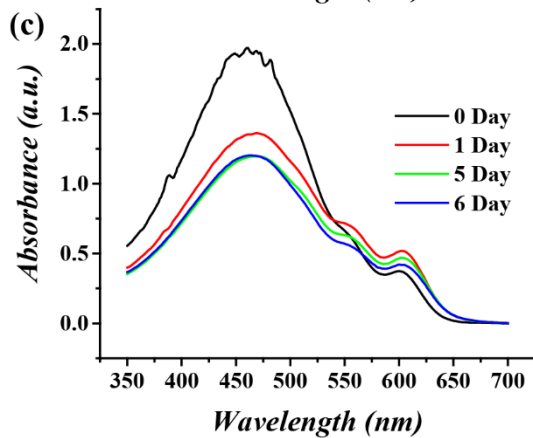
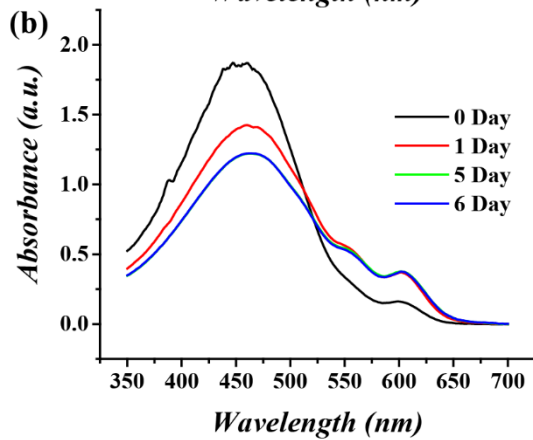
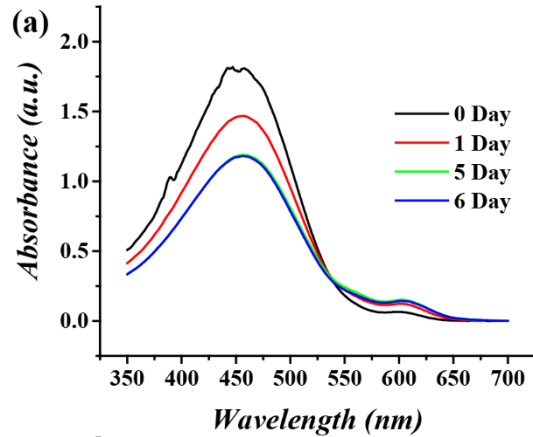




Figure 19: Seeded crystallization kinetics as characterized by UV-vis of unimers. incubated with different amount of seeds in solution for 6days: 8% (a), 14% (b), and 24% (c) out of the total P3HT in solution seeded crystallization

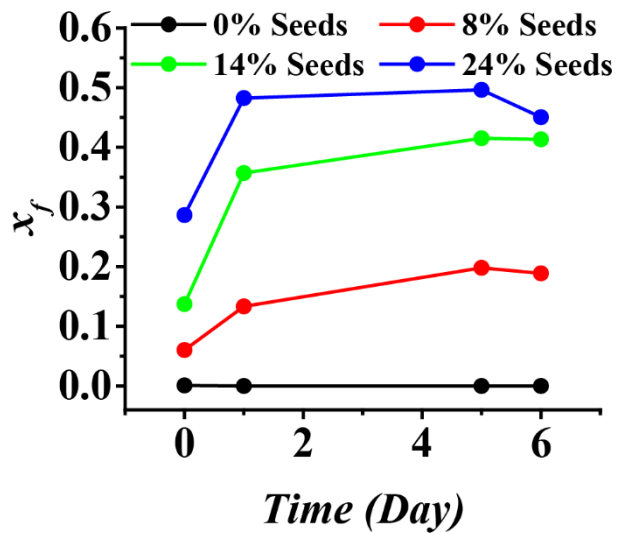


Figure 20: NF fraction as function of time. Unimers (a). incubated with different amount of seeds in solution for 6days: 8%, 14%, and 24% out of the total P3HT in solution

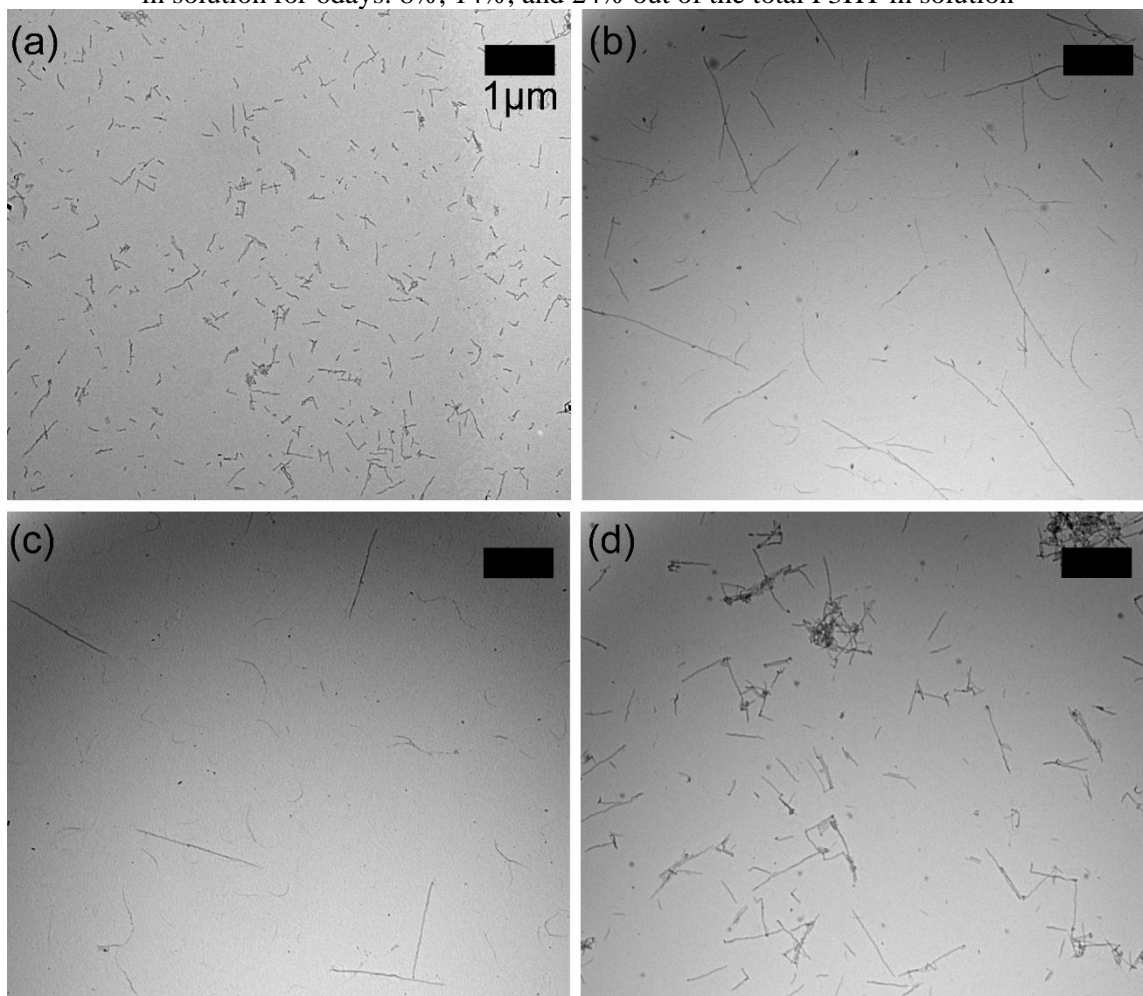


Figure 21: TEM images of P3HT seeds initially (a). Different amount of seeds incubated with the same amount of unimers in solution for 6days: 8% (b), 14% (c), and 24% (d) seeds out of the total P3HT in solution.

To improve seed stability and mitigate NF adsorption of the NFs on the walls of the vial, NFs and seeds were prepared from a block copolymer consisting of poly(3-hexyl thiophene) and poly(3-triethyleneglycol thiophene) (P3HT-P3TEGT, 1.85:1,  $M_n = 18$  kg/mol). Presumably, the P3TEGT block remains at the edge of the NFs in a dissolved state, stabilizing the P3HT core.<sup>74</sup> Using a 4:1 mixture of chlorobenzene and methanol (CB:MeOH) P3HT-P3TEGT was crystallized into NFs by cooling to 2 °C. Sonication at 5 °C for 3 h these NFs were converted into seeds with negligible amount of aggregation (Figure 22).

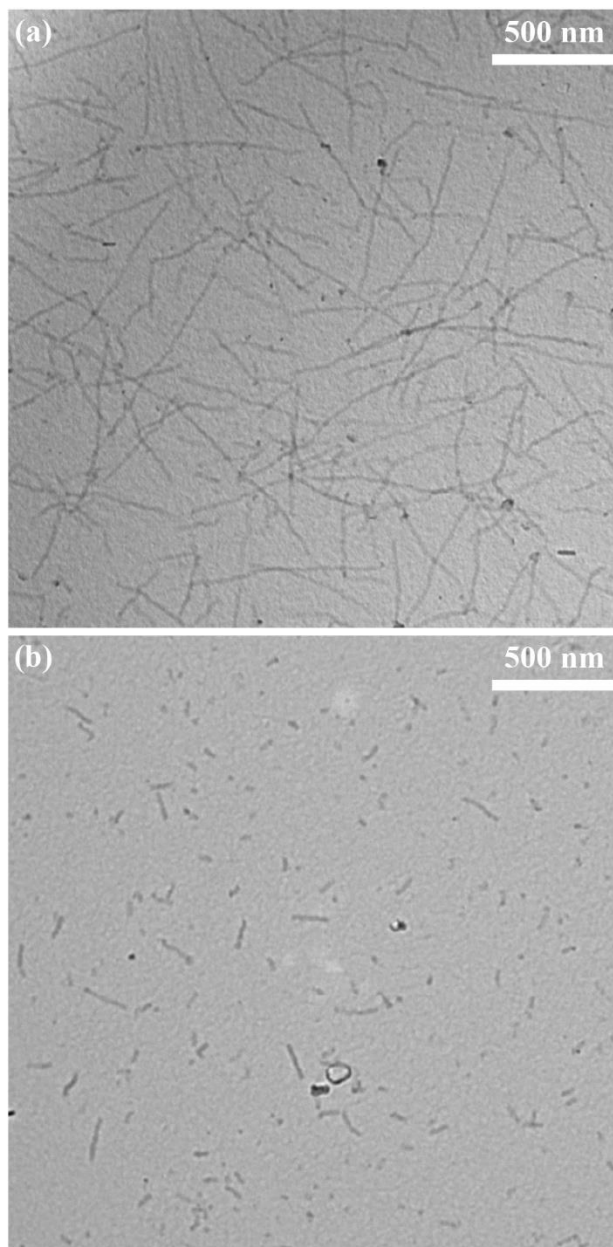


Figure 22: P3HT-b-P3TEGT (1.85:1,  $M_n = 18$  kg/mol) NFs formed in a chlorobenzene:methanol (4:1) solution at 1mg/mL before (a) and after (b) sonication for 3 h at 5 °C.

## 2.5 Conclusions

We have demonstrated a method for selective crystallization of P3HT NFs from graphene surfaces in solution. Surprisingly, the rate of crystal nucleation is found to be highly dependent on the underlying substrate, suggesting a potential route for further tailoring crystallization kinetics. Although we expect that the NFs grow out-of-plane due to face-on adsorption of P3HT chains on

graphene followed by  $\pi$ - $\pi$  stacking, capillary forces are sufficient to cause collapse into a horizontally oriented NF film upon solvent removal. *In situ* measurements with AFM confirmed that the NFs grow out-of-plane in solution growth reaching heights of 20 nm in the time frame of the experiment. These findings should be relevant to other conjugated polymers showing similar interactions as P3HT with graphene, thereby providing a new method for the study of surface-directed crystallization and novel pathways for fabricating organic electronic devices. The seeded crystallization of P3HT showed that seeds can be extended into longer NFs but this process is hindered by aggregation and adsorption onto the container's wall during crystallization. P3HT-P3TEGT was shown to produce more uniform seeds and promises to mitigate the mentioned issues with the homopolymer.

## CHAPTER 3

### FORMATION MECHANISM OF P3HT NANOFIBERS CRYSTALLIZED FROM GRAPHENE

#### 3.1 Abstract

Solution-based crystallization is a powerful route to tailor the hierarchical morphology of conjugated polymers and increase the performance of organic electronic devices. Poly(3-hexyl thiophene) (P3HT), a workhorse in the study of organic electronic devices, assembles into nanofibers (NFs), which are beneficial for the charge mobility of the resulting films. In this study, we investigate the influence of the physical properties of P3HT (*e.g.*, regioregularity, molecular weight and concentration) on the hysteresis observed during the solution-based assembly of NFs. It was found, that this hysteresis (*i.e.*, difference between the crystallization and melting temperatures) increases with molecular weight due to an increment in the lamellar size (*i.e.* NF width) as observed by transmission electron microscopy. From this hysteretic behavior, we demonstrate, with P3HT, a platform to characterize the crystallization on the surface of graphene *in situ* through high resolution atomic force microscopy (AFM). Surprisingly, AFM showed an interchain distance along the *a* crystal axis of  $16.7 \pm 0.7 \text{ \AA}$ , and  $7.7 \pm 0.2 \text{ \AA}$  for the *c* crystal axis, which suggest that the crystals on the surface of graphene are Form I. Although the NFs crystallize out-of-plane from graphene, capillary forces are sufficient to render them into an in-plane orientation. Imbedding the wet NFs in an amorphous matrix of an indene-C<sub>60</sub> bisadduct, an electron acceptor, during solvent evaporation partially preserves the face-on orientation. Similarly, poly[2,5-bis(3-tetradecylthiophen-2-yl)thieno[3,2-*b*]thiophene] (PBTTT) crystallizes into NFs from graphene with similar orientation angles with the HOPG crystallographic axes as for P3HT. For PBTTT, however, the observed interchain distance along the (100) dimension by *in situ* AFM was larger ( $26.4 \pm 0.3 \text{ \AA}$ ) than crystals formed in bulk ( $21.5 \text{ \AA}$ ). This study provides

a better understanding about the crystallization and assembly of conjugated polymers suitable for organic electronics.

### 3.2 Introduction

Conjugated polymers are intriguing materials capable of crystallizing into nanostructures suitable to increase the performance of electronic devices.<sup>10,75</sup> However, control over the hierarchical assembly of conjugated polymers in solution remains a challenge due to the wide variety of parameters that affect polymer assembly during film formation.<sup>76-78</sup> Since nucleation is typically stochastic,<sup>79</sup> it is desired to introduce nucleating agents to better control the crystallization assembly of conjugated polymers.<sup>47</sup> To achieve this objective, there has been a growing interest in the use of pre-existing nucleation sites such as 1,3:2,4-bis(3,4-dimethylbenzylidene)sorbitol,<sup>80</sup> seed crystals,<sup>49</sup> electron acceptors,<sup>81</sup> carbon nanotubes<sup>82</sup> and graphene derivatives<sup>54,83</sup> to drive growth of conjugated polymer crystals, with most work focusing on poly(3-hexyl thiophene) (P3HT).

Amongst these nucleating agents, graphene derivatives are particularly interesting due to their tunable electronic properties and high conductivities, which have been exploited to improve the performance of photovoltaic cells, both in the form of additives and electrodes.<sup>25,84</sup> Graphene is known to induce a face-on orientation (with the  $\pi$  orbital oriented normal to the surface plane) on P3HT chains, which allows better out-of-plane mobility.<sup>25,85</sup> However, the films are fabricated through spin casting, which convolutes the assembly mechanism of P3HT/graphene composites and does not permit in situ characterization of the crystallization. Therefore, the crystallization mechanism remains unclear. To resolve this mechanism, several studies using scanning tunneling microscopy have found that when P3HT is crystallized from highly oriented pyrolytic graphite (HOPG) the distance between backbones along the hexyl chain direction is 1.4 nm.<sup>71,86-88</sup> This is significantly smaller to the typical 1.6 nm distance observed for P3HT films<sup>30</sup> or crystallized by

self-seeding.<sup>89</sup> Epitaxial crystallization of P3HT on HOPG has been invoked to explain this difference, yet the reason for the reduction in the interchain dimension remains unclear.

It is challenging to isolate the P3HT crystallization on nucleating agents given that the polymer can spontaneously crystallize in free solution, adsorb and obscure the graphene surface,<sup>90</sup> thus it is crucial to prevent homogenous nucleation. Therefore, it is key to understand the hysteresis in the crystallization of P3HT to limit the crystallization on the nucleating agents and better understand the mechanism.<sup>48,83</sup> The hysteresis in the crystallization of flexible polymers such as polyethylene (PE) has been extensively studied.<sup>91-94</sup> Interestingly, it was found that the hysteresis window increases in n-alkanes with higher molecular weight due to the creation of a metastable phase for longer chains, which nucleates before the most stable crystals.<sup>91,95</sup> Additionally, it was argued that the hysteresis window in PE increases with molecular weight and plateaus at the chain folding threshold due to incomplete crystallization.<sup>96</sup> In contrast, the hysteresis in crystallization of conjugated polymers has received less attention. In one study, Oh and coworkers<sup>47</sup> studied the effects of solvent in the hysteresis of P3HT crystallization and determined that the better the solvent is for P3HT the narrower the hysteresis. However, the influence of the physical properties of the polymer on the crystallization hysteresis has not been investigated.

Here, we provide insight on the effects of molecular weight, regioregularity and concentration on the stability of supersaturated solutions of P3HT, to better explain the influence of graphene in the crystallization of P3HT. Using molecular weight as independent variable, our results demonstrate a dependence of lamellar thickness (NF width) to the hysteresis window. Additionally, the hysteresis window was optimized to characterize the crystallization of P3HT on HOPG *in situ* using high resolution AFM. From the interchain distances between backbones and hexyl chains indicate that the crystals are of Form I. Due to the possible compatibility of our

crystallization method with roll-to-roll processing, our findings contribute to better understand and perhaps improve film formation in continuous fabrication processes.

### 3.3 Experimental procedures

#### 3.3.1 Synthesis of poly(3-hexyl thiophene)

Poly(3-hexyl thiophene) (P3HT) was synthesized by Grignard metathesis polymerization (GRIM) as explain in Section 2.3.1. Samples 5 and 6 with controlled regioregularity (RR) were prepared by Bumjoon Kim's group at Korea Advanced Institute of Science and Technology (KAIST).<sup>97</sup> The key synthetic feature is that head-to-head coupled 3,4',-dihexyl-2,2'-bithiophene dimer were copolymerized during the Grignard methathesis (GRIM) polymerization of P3HT. As changing the feed ratio, RR of P3HT can be precisely changed while maintaining the controlled nature of GRIM polymerization technique. The remaining polymers were purchased from Rieke Metals (sample 4 and 7) and Sigma Aldrich (sample 8), and used as received. Each polymer was characterized by GPC (Figure 23) and NMR (Figure 24) to determine the listed molecular weights and RRs, respectively.

Table 1. Physical properties of the P3HT used in this study are listed below. The molecular weights given in polystyrene equivalent were measured by GPC and the regioregularity was determined from NMR.

Sample	$M_n$ (kg/mol)	$\bar{D}$	Regioregularity (%)
1	6	1.29	94
2	10	1.33	94
3	12	1.29	96
4	15	1.60	95
5	17	1.70	81
6	21	1.44	88
7	22	1.9	96
8	24	1.89	94



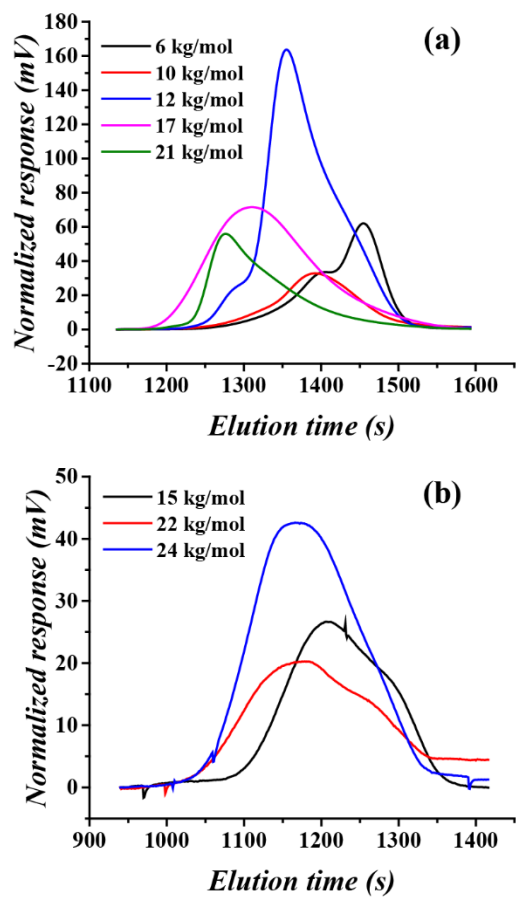


Figure 23: GPC traces obtained using tetrahydrofuran at room temperature (a) and trichlorobenzene at 140 °C (b). The background signal was subtracted for better visualization of the traces.

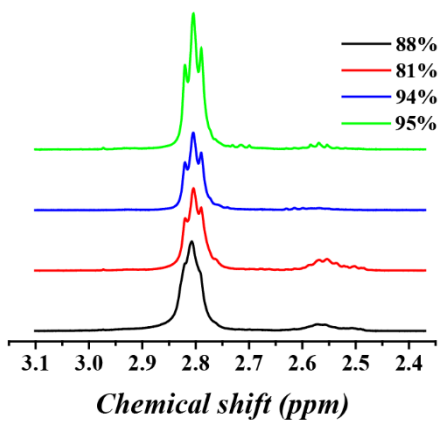


Figure 24: NMR spectra of P3HT with different regioregularity.

### 3.3.2 Crystallization experiments

The melting and crystallization temperatures of P3HT solutions were determined *in situ* using a Hitachi U-3010 UV-vis spectrometer equipped with T2/Hitachi Quantum Northwest temperature controller. This controller controls the temperature with an accuracy of  $\pm 0.3$  °C. The solutions were dissolved at high temperature, and upon cooling to room temperature, transferred to a 1 cm path length quartz cuvette. Once, in the cuvette the solution was reheated to a preset temperature to erase any thermal history. While stirring at 400rpm, the sample was cooled at a 1 °C/min rate, equilibrated for at least 10 min at the lowest temperature, and reheated at 1 °C/min, while monitoring the absorbance of the solution.

The crystallization kinetics of P3HT ( $M_n = 12$  kg/mol) were examined *in situ* using UV-vis. The P3HT solution (0.5 mg/ml) was quenched from 80 °C to 2 °C ( $T_c$  of the polymer) and the absorbance was monitored across time. A relative crystalline fraction was obtained by converting the absorbance at 612 nm to the concentration of NFs. To study the effects of adding graphene in the crystallization kinetics of P3HT a graphene suspension was added to a metastable solution (0.5 mg/mL) of the polymer with a graphene loading of 0.001 mg/mL. Graphene (graphene nanopowder: 12 nm thick, Graphene Supermarket) were suspended by sonicating a 0.05 mg/mL suspension in *m*-xylene for 1 h.

The crystallization of P3HT on the surface of highly oriented pyrolytic graphite (HOPG) was characterized using a Cypher ES AFM with an Arrow UHFAuD tip. Upon injection of a 0.5 mg/mL metastable solution the tip was tuned to around a third (~40 kHz) of the resonance frequency (1400 KHz) of the tip using a target amplitude of 100mV and an amplitude set point of ~50 mV. Although the tip curvature radius is around 10 nm, it is possible that the high drive frequency of the tip allows a sharper region to deliver the molecular resolution observed. The morphologies of the crystalline solutions were inspected by TEM. For this purpose, 0.2 mL of the solution was crystallized at the respective solution crystallization temperature ( $T_c$ ) by

cooling at 1 °C/min and maintaining stirring at 400 rpm. Subsequently, the solution was rapidly transferred into a 20 mL vial equilibrated at  $T_c$ , corrected for the heat transfer delay from the sample stage and the solution, and crystallized for at least 1 h. After soaking a TEM Cu grid in the solution inside the vial, the solution excess was removed using a filter paper at  $T_c$ .

To determine the morphology of the polymer on the surface of graphene flakes, 0.5 mg of graphene flakes were added to 1 mL of a P3HT metastable solution (0.5 mg/mL) and sonicated for 30 min. After heating the solution at 80 °C the solution was left to cool to room temperature and centrifuge at 10 krpm for 30 min to remove remaining dissolved P3HT in the supernatant.

The precipitate was suspended in fresh solvent and drop casted in a TEM grid. TEM shows that NFs are formed on the surface of the graphene flakes Figure 25. The NF width was estimated by measuring 60 NFs except for the NFs crystallized on graphene with error bars representing the standard error on the average.

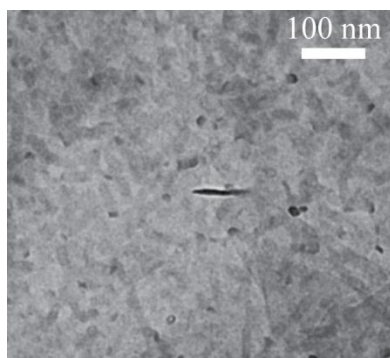


Figure 25. P3HT crystallized on a graphene flake.

### 3.3.3 Absorption coefficient of P3HT nanofibers

Using a method previously described in our group<sup>83</sup>, the absorption coefficient of NFs in solution was determined to be  $44 \pm 3 \text{ mL cm}^{-1} \text{ mg}^{-1}$  (Figure 26 and Figure 27). Using Beer-Lambert Law the absorbance at 612 nm, coming from the aggregated state of P3HT, can be converted into an approximation of the NF concentration.

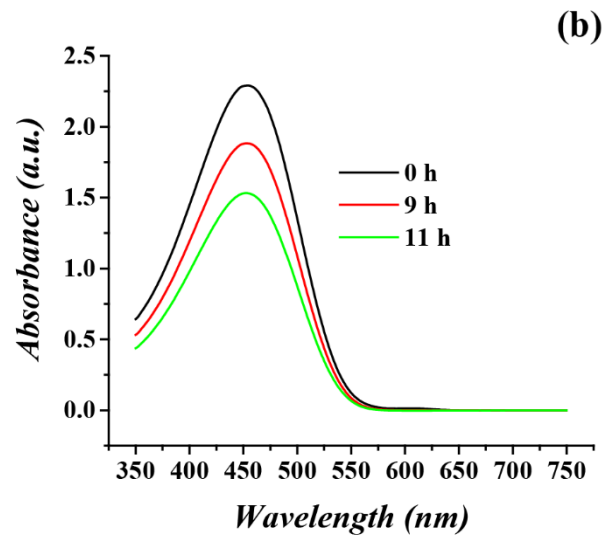
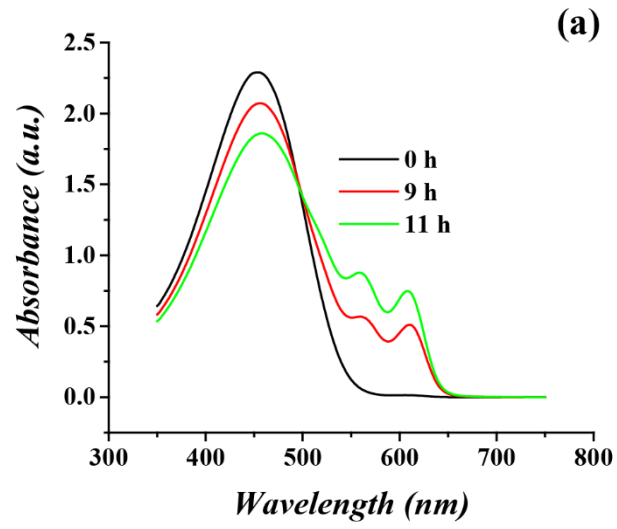


Figure 26: UV-vis of P3HT crystallized for different at different period of times (a) and after filtration (b).

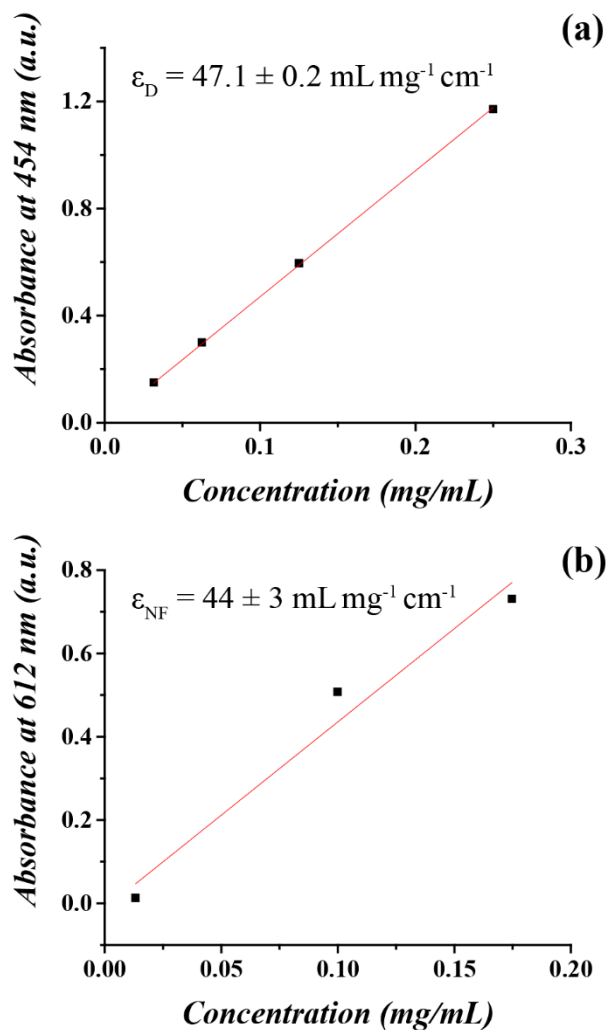


Figure 27: Calibration curves of dissolved (a) and crystallized P3HT in *m*-xylene (b).

### 3.4 Results and discussion

#### 3.4.1 Hysteresis in the crystallization of P3HT

To characterize P3HT crystallization in solution UV-vis is a powerful tool since it has been demonstrated that the crystallization and melting temperatures of P3HT can be characterized using the evolution the vibronic peaks upon the  $\pi$ -stacking of the chains.<sup>83</sup> As previously shown, the appearance of the vibronic peak at 612 nm is identified as the crystallization temperature ( $T_c$ ), while its disappearance indicates the melting point ( $T_m$ ) of the solution. As show in Figure 28a. it follows that P3HT has a similar hysteretic behavior as PE, where the hysteresis increases with

molecular weight and plateaus at high molecular weight.<sup>91,94</sup> Interestingly, previous studies,<sup>46,98</sup> have seen that P3HT when crystallized into nanofibers (NFs) tends to fold at molecular weights higher than 10 kg/mol polystyrene equivalents. Our P3HT samples, crystallized at their respective  $T_c$ , showed a NF morphology as characterized by TEM in Figure 29. In this structure, the NF width represents the lamellar thickness, thus as previously showed the chain folding threshold can be determined from the point where the NFs width deviates from the contour length of the polymer. As seen in Figure 28, the NF width deviates from the contour length chain beyond  $M_n = 12$  kg/mol indicating chain folding. Our molecular weight threshold ( $M_n = 12$  kg/mol) agrees with P3HT previous studies.<sup>46,98</sup>

One key advantage of working with P3HT is that the number of defects in the crystallized structures can be increased by reducing the polymer's regioregularity (RR) (head-to-tail coupling).<sup>97</sup> According to Meyer and coworkers<sup>96</sup> the hysteresis window should increase with the number of defects.

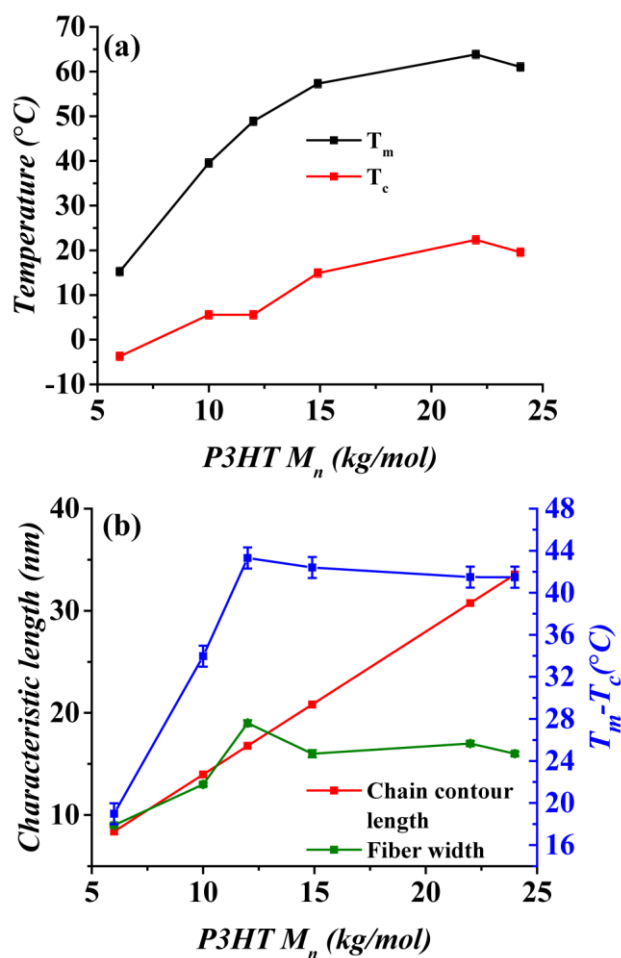


Figure 28: Melting ( $T_m$ ) and crystallization ( $T_c$ ) temperatures with the corresponding hysteresis window ( $T_m - T_c$ ) of highly regioregular P3HT(a). Correlation between the hysteresis window chain folding by comparing the fiber width against the polymer contour length as function of molecular weight (b). The chain contour length was determined from the corrected molecular weight by dividing the overestimated GPC molecular weight by 1.7.<sup>71,99</sup>

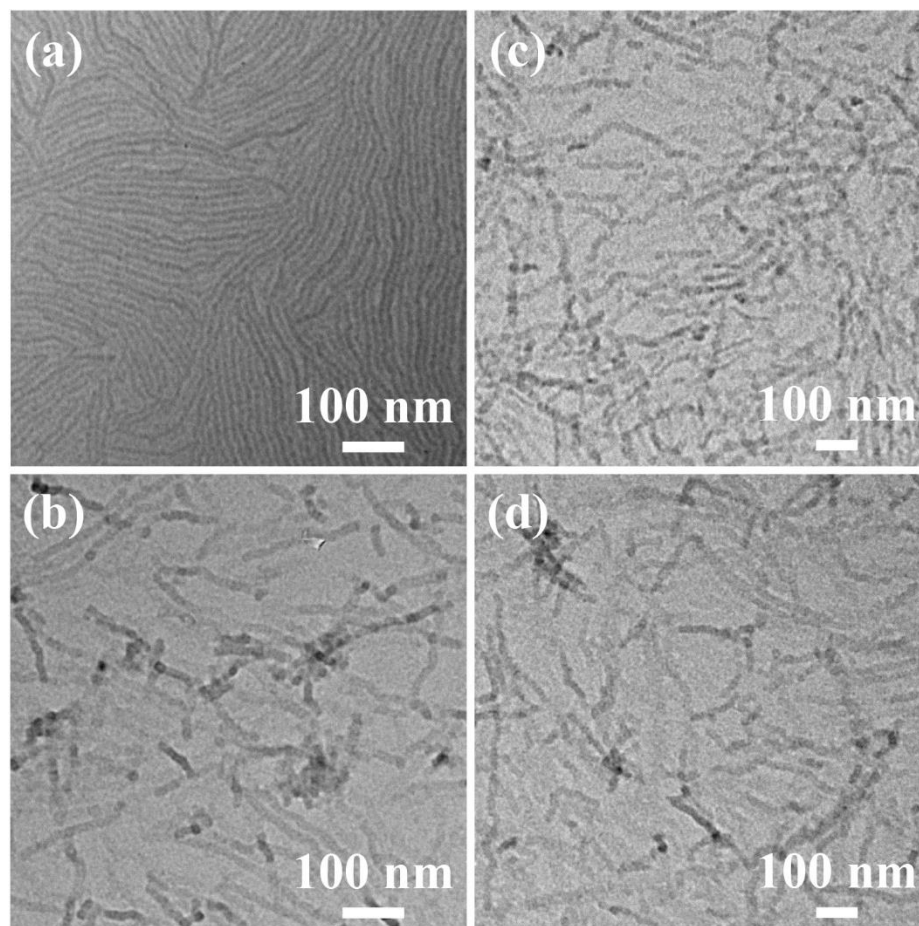


Figure 29: TEM images of P3HT with different molecular weights measured in polystyrene equivalent: 6 kg/mol (a), 10 kg/mol (b), 12 kg/mol (c), 22 kg/mol (d), crystallized at their respective crystallization temperatures when cooled at 1 °C/min from 80°C.

However, our results shown in Figure 30a do not exhibit a correlation between the hysteresis window and RR. The NF width was found to be 16-17 nm across the RR range of 88-95% (Figure 30a). Note that at RR = 81%, the polymer did not crystallize significantly to collect NFs for TEM imaging. Our results indicate that crystallization hysteresis and RR are uncorrelated. Also, Figure 30b demonstrates that the hysteresis decreases with concentration. This can be explained by a reduction in the nucleation barrier with increasing supersaturation.



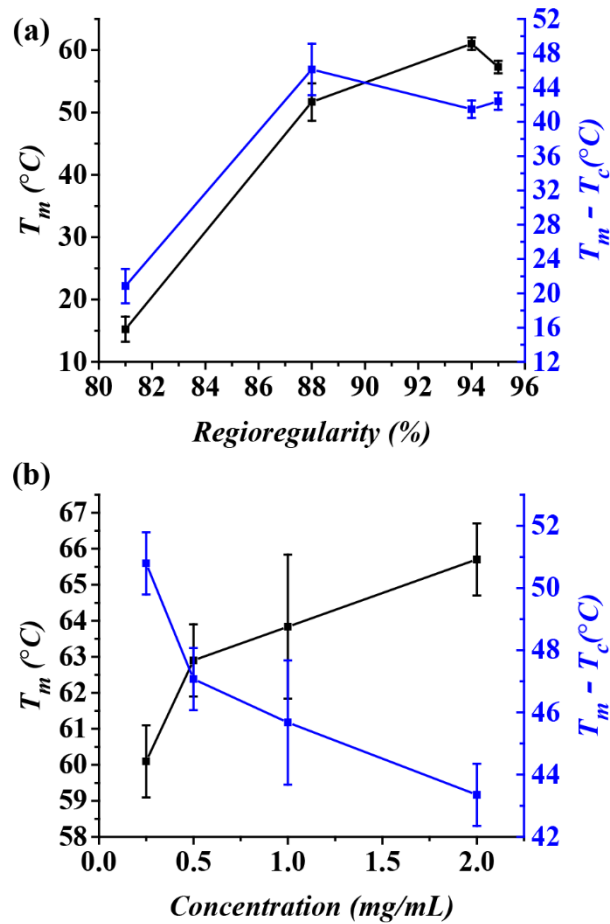


Figure 30: Melting point and hysteresis window as a function of regioregularity (a) and concentration (b) of P3HT.

### 3.4.2 Crystallization mechanism

Rapid crystallization is important for the formation of the desired structures in a fast-paced production of electronic devices.<sup>5</sup> The Avrami model is a suitable tool to provide better understandings of the kinetics and the formation mechanism of crystals.<sup>100,101</sup> The model predicts the crystallinity fraction ( $x$ ) increment as function of time ( $t$ ) is given by:

$$1 - x(t) = e^{(-kt^n)} \quad [3]$$

Where  $k$  is the crystallization rate pre-factor and  $n$  is the Avrami exponent, which typically indicates the growth dimensionality, mechanism of nucleation and the rate determination process.

It has been found that P3HT shows Avrami exponents of  $n = 0.58-1.26$  in the melt, indicating

heterogeneous and one-dimensional crystallization mechanism.<sup>102</sup> Yang and coworkers<sup>103</sup> found Avrami's exponents of 3-4 for the non-isothermal crystallization of P3HT from graphene flakes. Unfortunately, it was concluded the Avrami model could not describe the non-isothermal crystallization of P3HT from reduced graphene oxide. Therefore, to better understand the influence of graphene on the crystallization kinetics of P3HT, metastable solutions of P3HT  $M_n = 12$  kg/mol were prepared at 0.5 mg/mL, and incubated at the crystallization temperature measured in the hysteresis experiments. The polymer crystallization kinetics were studied and compared to the kinetics upon addition of graphene flakes with a surface area of  $\sim 1.2$  cm<sup>2</sup> (comparable to the graphene surface area used in our previous work).<sup>83</sup> As expected, P3HT crystallized from graphene into NFs of  $15.0 \pm 0.5$  nm in width (Figure 25). Interestingly, Figure 31 illustrates that, within the period studied, the crystallization proceeds faster in the presence of graphene and even reaching higher crystalline fractions when compared to solutions of P3HT alone. The Avrami model (Figure 31b) was fitted to the data from pristine P3HT and graphene/P3HT composite crystallization resulting in  $n = 1.50 \pm 0.01$  and  $n = 1.42 \pm 0.02$ , respectively. The increments in the crystallization rate,  $k$  upon addition of graphene, the reduction in  $n$  indicate that graphene is a nucleating agent for one-dimensional P3HT crystals. This agrees with previous studies on carbon nanotubes<sup>104</sup> since they both serve as good nucleating agent for P3HT to crystallize into NFs.

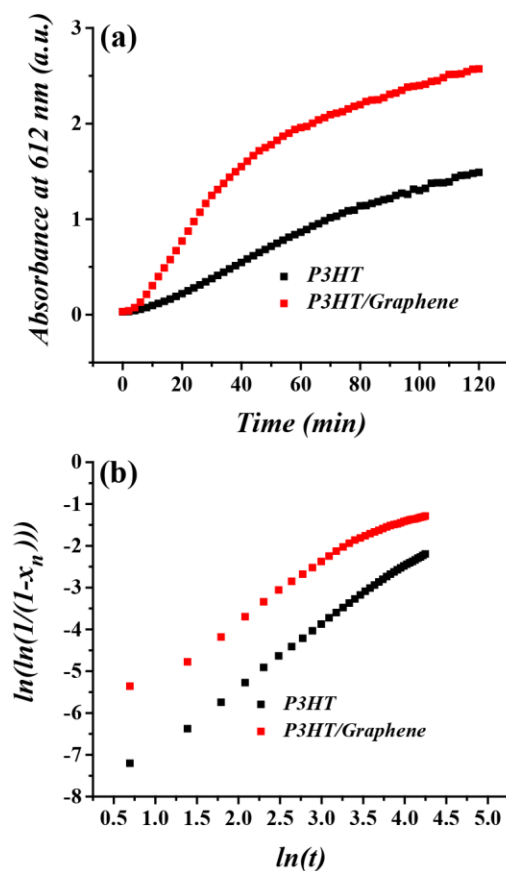


Figure 31: Kinetics of crystallization of pristine P3HT at 0.5 mg/mL as characterized by UV-vis spectroscopy and upon addition of graphene flakes (a). Crystallization kinetics fitted to the Avrami model (b).

Table 2: Avrami parameters summary.

Graphene loading ( $\mu\text{g/mL}$ )	n	k ( $\times 10^{-4} \text{ min}^{-n}$ )
0	$1.50 \pm 0.01$	2
1	$1.42 \pm 0.02$	13

Given the influence of the processing parameters in the morphology evolution of conjugated polymers, there is great interest in characterizing the formation of thin films *in situ*.<sup>76</sup> The hysteresis in the crystallization of P3HT permits the generation of metastable solutions suitable for template crystallization from graphene and for tuning the crystallization kinetics for *in situ* studies.<sup>83</sup> Therefore, we have employed *in situ* AFM to characterize this transition and propose a

formation mechanism. A metastable solution was injected into a freshly cleaved HOPG surface, which prevented adsorption of preformed crystals on the surface and any defects coming from the conventional transferring process of graphene. Figure 32 shows that P3HT chains adsorb into non-ordered domains, which include chain folded chains, and crystallize into NF nuclei. Note that the unresolved areas in these images result from the dynamic nature of the system, where the chains can rotate and move, as previously observed by scanning tunneling microscopy (STM).<sup>105</sup>

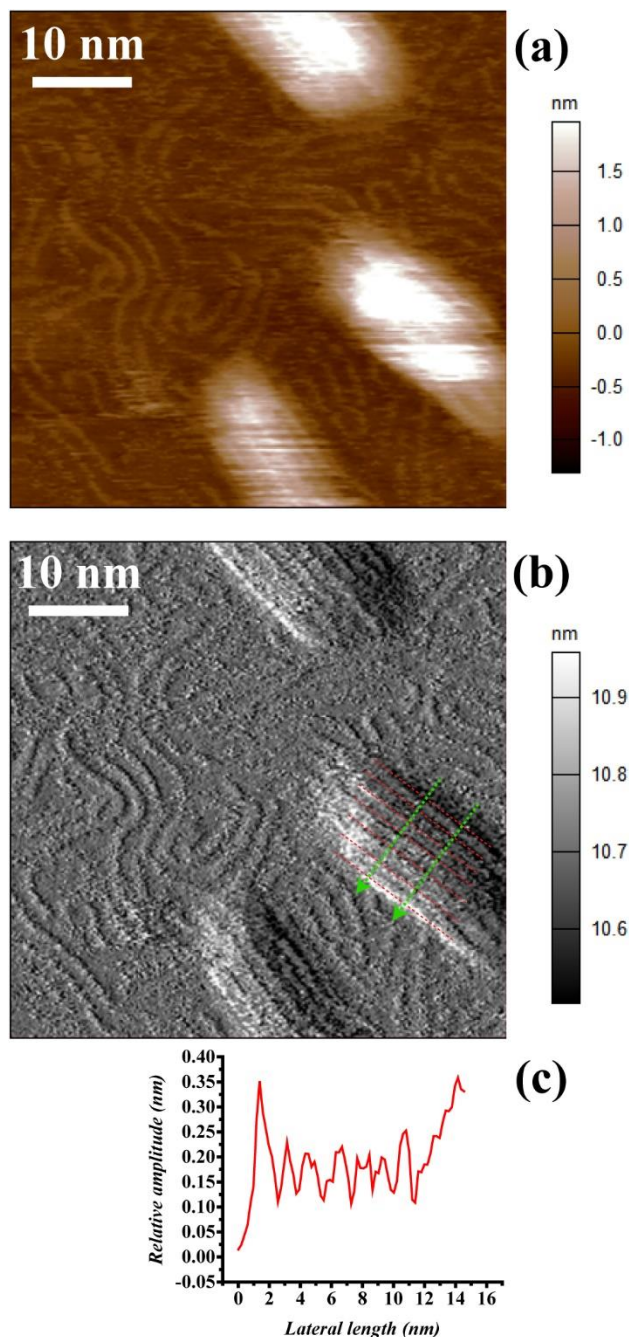


Figure 32: P3HT crystallizing on HOPG as characterized by AFM *in situ* and visualized using the height channel (a) and the amplitude channel (b). The segmented lines indicate the interchain distance ( $16 \text{ \AA}$ ) in along the *a* axis. An amplitude profile from the rectangular area on (b) shows the steps on the NFs (c).

The faster crystallization of P3HT with higher molecular weight ( $M_n = 22 \text{ kg/mol}$ ) reduces the resolution even further (Figure 33). In our previous study,<sup>83</sup> we attributed the larger lateral dimensions of the NFs crystallized from HOPG ( $27.4 \pm 0.4 \text{ nm}$ ) to convolution effects of the 10

nm radius of the tip with the original NF<sup>106</sup> ( $16 \pm 1$  nm). However, our AFM images show P3HT chains on the surface of HOPG. Therefore, the NF nuclei are not convoluted by the tip, but a possible result of preferential fractionation to large molecular weight or the incorporation of multiple chains in the long lateral axes of the NF nuclei. Additionally, it is evident that the crystals have steps systematically ordered across the shorter dimension of the NF nuclei (Figure 32). Based on the crystal dimensions previously observed by TEM<sup>89,107</sup> and STM<sup>4,65</sup> the distance between steps can be assigned to the (100) direction of a P3HT crystal. Indeed, the distance between crystals is  $16.7 \pm 0.7$  Å in agreement with what has been found by electron diffraction for P3HT crystals of Form I.<sup>89,107</sup> Remarkably, as seen in Figure 34 AFM also resolves the hexyl chains of a series of P3HT chains with repetitive distances of  $7.7 \pm 0.2$  Å and  $17.1 \pm 0.9$  Å between them, respectively. Consequently, the crystals are indeed of Form I because the  $7.7 \pm 0.2$  Å can be assigned to the *c* axes. STM studies on P3HT have been unable to measure structures taller than a bilayer due to the vanishing signal in the out-plane direction beyond a P3HT monolayer, thus the origin of the repetitive distance between backbones of 15 Å remains unclear.<sup>86,108,109</sup> We propose that these domains of organized monolayers observed by ATM serve as a metaphase for P3HT to assemble into Form I crystals.

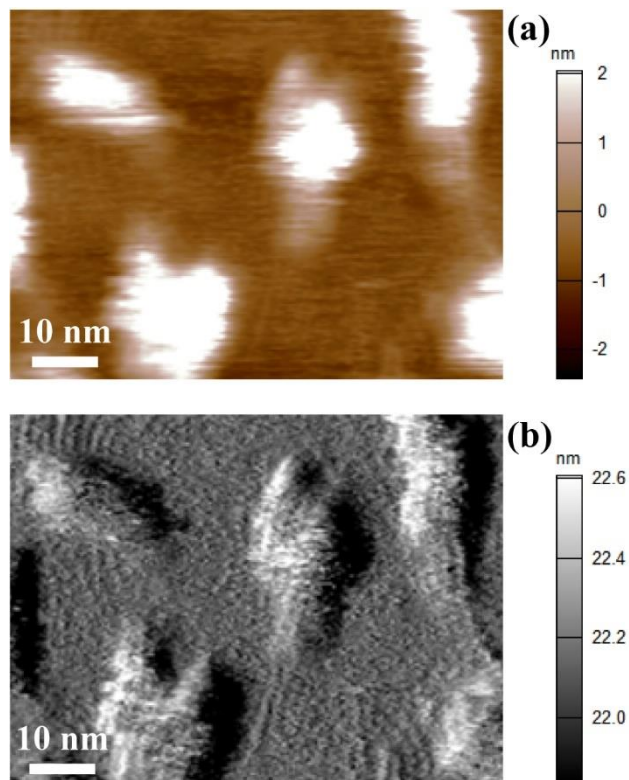


Figure 33: P3HT ( $M_n = 23$  kg/mol) crystallizing on HOPG as characterized by AFM *in situ* and visualized using the height channel (a) and the amplitude channel (b).

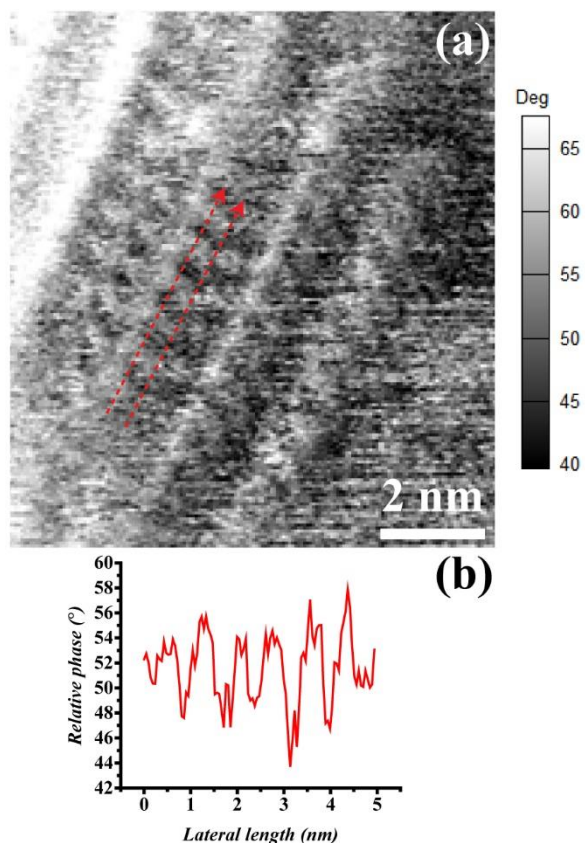


Figure 34: Phase channel of *in situ* AFM showing P3HT chains on the surface of a nanofiber nucleus (a) with the phase contrast profile obtained from the rectangular area averaged between red lines (b) as illustrated on (a).

It is widely accepted that flexible chains will always crystallize first in a chain-folded macro conformation.<sup>110</sup> As seen in Figure 35, multiple AFM scans confirm that the disorganized chains can organize into domains of extended chains and nucleate a NF. The nucleation of a NF can occur within 30 s. Not surprisingly, the interchain distance of P3HT with a  $M_n = 22$  kg/mL is  $16.3 \pm 0.6$  Å (Figure 33) in good agreement with the results found for the lower molecular weight (Figure 32).



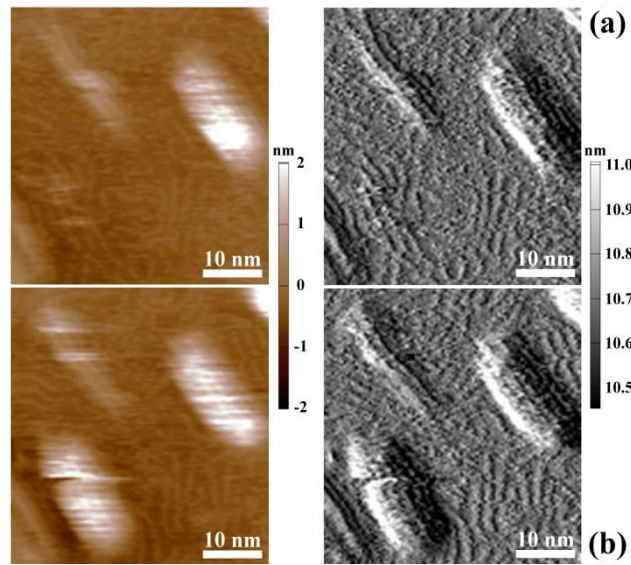


Figure 35: *In situ* AFM illustrating P3HT nucleus forming on HOPG from an ordered monolayer domain (a) into a nanofiber nucleus (b).

### 3.4.3 Transition in the orientation of P3HT nanofibers

Selective crystallization on nucleating sites can provide a practical route to achieve template crystallization of P3HT nanostructures with the desired orientation. The hysteresis in the crystallization of P3HT serves as a handle to prevent homogenous crystallization since the polymer solution has a higher melting temperature than its crystallization temperature<sup>47</sup>. Given the dispersity in molecular weight and variations in the degree of regioregularity per chain, different solubility degrees are attained from each polymer batch. It was determined, by visual inspection (i.e. no change in color of the solution), that crystallization at room temperature of highly regioregular (90 %) P3HT ( $M_n = 13$  kg/mol polystyrene equivalent,  $D = 1.19$  as obtained from gel permeation chromatography) was prevented if 10 %<sub>v/v</sub> of chlorobenzene (i.e. a good solvent for P3HT) is added to the solution at a 0.5 mg/mL concentration (90 %<sub>v/v</sub> *m*-xylene). To obtain template crystallization of P3HT and characterize the graphene films, silicon and indium tin oxide (ITO) were used as supporting substrates. Graphene was fabricated through chemical vapor deposition, which consisted of mostly bilayer graphene (BLG), as characterized by UV-vis and Raman spectroscopy (Figure 36). A thin layer (9 nm) of molybdenum trioxide ( $\text{MoO}_3$ ) was deposited on glass substrates half-coated with ITO. The  $\text{MoO}_3$  film served as a buffer layer for facilitating hole-extraction from P3HT onto graphene.

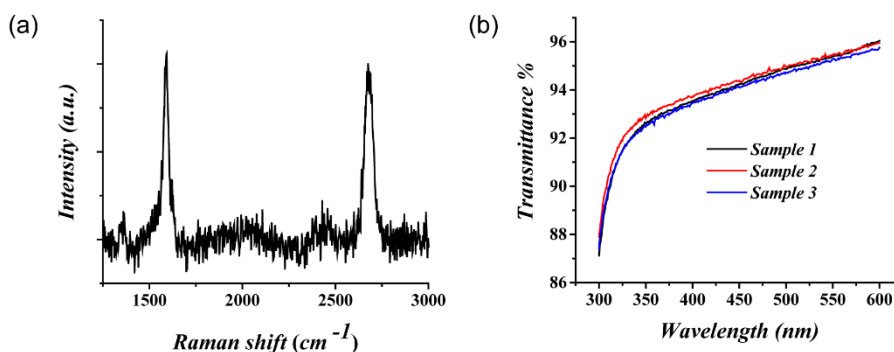


Figure 36: Raman spectroscopy spectrum of BLG deposited on glass substrate pre-coated with MoO<sub>3</sub>/ITO (a). UV-vis spectrum of BLG deposited on graphene (b).

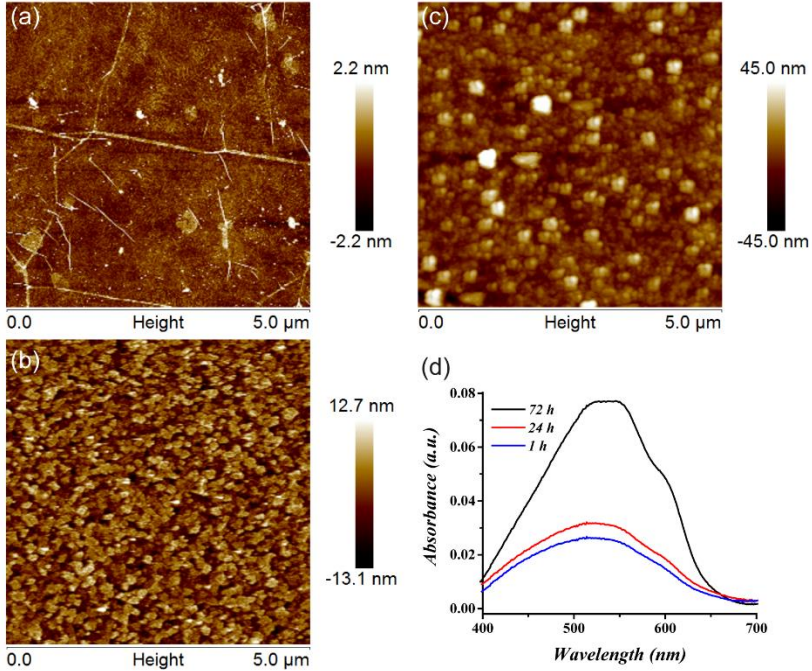


Figure 37: AFM images of BLG as transferred on a silicon oxide substrate (a); MoO<sub>3</sub> exposed surface (b) and BLG after 72 h of incubation in a P3HT solution (c). UV-vis absorbance of P3HT crystallized from BLG on MoO<sub>3</sub> to different extends (d).The intermolecular interactions between

P3HT and graphene induce the P3HT to orient face-on with respect to the substrates<sup>56</sup>. Previous studies have shown that the orientation of the molecules affects energy levels of the material<sup>111,112</sup>. In the case of P3HT it is expected that a change of chain orientation from face-on to edge-on would reduce the highest occupied molecular orbital (HOMO)<sup>112</sup>. In solution, P3HT NFs can grow to be ~1 μm in, but if they grow out-of-plane and longer than ~ 10 nm, then surface tension is sufficient to collapse them onto an in-plane orientation<sup>83</sup>. To understand this transition in orientation, ultraviolet photoelectron spectroscopy (UPS) and near edge x-ray absorption fine structure (NEXAFS) were employed. UPS allows access to the intrinsic electronic characteristics of the films studied, when compared to a metallic standard such as Au. The energy of the UPS beam was verified, using an Au standard, to have an energy of  $E_p = 94.76$  eV calculated using the

following relation:

$$E_p - WF_{Au} = \Delta E_k \quad [4]$$

where the work function of Au is assumed to be  $WF_{Au} = 5.1$  eV, and the measured difference between the secondary electron cutoff ( $E_{SEC}$ ) and the midpoint of the valance band with the highest kinetic energy of Au is  $\Delta E_k = 89.66$  eV. The UPS spectra are shown in Figure 38. As the P3HT film grows thicker on graphene, the HOMO of P3HT monotonically decreased from 5.1 eV to 4.8 eV, values which agree with previous measurements<sup>113</sup>. These values were determined using the following equation:

$$E_p - (E_{val} - E_{SEC}) = HOMO \quad [5]$$

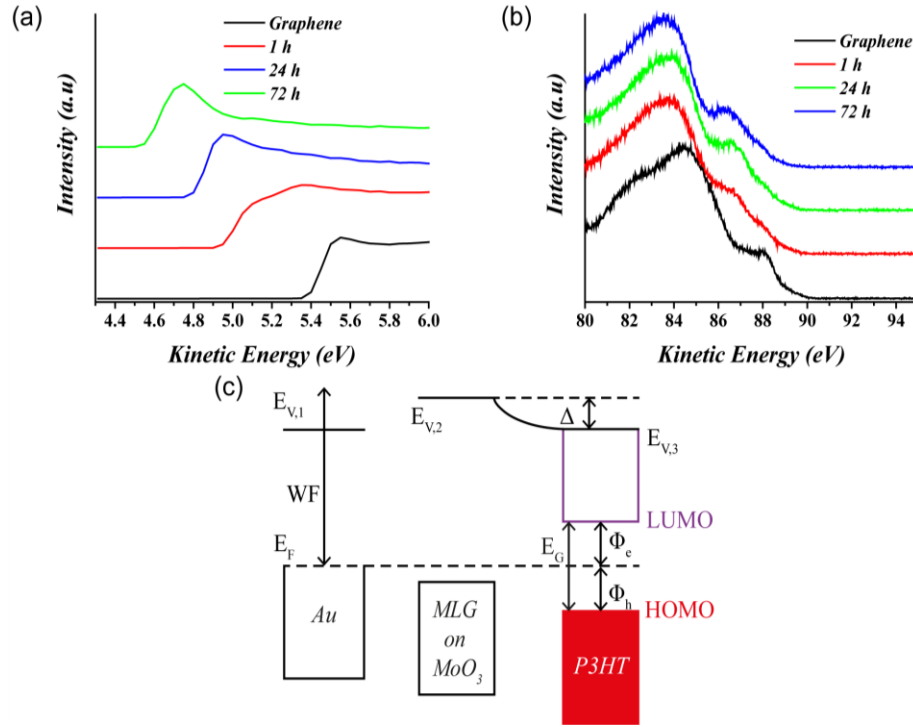


Figure 38: UPS spectra of P3HT crystallized from BLG on MoO<sub>3</sub> at the secondary electron cutoff region (a) and their respective valance bands (b). Schematic representation of the energy levels of the different layers of the sample (c), where  $E_{val}$  is the onset of the valance bands. The shift in

vacuum levels of the different materials relative to Au is the interfacial dipole energy ( $\Delta$ ), while

the difference between  $E_F$  and HOMO yields the hole-extraction energy barrier ( $\Phi_h$ ).

Unfortunately, UPS does not provide information about the lowest unoccupied molecular orbital

(LUMO). But from the onset of the UV-vis absorbance spectrum at lowest energy region the

optical energy gap can be calculated, which if added to the HOMO results in the LUMO and

allows the calculation of the electron-injection energy barrier ( $\Phi_e$ ). The calculated parameters are

summarized in Table 3.

Table 3: Electronic characteristics of P3HT films crystallized from BLG on MoO<sub>3</sub>.

Time (h)	$E_G$ optical (eV)	$\Delta$ (eV)	$\Phi_h$ (eV)	$\Phi_e$ (eV)	HOMO (eV)	LUMO (eV)
1	1.8	0.35	0.38	1.45	5.1	3.3
24	1.8	0.5	0.36	1.3	4.9	3.1
72	1.8	0.75	0.44	1.05	4.8	3

Despite the possibility that secondary electrons can escape from below the P3HT film, the shape of the valance bands is very similar for all P3HT films, thus the contribution of the underlying substrate can be ignored. This implies that there is a transition in the chain orientation of P3HT from face-on to edge-on.

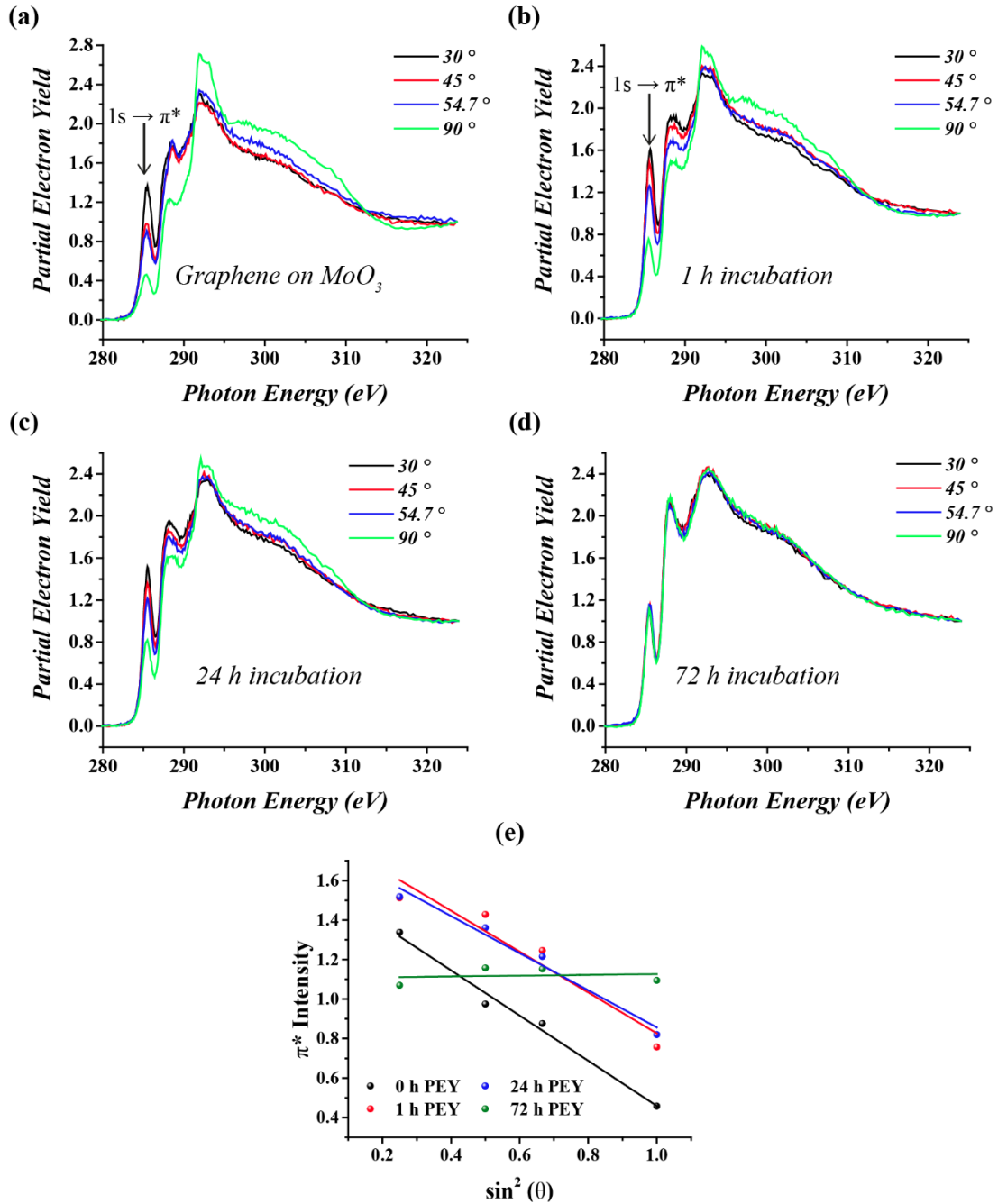


Figure 39: Spectra obtained from NEXAFS operated on partial electron yield mode of BLG on MoO<sub>3</sub> (a); P3HT crystallized for 1 h (b), 24 h (c) and 72 h (d). Linear fittings of the 1s → π\* C=C resonance intensity as a function of incident angle (e). NEXAFS is a powerful technique to determine the conformation of molecules in ultra-thin films (i.e. a monolayer) due to its high sensitivity for the direction of the transition dipole along the molecular orbitals<sup>114</sup>. The angle dependence of the intensity from the resonance around 285 eV, which is attributed to the 1s → π\* C=C orbitals, is typically employed to determine molecular orientation<sup>115</sup>. Figure 39e shows NEXAFS spectra measured at four incident angles ( $\theta = 30^\circ, 45^\circ, 54.7^\circ$  and  $90^\circ$ ) of P3HT crystallized to different for different extends (1 h, 24 h, 72 h) and the background of BLG on MoO<sub>3</sub>. The NEXAFS measurements were carried out with *p*-polarized X-rays at the Pohang Accelerator Laboratory (beamline BA07) under partial electron yield (PEY) mode with bias of 900 V that yields a probing depth of ~10 nm. The figure of merit dichroic ratio (*R*) provides quantifying method for the orientation of molecules. From Figure 39 it is evident that the intensity of the 1s → π\* C=C resonance is proportional to  $\sin^2\theta$ , where *R* is the proportional constant is. It is expected that in films with no preferential orientation will show *R* = 0, for a perfect face-on orientation *R* = -1, while *R* ≈ 0.7 for edge-on<sup>114</sup>. Figure 39 shows a transition from a face-on orientation to an edge-on orientation, although the contribution of graphene to the change in orientation due to the overlapping of the resonances with P3HT remains a challenge. Despite this, the combination of the results of NEXAFS and UPS depicts a transition of a face-on orientation of P3HT to edge-on chains as the film grows thicker.

Table 4: Dichroic ratio values for the P3HT films.

Time (h)	Dichroic ratio (R)
0	1.1 ± 0.1
1	1.0 ± 0.2
24	0.9 ± 0.1
72	0.0 ± 0.1

To preserve the face-on orientation of the P3HT nanostructures after 6 days of crystallization, the wet substrates were introduced into a highly-concentrated solution (20 mg/mL) of indene C<sub>60</sub> bisadduct (ICBA) in *m*-xylene. The ICBA matrix can potentially lock the nanostructure in place during solvent evaporation and complete the active layer for OPV devices. Grazing incidence wide-angle X-ray scattering (GIWAXS) measurements of a pristine P3HT film crystallized from graphene revealed strong (h00) reflections and clear (010) reflection along the out-of-plane direction  $q_z$  ( $I_{(010)z}$ ), as well as (h00) reflections and a clear (010) peak along the in-plane direction  $q_{xy}$  ( $I_{(010)xy}$ ), this is consistent with a combination of crystalline edge-on and face-on molecules as seen in Figure 40a. Surprisingly, Figure 41b shows that the P3HT nanostructure embedded in ICBA has a combination of both edge-on and face-on orientations. Additionally, a clear amorphous ring centered at  $q = 1.3 \text{ \AA}^{-1}$  characteristic of ICBA is observed. The peak at around  $q = 0.7 \text{ \AA}^{-1}$  can be attributed to the characteristic size of P3HT/ICBA structures produced during solvent evaporation. To better quantify the effects of the ICBA matrix on the P3HT orientation, a bilayer of P3HT (bottom) with ICBA (top) was fabricated as a control experiment. Although the analysis is complicated due to the presence of ICBA scattering, we can still estimate the level of orientation by comparing the relative strengths of the scattering at the P3HT peak locations, presented in Table 5. The ratio of the relative intensities of  $I_{(010)z}$  and the (100) reflection ( $I_{(010)z}$ ), is higher for P3HT embedded in ICBA ( $I_{(010)z}/I_{(100)z} = 0.20$ ) than for the bilayer sample ( $I_{(010)z}/I_{(100)z} = 0.06$ ). The opposite is observed for the intensity ratios in-plane, where the bilayer ratio is higher ( $I_{(010)xy}/I_{(100)xy} = 0.63$ ) than for the ICBA-embedded P3HT ( $I_{(010)xy}/I_{(100)xy} = 0.35$ ). Despite the unknown ICBA contribution to the intensity ratios, these results are evidence that the ICBA matrix can preserve the face-on orientation during solvent evaporation.



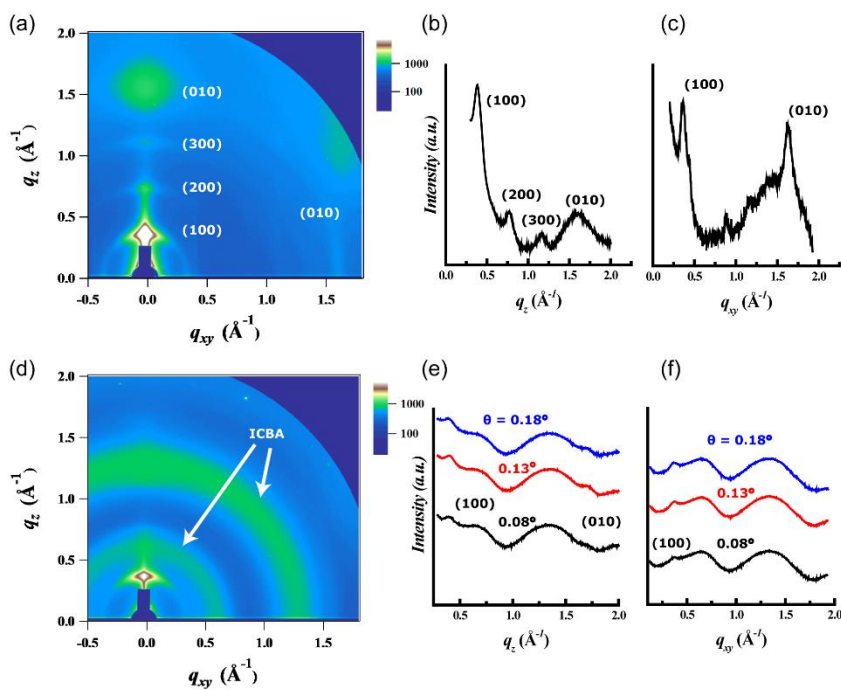


Figure 40: 2D GIWAXS measurements of P3HT films crystallized for 6 days from graphene on Si as prepared (a) and embedded in a ICBA matrix during solvent evaporation (b) with their respective spectra along the out-of-plane (b, e) and the in-plane directions (c, f).

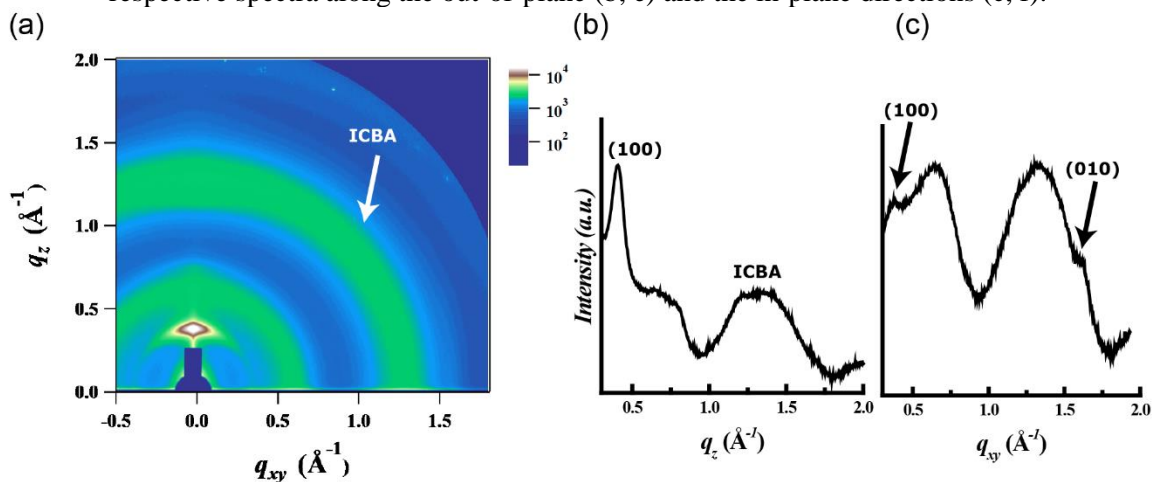


Figure 41: 2D GIWAXS measurements of P3HT films crystallized for 6 days from graphene on Si with a ICBM layer on top prepared with the spectra along the out-of-plane (b) and the in-plane directions (c).

Table 5: Intensity ratios, obtained from GIWAXS, for the specified reflections of P3HT crystallized from graphene.

Sample	ICBA/P3HT bilayer	ICBA embedded P3HT
$I_{(010)_z}/I_{(100)_z}$	0.06	0.20
$I_{(010)_{xy}}/I_{(100)_{xy}}$	0.63	0.35

### 3.4.4 Alternative materials for graphene templated crystallization

To extend the method of templated crystallization of conjugated polymers from graphene surfaces beyond P3HT, the solution crystallization of poly[2,5-bis(3-tetradecylthiophen-2-yl)thieno[3,2-*b*]thiophene] (PBTTT) was analyzed. Using a molecular weight of  $M_n = 28$  kg/mol with  $\bar{D} = 1.58$  (as measured by GPC in polystyrene equivalent), a solution of the polymer was prepared by mixing it in orthodichlorobenzene (ODCB) at 80 °C (0.05 mg/mL). The solution was brought to room temperature and transferred to a 1 mm cuvette in the UV-Vis spectrometer (Figure 42). UV-vis spectroscopy indicates that the shoulder at around 600 nm does not emerge above 7 °C as the solution is cooled down from 55 °C, which suggests the polymer is aggregating<sup>116</sup>. On the other hand, the absorbance persists at higher temperatures. This makes PBTTT a potential candidate for templated crystallization from graphene substrates.

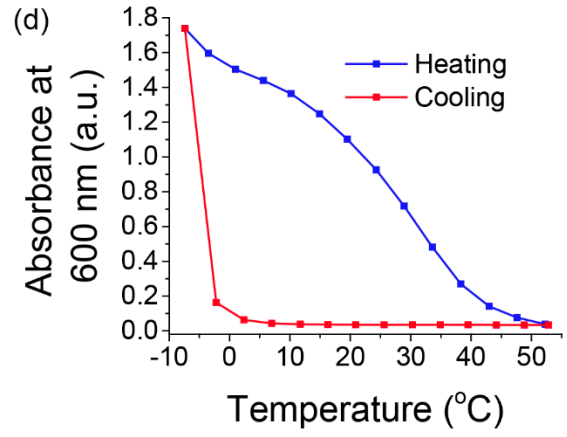
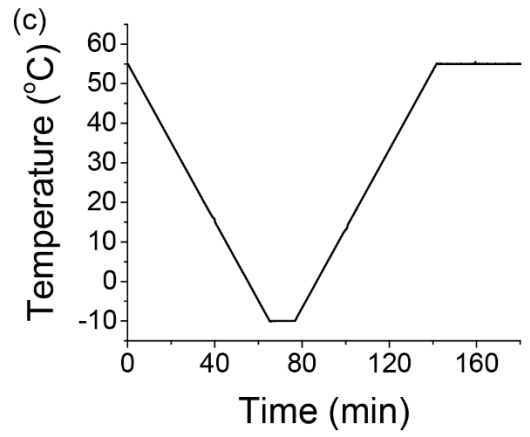
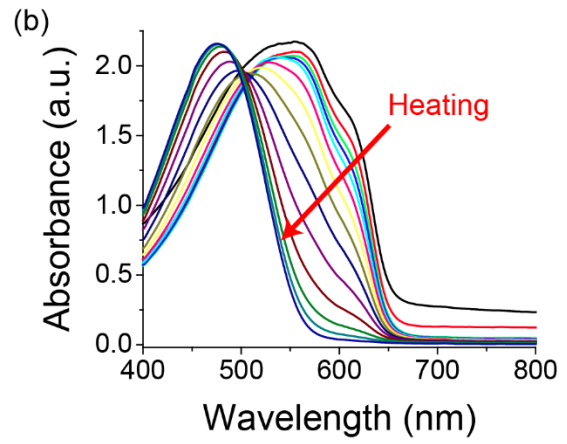
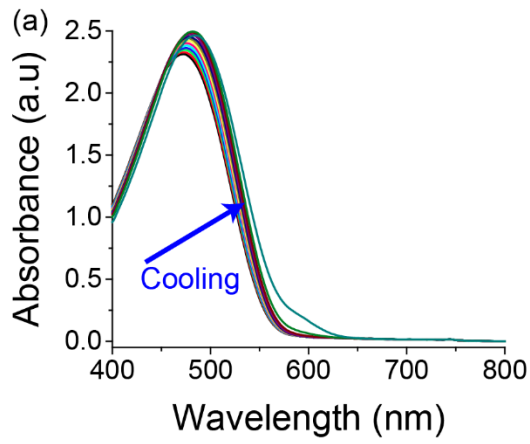


Figure 42: The hysteresis between crystallization and melting of PBTTT NFs. UV-vis spectra of 0.05 mg/mL solution of PBTTT in ODCB during cooling and (a) heating (b), along with the temperature profile employed (c), and absorbance of aggregated PBTTT at 600 nm (d). The

crystallization of PBTTT was characterized *in situ* using AFM (Figure 43). A 0.05 mg/mL was injected on a HOPG freshly cleaved substrate as previously described for P3HT. It was found that

the lateral dimension of the PBTTT nuclei are  $21 \pm 1$  nm and  $8.2 \pm 0.5$  nm. Moreover, the orientation angle of the longest lateral dimension of the NF with respect of an arbitrary angle on the substrate is distributed into three sets of angles  $60^\circ$  apart from each other. This correspond to

the crystallographic axes of HOPG. Consequently, PBTTT follows a similar out-of-plane crystallization as P3HT, where NFs are crystallizing out-of-plane from HOPG.

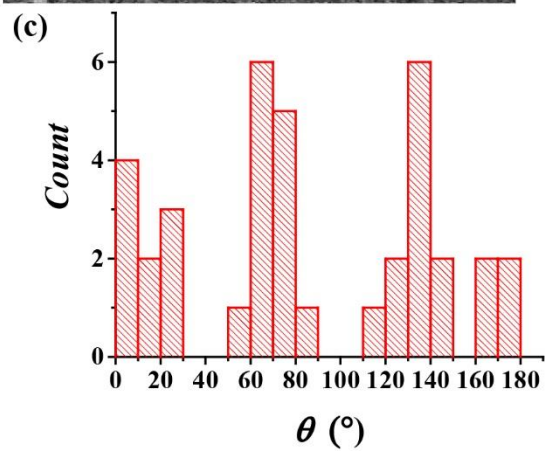
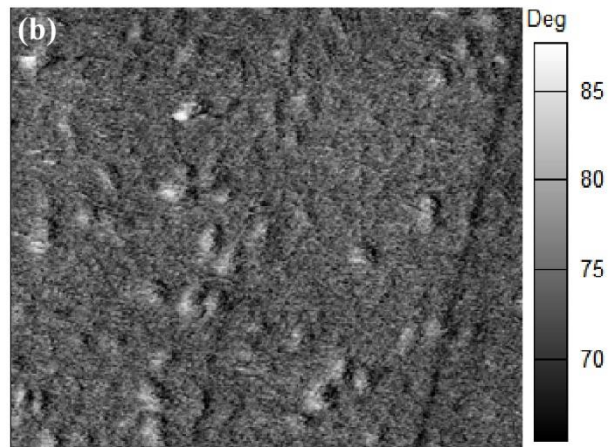
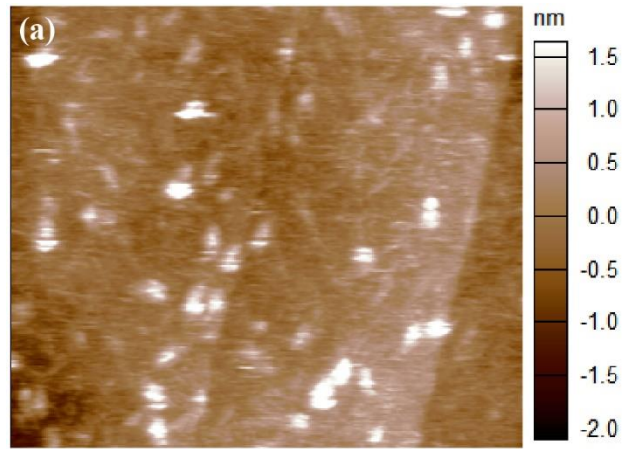


Figure 43: PBTTT crystallizing on HOPG as characterized by AFM *in situ* and visualized using the height channel (a) and the phase channel (b). In-plane orientation angle of the lateral long axis of the NF with respect of an arbitrary angle of the HOPG surface (c). The high-resolution images

shown in Figure 44 demonstrate PBTTT adsorbed on HOPG and crystallizing into NFs.

Interestingly, the chains assemble into NF nuclei and the AFM can remove them, leaving a monolayer behind (Figure 45). Surprisingly, the interchain distance in the (100) direction obtained by AFM ( $26.4 \pm 0.3 \text{ \AA}$ ) is larger than expected for PBTTT ( $21.5 \text{ \AA}$ )<sup>117</sup> crystallized in the bulk. Contrary to P3HT, it was not possible to observe the steps on the surface of PBTTT crystals, thus the interchain distance was characterized from organized monolayer-domains as depicted in Figure 45. The larger interchain distance can be attributed to ordered metastable domains that will transform into the typical packing structure away from the HOPG surface. Moreover, PBTTT selectively crystallizes into NFs from graphene as seen by SEM (Figure 46).

As illustrated in Figure 46b, (*h*00) reflections are observed by GIWAXS after 24 h of crystallization. Interestingly, the interchain distance was  $21.5 \text{ \AA}$ , which suggests a transition of a metastable ordered phase on the surface of graphene into bulk crystallization.

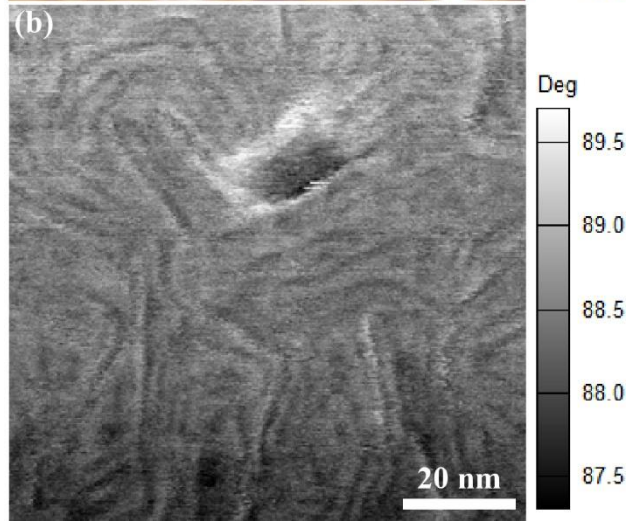
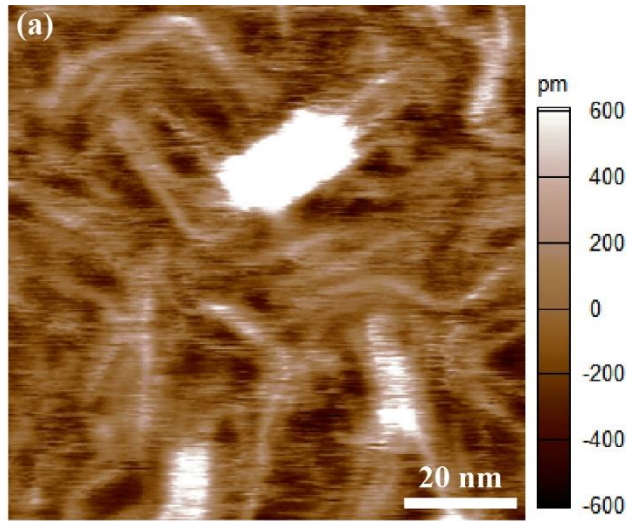


Figure 44: High-resolution AFM characterization *in situ* of PBTTT NFs crystallizing on HOPG and visualized using the height channel (a) and the phase channel (b).

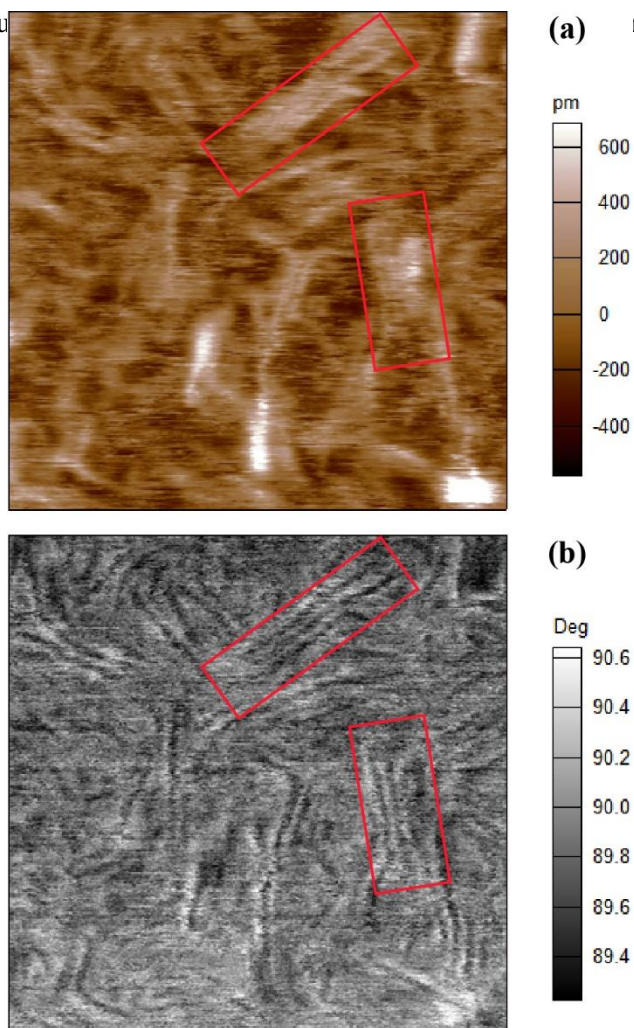


Figure 45: High-resolution AFM characterization *in situ* of PBTTT crystallizing on HOPG into organized domains visualized using the height channel (a) and the phase channel (b).



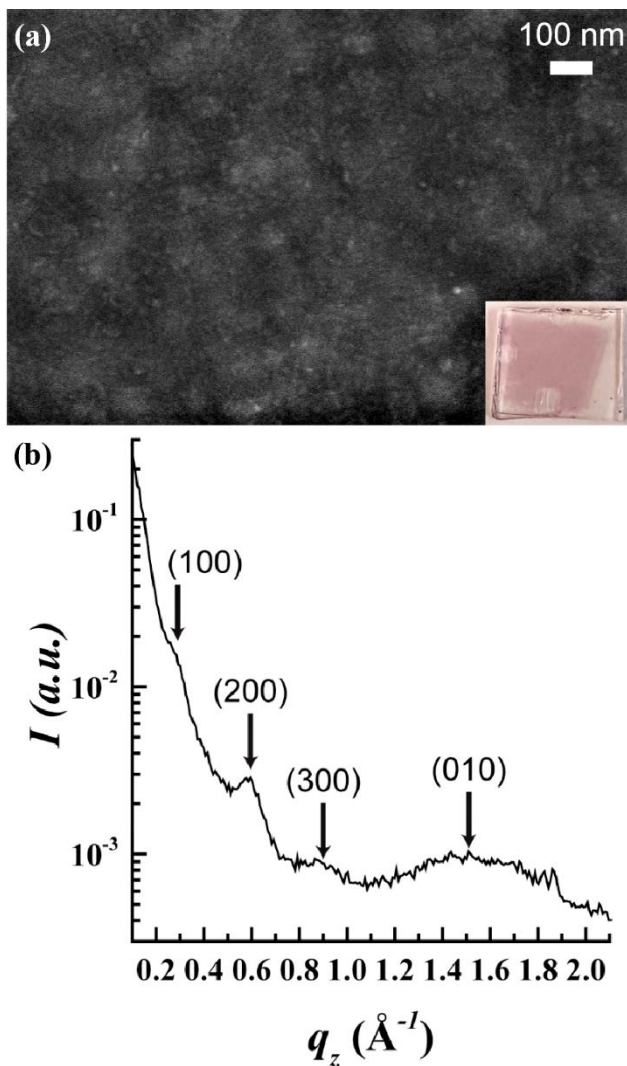


Figure 46: SEM image of PBTTT crystallized from graphene on ITO (a) in a 0.05 mg/mL metastable solution of ODCB for 24 h. GIWAXS out-of-plane cut of PBTTT crystallized from graphene on Si (b). The inset in (a) shows the film selectively crystallized on graphene.

### 3.5 Conclusions

The hysteresis in the crystallization of P3HT increases with molecular weight and plateaus upon reaching the chain folding threshold ( $M_n = 12$  kg/mol), as confirmed by TEM and UV-vis spectroscopy. No correlation was observed between the hysteresis window and the regioregularity of the polymer. With the increase in the amount of crystalline P3HT, the reduction in the Avrami exponent, and the faster crystallization kinetics observed upon addition of graphene it was demonstrated that graphene serves as a good nucleating agent for one-dimensional

crystallization of P3HT. AFM results point to a formation of Form I P3HT crystals on HOPG. The NFs crystallize from a wetting layer capable of reorganizing into crystals with a face-on orientation. Moreover, PBTTT was shown to selectively crystallized on graphene. AFM shows that PBTTT is less interdigitated ( $26.4 \pm 0.3 \text{ \AA}$ ) in the domains organized on HOPG than when crystallized in the bulk ( $21.5 \text{ \AA}$ ). Given that it was not possible to clearly identify regularly arranged chains in the PBTTT crystals, the larger interchain distance seen by AFM can be attributed to a metastable phase that can rearrange into more stable crystals.

## CHAPTER 4

# SELECTIVE CRYSTALLIZATION OF P3HT NANOFIBERS FOR GRAPHENE-BASED ELECTRONICS

### 4.1 Abstract

Molecular templated growth of polymers is a promising route to high-performance organic electronic materials through precise patterning of the components during device fabrication. Using supersaturated solutions of poly(3-hexyl thiophene) (P3HT) in *m*-xylene, conditions were found to deliver fast and selective crystallization of nanofibers (NFs) from graphene surfaces. Electrode patterns printed by liquid-bridge mediated nanotransfer using a solution process based on graphene ink can induce crystallization of P3HT NFs. The rapid and selective crystallization of NFs connected graphene electrodes 10  $\mu\text{m}$  apart in 5 min as verified by a functional organic field effect transistors and microscopy techniques. Further crystallization increased the hole mobilities up to  $\mu = 20 \times 10^{-3} \text{ cm}^2 \text{ V}^{-1} \text{ s}^{-1}$ , which is two orders of magnitude higher than comparable devices fabricated by spin casting of P3HT films on otherwise identical electrodes ( $\mu = 0.9 \times 10^{-3} \text{ cm}^2 \text{ V}^{-1} \text{ s}^{-1}$ ). Additionally, graphene was used in heterojunction solar cells as a buffer layer between ITO and PEDOT: PSS. Remarkably, devices fabricated by spin casting P3HT with methanofullerene phenyl-C61-butyric-acid-methyl-ester (PCBM) showed a higher power conversion efficiency (1.92%) than it was previously reported (0.68%). However, devices prepared by selectively crystallizing P3HT from graphene short circuited possibly due to preexisting holes in the graphene films. The solution-processable fabrication of electrodes and semiconductors is potentially scalable and amenable to roll-to-roll manufacturing.

### 4.2 Introduction

A key challenge for the fabrication of organic electronic devices is the precise control over the location of each feature to minimize inter-device interference and manufacturing

steps.<sup>118,119</sup> Molecular templated growth (MTG) is a promising method to orient and control the morphology of organic semiconductors to produce high quality thin films and improve the performance of solar cells and .<sup>120</sup> Graphene has spark increasing interest as electrode and template due to its extraordinary optical transparency, conductivity and mechanical strength.<sup>85,121,122</sup> Previously, MTG for organic electronics has been mostly focused on small molecules<sup>120,123</sup> due to their ability to form single crystals with good charge transport characteristics. For example Cho and coworkers demonstrated that vacuum using graphene as template for pentacene increases the power conversion efficiency of solar cells.<sup>121</sup> Yet, this method required vacuum deposition of the active layer, which increases the fabrication costs and does not allow for in situ characterization. If the thin films are formed from solutions of small organic molecules it is challenging to identify suitable orthogonal solvents in subsequent fabrications steps.<sup>124</sup> Polymers represent an attractive alternative because they possess excellent solution rheology properties to generate solution-based processing techniques over large surfaces.<sup>125</sup>

Another aspect to consider in the fabrication of organic electronics is the hierarchical assembly/orientation of the structures in the active layer.<sup>126</sup> Poly(3-hexyl thiophene) (P3HT) a major pillar in the development of polymer-based electronics assembles into nanofibers (NFs) due to the strong  $\pi$ - $\pi$  interactions between chains.<sup>127</sup> The  $\pi$ - $\pi$  stacking of the chains allows for high charge transport along the nanofiber direction.<sup>126,128,129</sup> Also, it has been demonstrated that P3HT selectively crystallizes from graphene into NFs.<sup>83</sup> The  $\pi$ - $\pi$  interactions drive P3HT to adopt a face-on orientation when in contact with graphene<sup>56</sup> and highly oriented pyrolytic graphite (HOPG) as characterized by scanning tunneling microscopy (STM).<sup>71,86</sup> Interestingly, the face-on orientation induced by graphene doubles the out-of-plane charge mobility of P3HT films.<sup>85</sup> On the other hand, orienting P3HT edge-on can increase the in-plane charge motility by an order of magnitude.<sup>20</sup> Therefore, it is desirable to exercise hierarchical assembly of 1D structures with the

proper orientation with respect to the substrate (e.g. edge-on for transistors and face-on for solar cells). NFs oriented in-plane have been shown to have edge-on oriented chains.<sup>130</sup> Interestingly, P3HT NFs are oriented in-plane when crystallized from graphene and removed from the solvent.<sup>83</sup>

Generally, electrodes for organic electronics including graphene are fabricated using vacuum deposition, thus increasing the cost and complicating device fabrication.<sup>131</sup> It has been demonstrated that graphene can be deposited using solution phase processing while maintaining high conductivity.<sup>132</sup> This was achieved using ethyl cellulose to disperse the flakes and post-deposition annealing to reduce the film resistivity. This process has achieved a resolution of the device features of 5  $\mu\text{m}$  using screen printing.<sup>133</sup> Subsequent patterning steps though, require precise alignment of the device features and patterning organic semiconductors remains a challenge due to the high sensitivity of these materials to the harsh lithography conditions (i.e. exposure to UV light, etchants and heat). To overcome this challenge, Wang et al<sup>122</sup> have shown that selective crystallization of semiconducting molecules is a suitable approach for patterning electronic devices, and improve charge transport in the out-of-plane direction. In their method, phenyl/phenyl capped tetraaniline (TANI) were patterned in  $\sim 2$  h through a crystallization-driven assembly into micron-sized crystals, using graphene as a template. Yet, faster crystallization routes are desired to meet roll-to-roll fabrication (i.e. ultimate processing technique for mass fabrication) translational speeds (over 1 m/min).<sup>134</sup> To address this, our work takes advantage of the intermolecular interaction between P3HT and graphene to pattern NFs on graphene-based electrodes, and to simultaneously fabricate multiple OFETs within 5 – 15 min with higher in-plane mobility than spin casted equivalents.

## **4.3 Experimental procedure**

### **4.3.1 Materials**

Highly regioregularity (95 %) poly(3-hexylthiophene) (P3HT) and m-xylene were purchased from Rieke Metals and Alfa-Aesar, respectively, and used as received. If not specified the rest of the materials were obtained from Sigma Aldrich. The molecular weight of the polymer was characterized using gel permeation chromatography (GPC) in polystyrene standards. Highly oriented pyrolytic graphite (HPG) ZYB Quality was purchased from K-Tek Nanotechnology. The HOPG substrates were freshly exfoliated before each used.

### **4.3.2 Film thickness growth**

The crystallization kinetics of P3HT on HOPG was studied using a Cypher ES atomic force microscopy (AFM) from Asylum Research. After peeling the off top layer of the HOPG substrate with an adhesive tape a fresh surface was exposed. To partially cover the HOPG surface, a series of circular sacrificial layers of poly(acrylic acid) (PAA) were drop casted on the top of the HOPG surface. This was achieved using a concentrated (50 mg/mL) solution in methanol. Once the film was dried at ambient conditions for at least 3 h, the HOPG substrates were immersed in the metastable solutions at different concentrations. Upon removing the substrates from solution and rinsing with fresh m-xylene the dried substrates were immersed in methanol to remove the PAA sacrificial layer. The thickness was then calculated from the step height difference between the HOPG bare surface and the P3HT film. For each AFM image 3 thickness profiles at least 1  $\mu\text{m}$  long were averaged over a 375 nm width individually.

### **4.3.3 Graphene electrodes fabrication**

The electrodes were fabricated using graphene ink imprinted on Si wafers with a thermally grown 300 nm  $\text{SiO}_2$  layer (Si-Tech, Inc). Before imprinting the electrodes, the silicon

wafers were cleaned under 5 min of ultrasonication in a 50 %v/v Versa-Clean™ aqueous solution, filtered water, acetone and isopropanol. After drying under a gentle flow of nitrogen, the substrates were exposed to UV-ozone for 10 min.

Graphene ink was prepared using liquid-bridge mediated nanotransfer molding. For soft nanoimprint lithography, an SU8 master was developed in a cleanroom environment with electrode patterns. Polydimethylsiloxane (PDMS) (Sylgard 184) was mixed in a 1:10 elastomer to base ratio, poured over the SU8 master, and heated at 65 °C overnight until cured.

The graphene ink was prepared using graphene flakes capped with ethyl cellulose and dispersed in an isopropanol (IPA), N-Methyl-2-pyrrolidone (NMP), and ethanol solvent mixture. The ink was drop casted at corner of a PDMS stamp and dragged across the surface of the patterned stamp, until the ink discontinuously de-wets from the surface, but filled the electrode patterns. The stamp filled with ink was dried for 10 min at 55 °C to remove residual solvent within the stamp.

To print, a drop of ethanol was cast on the cleaned Si/SiO<sub>2</sub> wafer, and the stamp with dried graphene ink was placed over the ethanol. The ethanol serves as a liquid bridge that causes the dried ink to print directly onto the Si/SiO<sub>2</sub> wafer. The PDMS stamp can be removed, leaving behind cleanly imprinted graphene electrodes. The graphene ink is annealed at 250 °C for 30 min until conductive.

The printed graphene electrodes are in the shape of two opposite “L” patterns that are roughly 250 nm in height, 300 μm in width and 165 μm in length, with a surface roughness of 38 ± 2 nm as seen by AFM (Figure 47). The channel length between two electrodes is 10 μm.

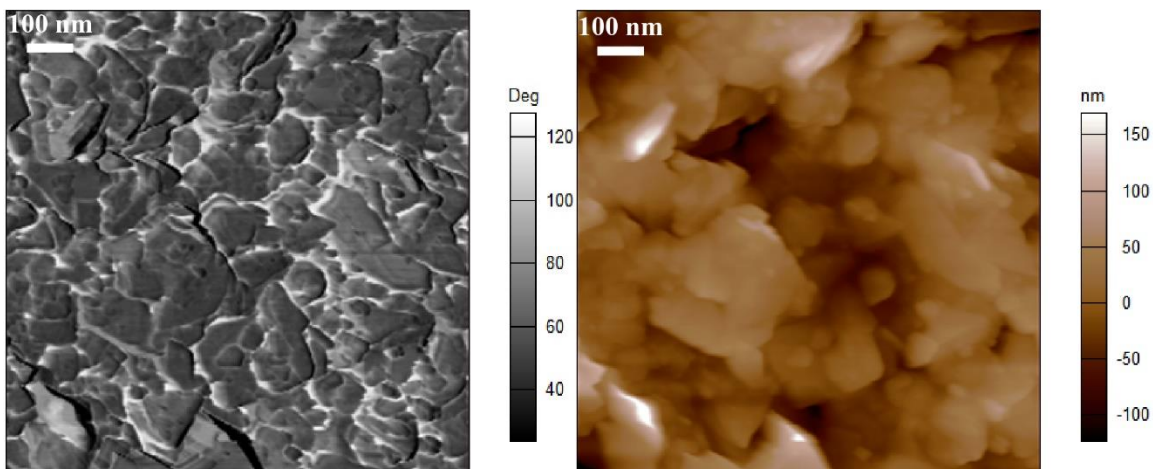


Figure 47: AFM of graphene electrodes.

#### 4.3.4 Graphene fabrication

Graphene was fabricated through chemical vapor deposition (CVD). Methane was introduced (930 sccm) with hydrogen (330 sccm) into a quartz tube as reactor to catalyzed the formation of graphene on the surface of 3 Cu foils (2 cm × 3 cm) at 1,000 °C. Upon reaction for 13 min, the system was cooled down by exposing the reactor to room temperature. At 400 °C the methane was turn off while keeping the hydrogen flow until the temperature reach 200 °C. The graphene was transfer to the desired substrate using conventional poly(methyl methacrylate) (PMMA) wet transfer as explained below.

First, the graphene on one side of the foil was protected with a thick layer of PMMA (Mw = 350 kg/mol) purchased from Sigma Aldrich. This film was fabricated by spin casting (60 s at 2 krpm) a solution (0.5 g/mL) of the polymer in chlorobenzene. Baking the samples in an oven at 120 °C for 20 min removed solvent residues and annealed the PMMA. Subsequently, the foils were exposed to oxygen plasma to oxidize the unprotected side of graphene. The Cu was etched overnight in an aqueous solution of ammonium persulfate (20 mg/mL). Residual ions were removed by transferring the samples in a water bath for 30 min using a glass slide. The samples were transfered to the pre-cleaned substrates and dried overnight at 120 °C. The PMMA was



removed by incubating the samples in acetone bath for 1 h. A final annealing at 350 °C under H<sub>2</sub> flow (330 sccm) for 1 h was performed to remove PMMA residues.

#### 4.3.5 Transistor characterization

The P3HT NF devices were characterized using a bottom-gate bottom-contact (BG-BC) transistor configuration as seen in Figure 48. BG-BC devices were made from Si/SiO<sub>2</sub> substrates with graphene ink source/drain electrodes directly imprinted onto the substrate. The characterization was carried out using a Keithley 4200-SCS in direct and reverse bias conditions.

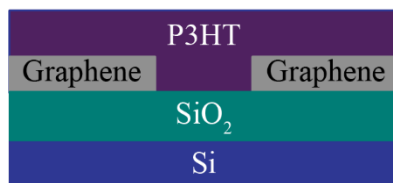


Figure 48: Schematic illustrating the cross-section of a transistor with a bottom-gate bottom-contact architecture used in this study.

#### 4.3.6 Selective crystallization

For patterning P3HT on the graphene electrodes, it is important that the crystallization is selective to graphene and that the crystallization in the bulk of the solution is negligible. To confirm this, bare silicon wafers were exposed to the metastable solutions (2 mg/mL) for from 5 min to 15 min. As evident in Figure 53 did not show any changes in the apparent number of nanofibers on its surface, in contrast to the abundant NFs on the graphene electrodes. This is evidence that P3HT crystallizes selectively on graphene. On the other hand, nucleation of NFs is observed on the graphene electrodes using *in situ* AFM (Figure 49).

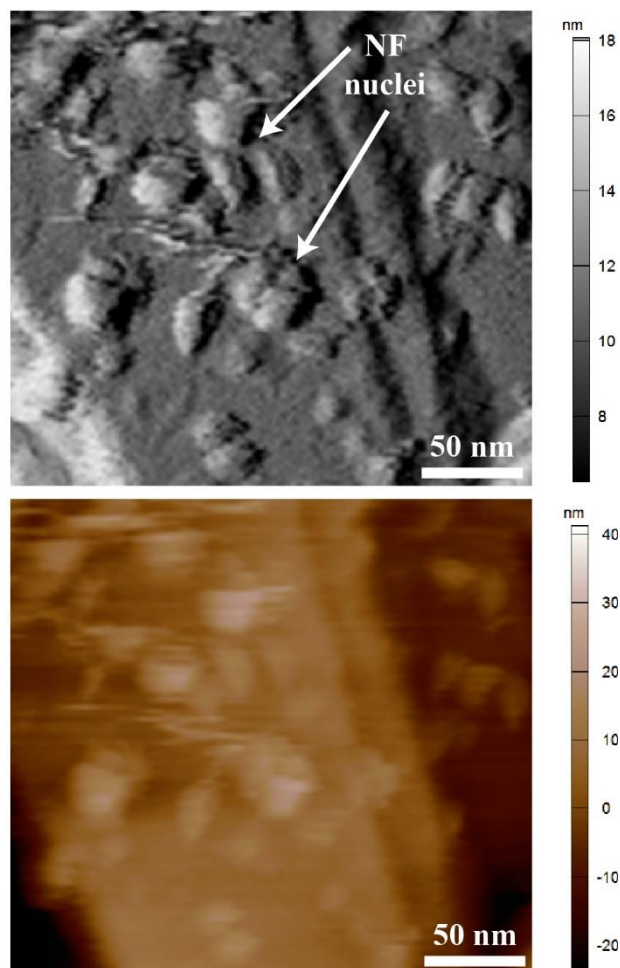


Figure 49: P3HT crystallizing on graphene electrodes as characterized by AFM in situ and visualized using the amplitude channel (top) and the height channel (bottom).

## 4.4 Results and discussion

### 4.4.1 Selective crystallization of P3HT for field effect transistors

Using the thermochroic properties of P3HT in solution and UV-vis spectroscopy, it was determined that P3HT shows a wide hysteresis between the crystallization ( $T_c$ ) and melting temperatures ( $T_m$ ) in solutions.<sup>47,83</sup> We previously demonstrated that P3HT solutions can have a sizable driving force for crystallization and exist in a metastable state with no spontaneous nucleation due to a nucleation barrier.<sup>83</sup> Subsequent addition of graphene-coated substrates induces selective crystallization on the graphene surface. Although graphene is a good nucleating

agent, the chosen crystallization conditions resulted in lethargic film formation kinetics, which required 5 days to generate a 90 nm thick film of P3HT. Therefore, to obtain faster crystallization on the surface of graphene for speeding up device fabrication, we increased the P3HT molecular weight and concentration. The kinetics of P3HT film formation was studied on HOPG substrates incubated at room temperature (22 °C) in a 20 mL vial containing ~1 mL of the metastable solution for the desired crystallization period. Afterwards, the substrates were cleaned with fresh solvent. Prior P3HT crystallization a poly(acrylic acid) PAA sacrificial layer was drop casted on the HOPG to produce a height step between the P3HT film and the HOPG. After removing the PAA layer with methanol, atomic force microscopy (AFM) was used to determine the P3HT film thickness. As shown in Figure 50a higher molecular weight P3HT ( $M_n = 22$  kg/mol) achieves a film thickness of approximately 90 nm on HOPG in a time 3 orders of magnitude shorter than for relatively low molecular weight ( $M_n = 12$  kg/mol) from our previous studies.<sup>83</sup> This is due to the stronger crystallization driving force at higher molecular weight. As determined from UV-vis spectroscopy the  $T_c$  increases with molecular weight from  $T_c = 6 \pm 1$  °C ( $M_n = 12$  kg/mol) to  $T_c = 22 \pm 1$  °C ( $M_n = 22$  kg/mol), when the solutions are cool from 80 °C at 1 °C/min. Similarly, the crystallization rate systematically increases with concentration. At 15 min a thickness of  $83 \pm 4$  nm was achieved with a concentration of 2 mg/mL, while it required 30 min for the 1 mg/mL solution to reach a similar value ( $82 \pm 6$  nm). Not surprisingly, at 1 h the 0.5 mg/mL solution formed a film  $54 \pm 1$  nm, thus it was demonstrated that the 2 mg/mL concentration was optimal for selective and rapid formation of P3HT films. Higher concentrations than 2 mg/mL were not explored because the crystallization point of a 2 mg/mL solution is around room temperature ( $22 \pm 1$  °C). Therefore, further increments in concentration would induce nucleation in the bulk of the solution and the selective crystallization will be obscured by absorbed crystals on the substrate surface, as seen previously with pre-formed NFs in solution.<sup>130</sup>

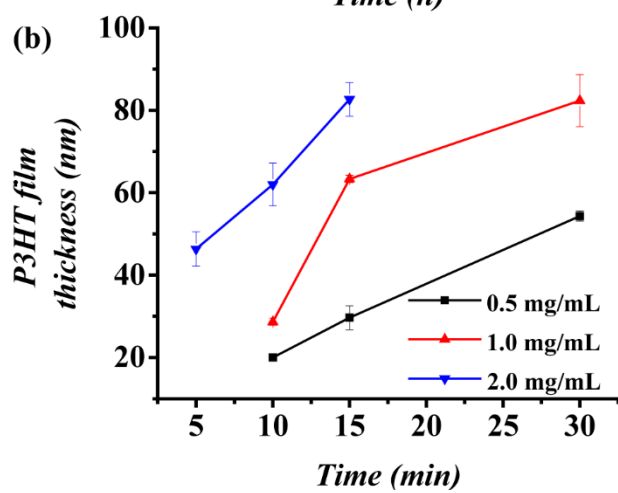
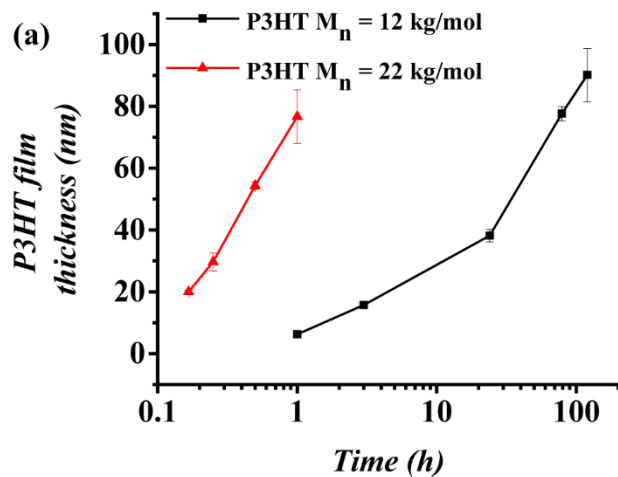


Figure 50: Kinetics of P3HT crystallized on HOPG into films from solution at low molecular ( $M_n = 12$  kg/mol) weight and high molecular weight ( $M_n = 22$  kg/mol) (a). The effects of concentration on high molecular weight P3HT crystallized from HOPG (b). The reported thickness and standard error values were measured by AFM. Although suitable for studying the kinetics of crystallization of P3HT, HOPG is too bulky and difficult to pattern to be useful in electronic devices. One layer of HOPG (e.g. graphene) possesses high conductivity and flexibility to be used as an electrode.<sup>121</sup> Typically, graphene is fabricated through chemical vapor deposition on Cu substrates. The combination of high temperatures, high vacuum, low throughput and complicated transferring process into substrates renders graphene into an expensive material to be used as an electrode.<sup>131,135</sup> Liam and Hersam developed a potential solution to this challenge by suspending graphene flakes in organic solvents using ethyl-cellulose as dispersant.<sup>132</sup> This colloidal graphene can be printed into conductive patterns to be used as electrodes. For our experiments, we used printed graphene electrodes fabricated through soft lithography from this graphene/cellulose ink, as developed by Naik et al. Once printed the graphene films became conducting by annealing at 250 °C for 30 min. The electrodes have a channel width of 10  $\mu\text{m}$  and a length of 300  $\mu\text{m}$  suitable for OFETs.

The crystallization of P3HT on the graphene electrode surface was monitored *in situ* using AFM (Figure 51 and Figure 49). At 198 min of exposure to a 0.5 mg/mL P3HT solution the surface of graphene showed several features that can be identified as NF nuclei (Figure 51a). As seen in Figure 49 both amplitude and height channels show the same features, which discards the possibility that these features are created from an artifact during imaging. The low contrast observed in the images seen using the height channel is due to the relatively rough surface of the graphene electrodes ( $R_q = 38 \pm 2$  nm). From the AFM amplitude channel in Figure 51 it is possible to observe NF nucleating on the surface of the graphene electrodes within 2 min as indicated by the red rectangle. Evidently the crystallization on graphene electrodes is like the crystallization mechanism observed on HOPG (Figure 17).

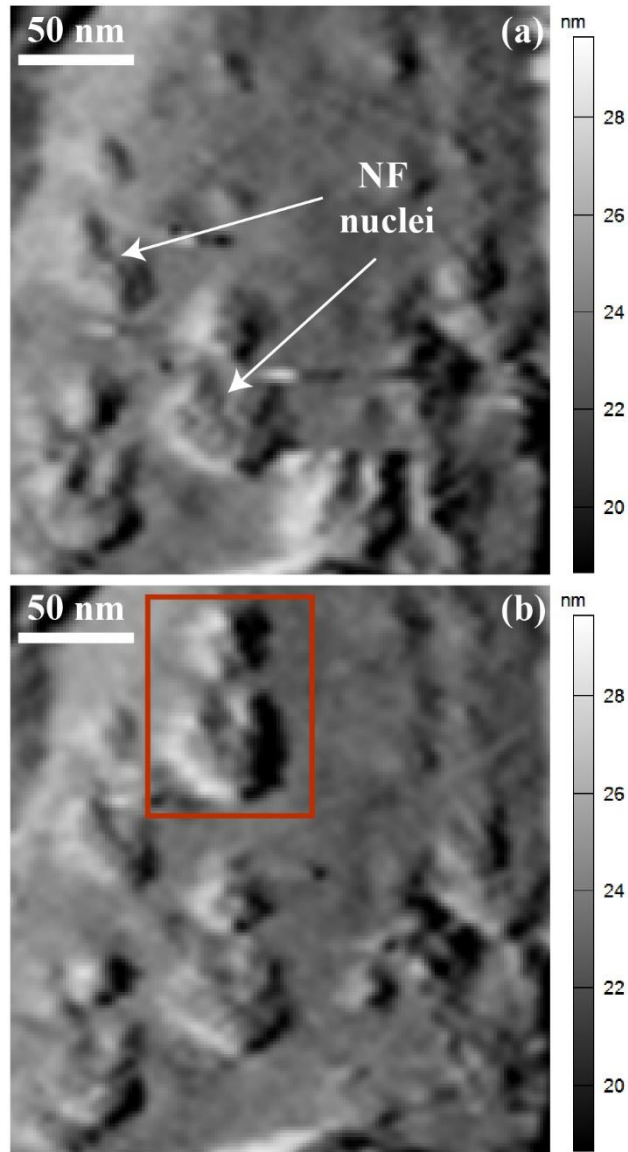


Figure 51: *In situ* AFM showing the formation of nuclei of P3HT NFs on the surface of graphene electrodes at 198 min (a) and 200 min (b) during the exposure to the P3HT metastable solution. Using the optimized conditions for fast crystallization of P3HT NFs from HOPG, the graphene electrodes were exposed to a P3HT metastable solution (2 mg/mL) for: 5 min, 10 min, 15 min at room temperature. Additionally, to ensure pre-crystallization in solution is insignificant, a control experiment was carried in parallel with clean SiO<sub>2</sub> substrates. Optical microscopy (Figure 52) shows that there is minimal or no change in the color of the SiO<sub>2</sub> substrates (pink surfaces), indicating the deposition of P3HT (blue domains) on the SiO<sub>2</sub> substrates exposed from 5 min until 15 min is negligible. This observation was also qualitatively confirmed using AFM as the number density of NFs on the surface SiO<sub>2</sub> did not appear to significantly change (Figure 53). Interestingly, the amount of P3HT crystallized on the graphene electrodes is evident at the early stages of crystallization as evidenced by the blue regions at 5 min of crystallization. However, most of the channel is not connected as seen by the bare SiO<sub>2</sub> (pink) portions of the sample. Subsequently, at 10 min P3HT crystallizes and partially connects the electrodes. Within 15 min, the channel gap between electrodes is completely covered by P3HT NFs, demonstrating the rapid crystallization of P3HT on graphene.

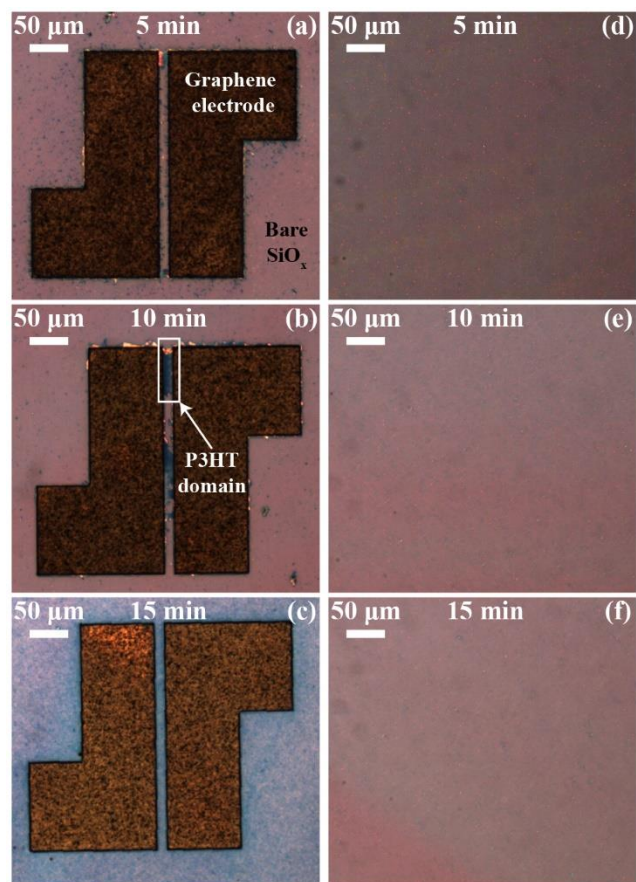


Figure 52: Imprinted graphene electrodes on SiO<sub>2</sub> wafers incubated in metastable (2 mg/mL) P3HT solutions for 5 min (a), 10 min (b) and 15 min (c), with their respective bare silicon wafers (d-f) exposed to the same conditions.



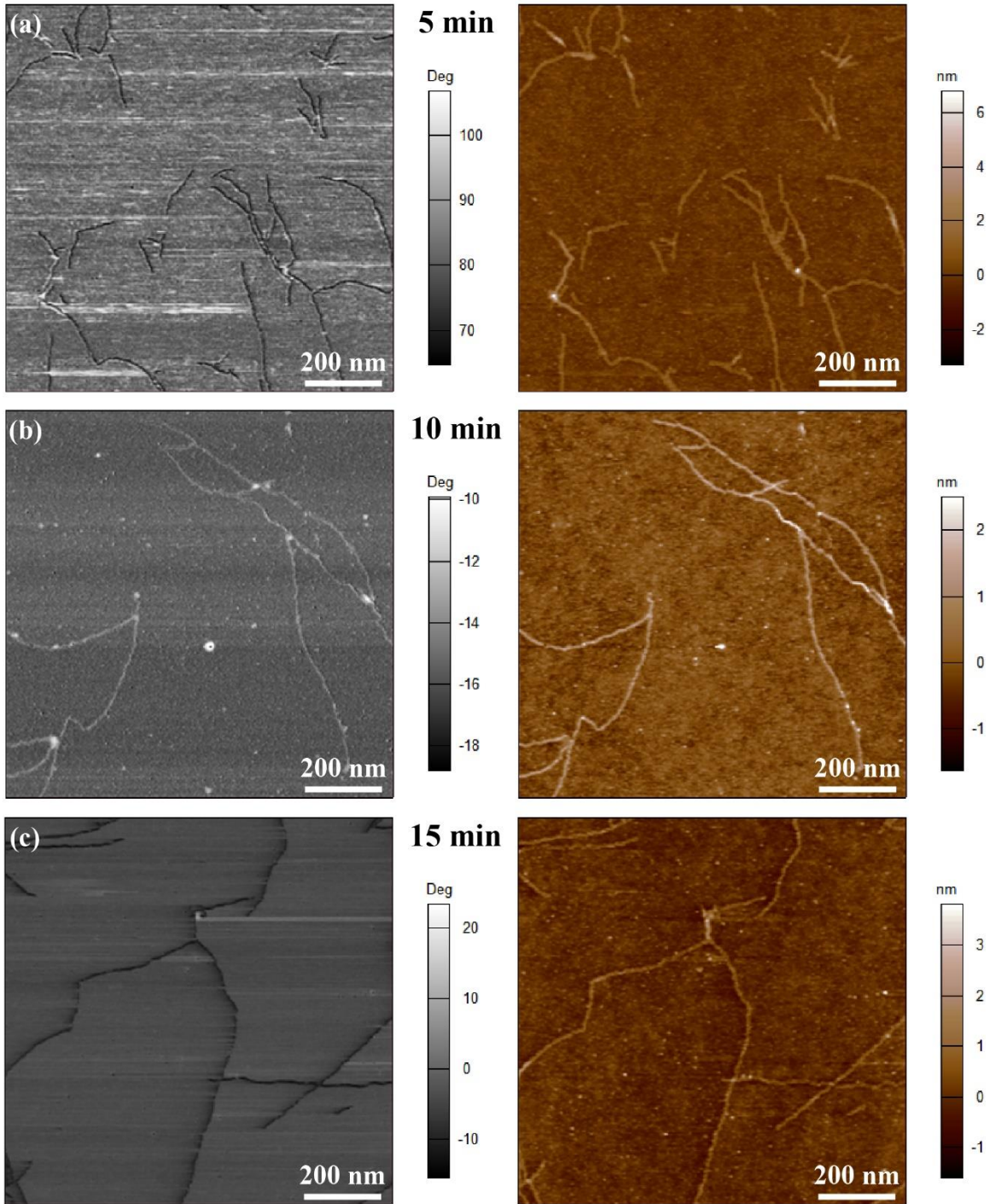


Figure 53: AFM of bare SiO<sub>2</sub> substrates exposed to metastable P3HT solutions (2 mg/mL) for 5 min (a), 10 min and (b) 15 min (c).

SEM shows that P3HT crystallizes into NFs oriented in-plane on the surface of the graphene electrodes (Figure 54). We have previously observed that P3HT NFs adopted primarily edge-on orientation when grown from graphene surfaces, since capillary forces are sufficient to

flatten the flexible and high aspect-ratio fibers upon drying of solvent.<sup>83</sup> Thus, the film is mostly composed of edge-on orientated P3HT chains. The graphene flakes with an average lateral dimension of 300 nm are visible as seen previously,<sup>132</sup> while the dense film of P3HT is composed of NFs  $17.4 \pm 0.3$  nm in width. Due to the high number density of NFs on the graphene surface it is not possible to determine the length of the NFs by SEM. However, it is evident that the P3HT NF film extends away from the electrodes into the channel as seen in Figure 52 and Figure 54. SEM also demonstrates that much of the channel is not covered by NFs for the spin casted sample because the darker regions identified as P3HT, leave abundant brighter regions, assigned to the wafer surface (Figure 55).

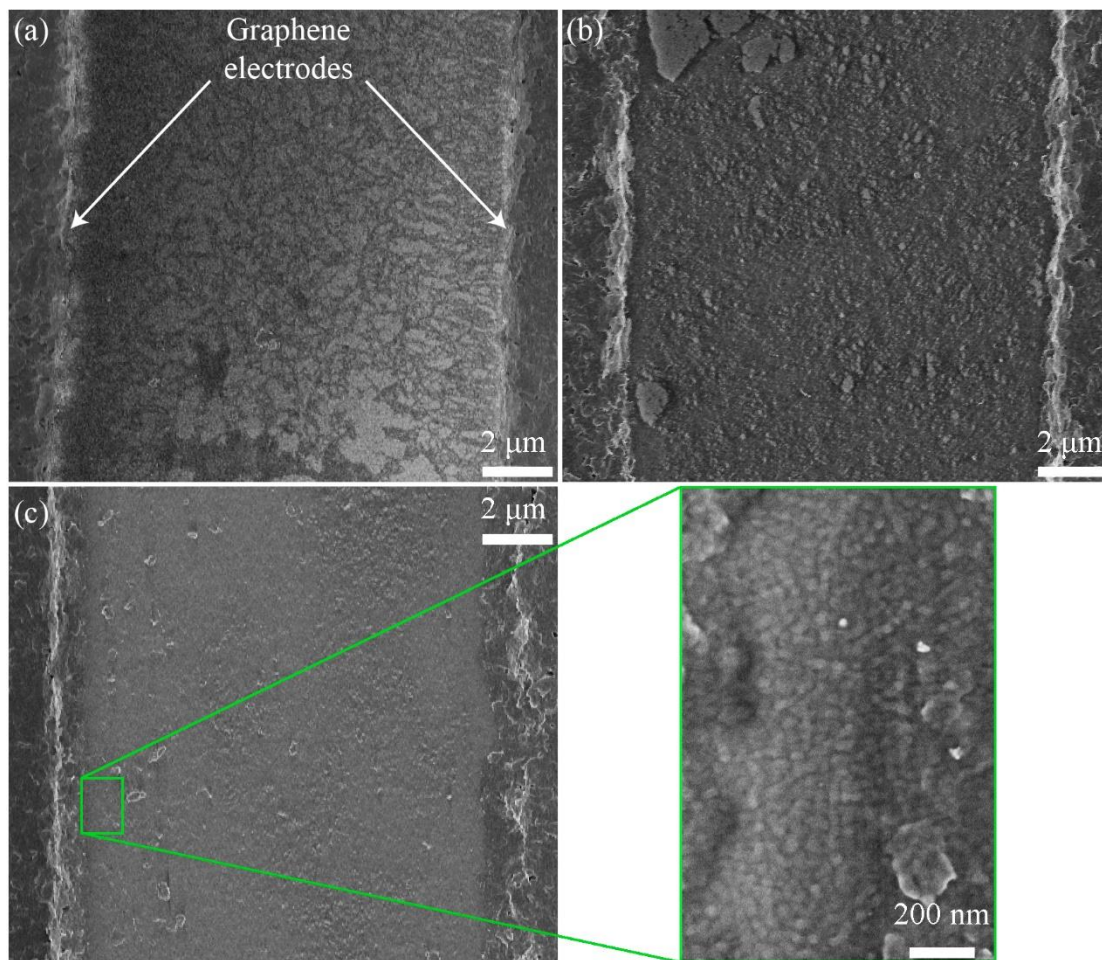


Figure 54: SEM showing the P3HT morphology on graphene electrodes when crystallized for 5 min (a), 10 min (b), 15 min (c). The NF morphology is shown from the area depicted by the green rectangle on the right of (c).

Interestingly, the electrodes incubated for 5 min, show a comparable NF film to the spin casted sample. The NF network spans from the graphene electrode into the channel as the crystallization proceeds. Although there are still gaps in the network, the NF crystallization helps creating a uniform film shown for both the 10 min and the 15 min samples. Despite an appreciable crystallization in the bulk of the solution (the solution turns from bright orange to light brown) at 15 min, most of the crystallization still occurs on the graphene electrodes.

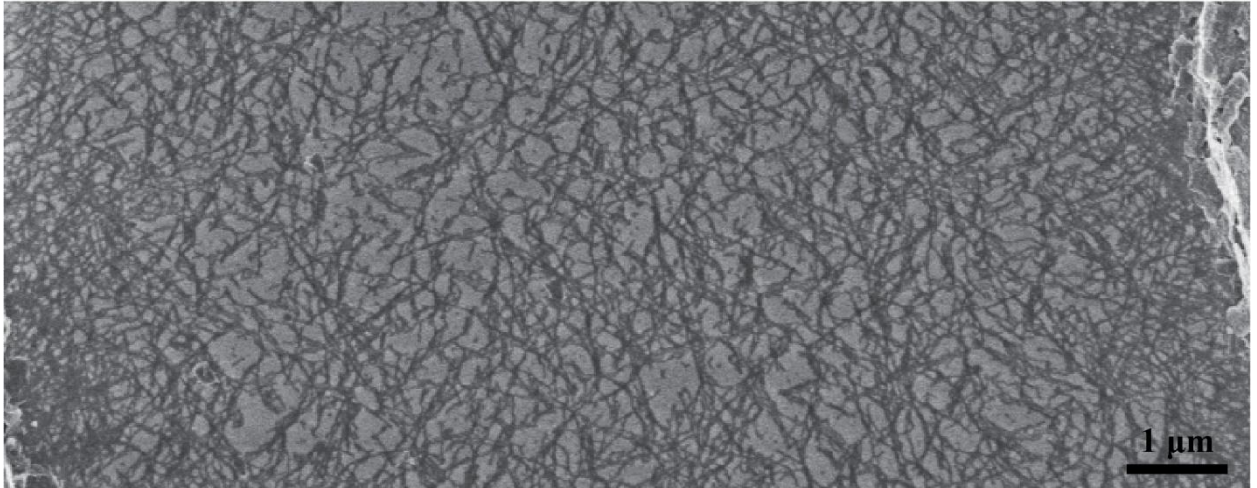


Figure 55: SEM showing the P3HT morphology in the channel of a set of graphene electrodes as spin casted from a *m*-xylene (2 mg/mL) solution.

To characterize the crystallization kinetics, the film thickness of P3HT crystallized from the graphene electrodes ( $t_{gr}$ ), was measured by optical profilometry (Figure 56). The P3HT film thickness is 5-fold smaller than for the films crystallized on HOPG ( $t_{HOPG}$ ). A similar difference was observed in our previous work,<sup>83</sup> and presumably reflects the more efficient nucleation of P3HT nanofibers on HOPG compared to graphene.



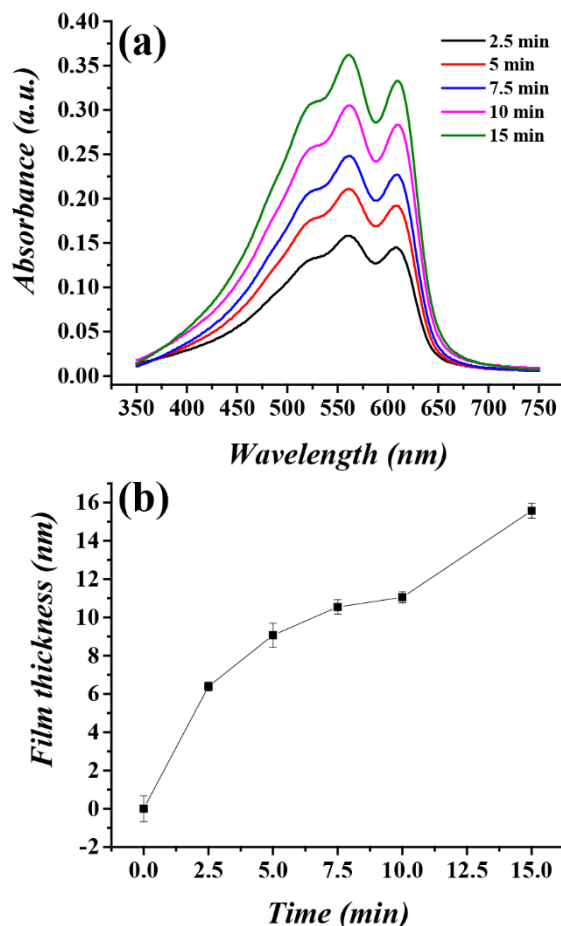


Figure 56: Formation kinetics of P3HT NFs crystallized from graphene flakes spin casted on glass (a) as characterized by UV-vis spectroscopy. Film thickness of P3HT as characterized by optical profilometry (b).

The contribution of the crystallization time to the film's electronic properties was determined using OFETs with a bottom-gate bottom-contact (BG-BC) configuration. The architecture of the device is illustrated in cross-section in Figure 48. A control sample was fabricated by spin casting the metastable solution (after passing the solution through a 0.45  $\mu\text{m}$  Teflon syringe filter), which will be considered as 0 min crystallization. The measurements were carried out under ambient conditions.

Transfer curves for the devices were obtained by sweeping the gate voltage ( $V_G$ ), while monitoring the drain current ( $I_{DS}$ ). Figure 57 depicts the transfer characteristic of devices measured at different crystallization times with their typical hole transport in  $p$ -channel

semiconductor under negative gate voltages. The hole mobilities were calculated using the slope of  $\sqrt{I_D}$  versus  $V_G$  line in the saturation regime, resulting in a maximum mobility ( $\mu$ ) obtained for the devices with the longest crystallization time of  $\mu = 20 \times 10^{-3} \text{ cm}^2 \text{ V}^{-1} \text{ s}^{-1}$  with a threshold voltage ( $V_{th}$ ) of 3 V and an on/off ratio of  $10^5$ . In contrast, the control sample yielded a value of  $\mu = 0.9 \times 10^{-3} \text{ cm}^2 \text{ V}^{-1} \text{ s}^{-1}$ , comparable to literature reports for devices prepared by spin coated P3HT ( $\mu = 1 \times 10^{-3} \text{ cm}^2 \text{ V}^{-1} \text{ s}^{-1}$ ) from dichlorobenzene.<sup>136</sup> Remarkably, the mobility increases with crystallization time as summarized in Table 6. Guo and coworkers<sup>130</sup> prepared devices by adsorbing a monolayer of preformed NFs in chloroform ( $\mu = 9.1 \times 10^{-3} \text{ cm}^2 \text{ V}^{-1} \text{ s}^{-1}$ ). Although the preparation of the active layer for this former study is significantly shorter (1 min) than for our devices with similar mobilities (10 min), the formation of the NFs takes a week and does not provide selective patterning of the active layer. As seen from the optical microscopy and SEM images, increments in the crystallization time allows for a higher number of NFs connecting the electrodes, thus the mobility improves.

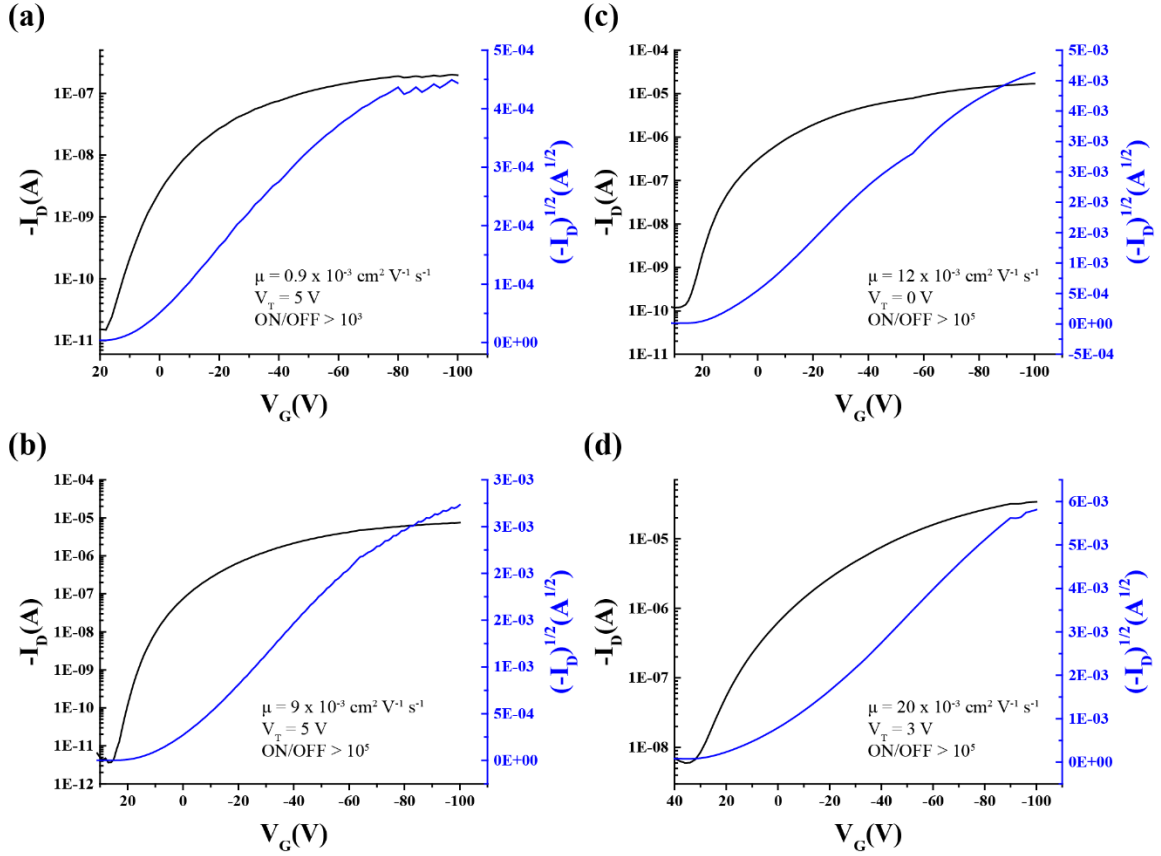


Figure 57: Transfer characteristics of OFET of P3HT spin casted (a), and crystallized for different crystallization periods: 5 min (b), 10 min (c), 15 min (d) on graphene electrodes. A  $V_{DS} = -100 \text{ V}$  was applied to all devices with a bottom-gate and bottom-contact geometry on a  $\text{SiO}_2/\text{Si}$  wafer.

Table 6. OFET properties as a function of crystallization time. The values represent an average of ten devices.

Crystallization time (min)	Mobility ( $\times 10^{-3} \text{ cm}^2 \text{ V}^{-1} \text{ s}^{-1}$ )	Threshold voltage (V)	ON/OFF ratio
0 (spin casted)	$0.9 \pm 0.1$	$5 \pm 4$	$> 10^3$
5	$9 \pm 5$	$5 \pm 7$	$> 10^5$
10	$12 \pm 4$	$0 \pm 10$	$> 10^5$
15	$20 \pm 3$	$3 \pm 4$	$> 10^5$

The output characteristics were obtained for gate voltages from 40 V to -100 V in increments of -10 V and a drain voltage from 0 to -100 V. Figure 57 shows the output characteristics corresponding to the increasing crystallization time. Despite the non-negligible hysteresis in the OFETs as shown in Figure 59, the trend of increasing mobility is evident. This

hysteresis can be mainly attributed to oxygen doping coming from air and traps in the P3HT films. The reduction in the hysteresis with crystallization time can be explained by a reduction in the active layer openings as the P3HT network fills the OFET channel.

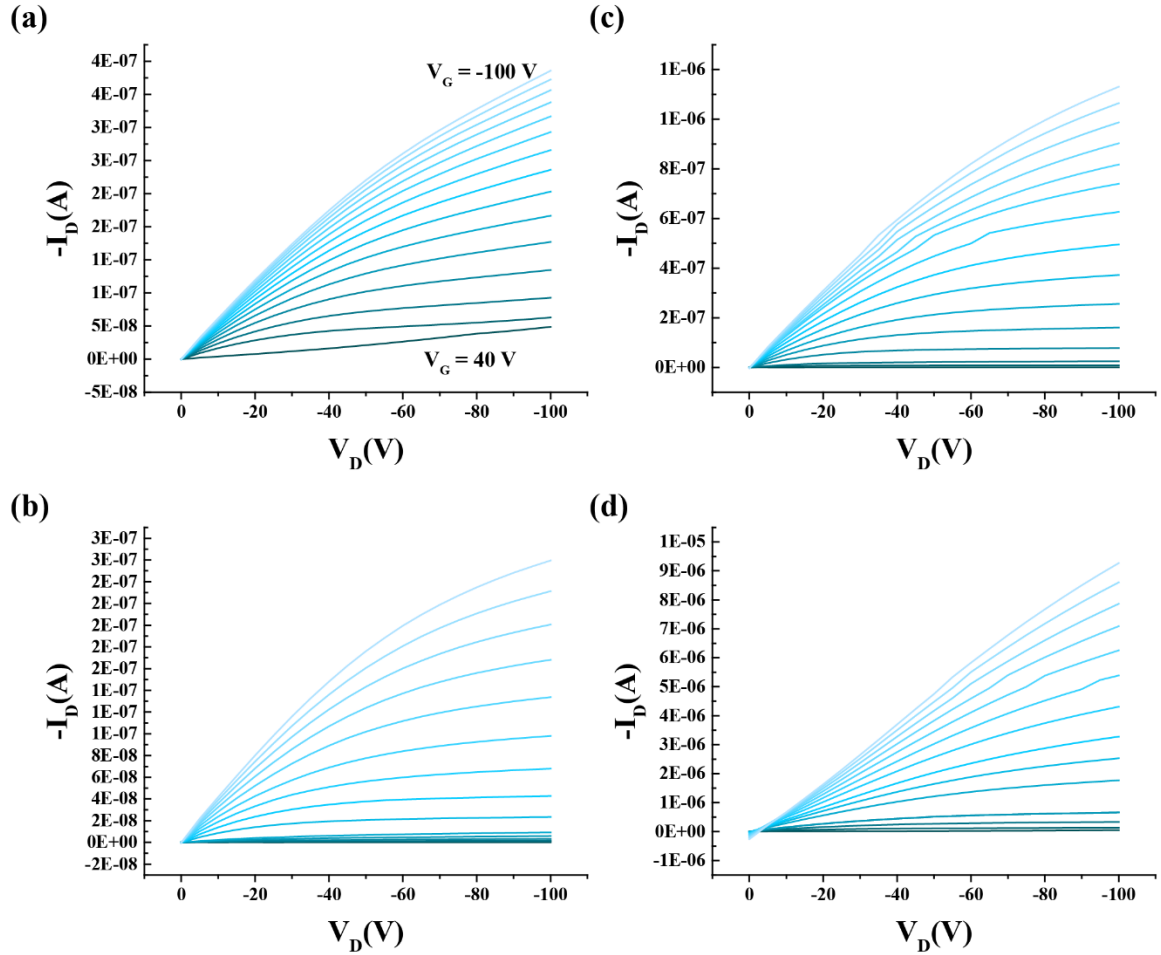


Figure 58: OFET output characteristics of P3HT spin casted (a) and crystallized for different times in a supersaturated solution for 5 min (b), 10 min (c) and 15 min (d) on graphene electrodes. The gate voltage was varied from 40 V to -100 V in 10 V steps.



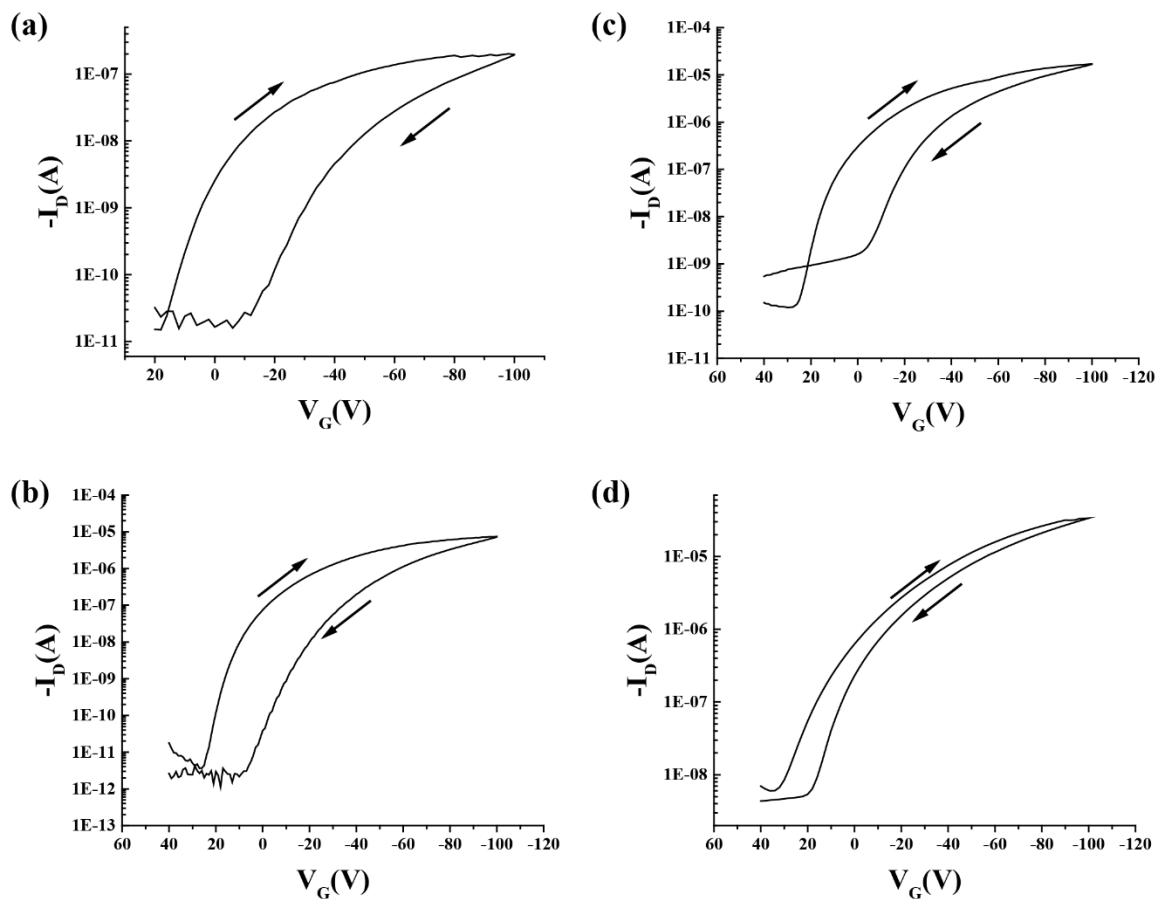


Figure 59: Hysteresis behavior in the devices prepared from P3HT spin casted (a) and P3HT crystallized for different times in a supersaturated solution for 5 min (a), 10 min (b) and 15 min (c) on graphene electrodes. A  $V_{DS} = -100$  V was applied to all devices with a bottom-gate and bottom-contact geometry on a  $\text{SiO}_2/\text{Si}$  wafer.

### 4.3.2 Graphene as an electrode for photovoltaic cells

Graphene can function in a solar cell as hole transport layer (HTL)<sup>121</sup> or electron acceptor.<sup>84</sup> However, the main limiting factor for employing graphene as a HTL is its low WF (4.5 eV). The maximum power conversion efficiency (PCE) obtained for P3HT-based devices employing pristine graphene as anode is 0.68%.<sup>137</sup> Alternatively, Wang and coworkers<sup>138</sup> argued that the conductivity of monolayer graphene is too low (6 k  $\Omega$ ), thus by incorporating a multiple layers of graphene the conductivity was increased to a value similar to ITO (10–20  $\Omega$  sq<sup>-1</sup>). Unfortunately, the 4-layer-graphene film is hydrophobic, which causes the buffer film composed of PEDOT:PSS (poly(3,4-ethylenedioxythiophene):polystyrene sulfonate) to be non-uniform.

This results in low PCE of 0.12% and 0.35% for pristine graphene with and without PEDOT:PSS buffer films, respectively. Consistently, both studies agreed that the main limiting factor for increasing the PCE of these devices is the deep HOMO of P3HT  $\sim 5.0$  eV, which does not match graphene's WF.

It has been demonstrated that the highest occupied molecular orbital (HOMO) of P3HT changes with crystallization, since  $\pi$  stacking allows for easier extraction of electrons compared to the amorphous counterpart.<sup>113</sup> Crystalline P3HT has a higher HOMO of 4.6 eV compared to amorphous P3HT (HOMO = 4.9 eV). Our results demonstrate that the HOMO of P3HT films decreases from 5.1 to 4.8 within 72 h of crystallization, which yields a final film thickness of  $\sim 20$  nm. Therefore, it is hypothesized that thicker P3HT crystallized from graphene can better match graphene's WF.

To fabricate photovoltaic devices, indium tin oxide (ITO) substrates were cleaned in successive sonication steps in 20 % Mucosal® aqueous solution, distilled water, acetone and isopropanol for 5 min each. The substrates were dried by blowing nitrogen. Finally, the substrates were exposed to UV-ozone for 10 min. Graphene was transferred using conventional PMMA transfer as described in Section 4.3.4. A thin film  $\sim 10$  nm thick of PEDOT:PSS (poly(3,4-ethylenedioxythiophene):polystyrene sulfonate) was spin casted at 3,500 rpm for 90 s on the ITO substrates and baked at 150 °C for 30 min in air. Solar cells were finished in a glove-box under nitrogen atmosphere using an active layer of P3HT ( $M_n = 28$  kg/mol as measured by GPC in polystyrene equivalent,  $D = 1.9$ ) and methanofullerene phenyl-C61-butyric-acid-methyl-ester (PCBM), obtained from Sigma Aldrich. A 20 mg/mL solution of 1:1<sub>w/w</sub> PCBM:P3HT was prepared by heating the solid mixture in *o*-dichlorobenzene to 80 °C with gentle stirring. After cooling to room temperature, the solution was filtered through a 0.2  $\mu\text{m}$  poly(tetrafluoroethylene) membrane syringe filter. The solution was spin casted at 1000 rpm. The devices were finalized

with the vacuum deposition of the cathode composed of Ca 15 min and 100 nm of Al as described in Figure 60. The samples were annealed at 110 °C for 10 min under N<sub>2</sub> atmosphere.

Current–voltage (I–V) characteristics were measured in a N<sub>2</sub> atmosphere using a Keithley 2400 source-meter under simulated AM1.5G irradiation using a 300 W Xe lamp solar simulator (Newport 91160). The illuminated area (0.06 cm<sup>2</sup>) was defined by the aperture from the metal photomask used in all reported PCE measurements. The parameters of 9 photovoltaic devices were averaged and tabulated in Table 7. Surprisingly, the power conversion efficiency is higher than was previously reported (0.68%).<sup>137</sup> This can be attributed to PMMA residues that were not removed in previous studies. Here, an annealing step at 350 °C under hydrogen for 1 h was carried to remove any PMMA residues, according to Cho and coworkers.<sup>135</sup> However, crystallizing P3HT for 2 h (~50 nm) into NFs directly from graphene resulted in short circuited devices as shown in Figure 61. It is possible that the graphene has holes on its surface, thus the high selectivity of P3HT to crystallize from graphene leaves openings for the anode to connect the cathode and short circuit the device.

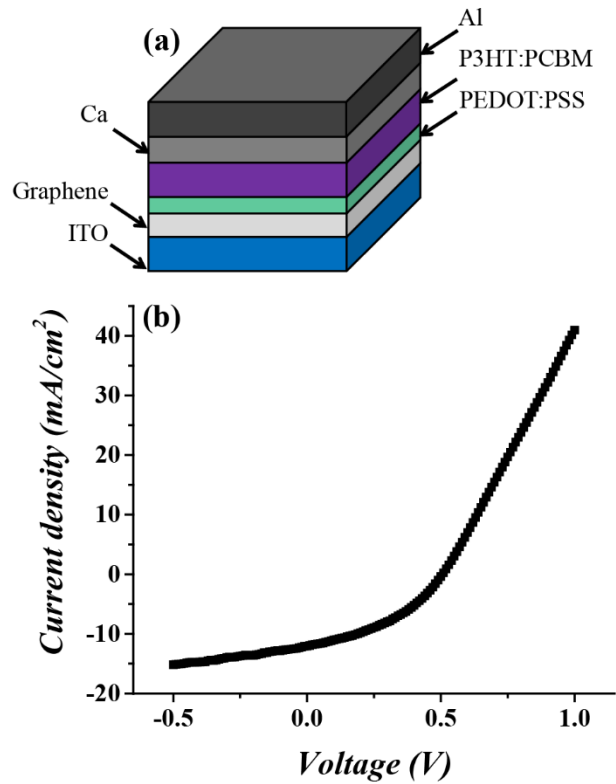


Figure 60: Schematic illustrating a typical OPV cell using a graphene based anode with a P3HT:PCBM (1:1) mixture as active layer (a) with its respective I-V curve (b). Table 7: Averaged open circuit voltage ( $V_{oc}$ ), short circuit current ( $I_{sc}$ ), fill factor and power conversion efficiency (PCE) of 9 photovoltaic devices.

$V_{oc}$ (mV)	$I_{sc}$ ( $\text{mA}/\text{cm}^2$ )	Fill factor	PCE (%)
$489 \pm 7$	$10.8 \pm 0.3$	$37 \pm 2$	$1.9 \pm 0.2$

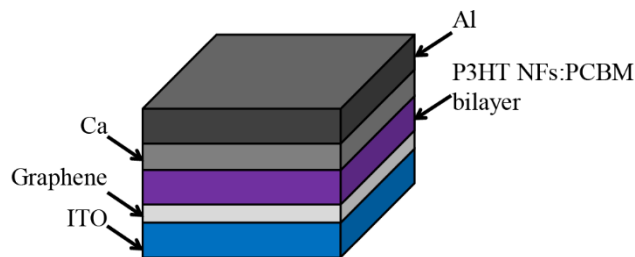


Figure 61: Schematic illustrating the architecture of an OPV cell based on a bilayer active film that uses graphene as a hole extraction layer to template for P3HT NFs.

#### 4.4 Conclusions

It was found that the fastest selective crystallization of NFs from graphene was achieved using P3HT of relatively high molecular weight ( $M_n = 22 \text{ kg/mol}$ ) and increasing the

crystallization point of the solution to be around room temperature at a concentration of 2 mg/mL. P3HT was crystallized into NFs from graphene-based electrodes in a similar way as from HOPG. It was found that P3HT NFs grow sufficiently long to connect adjacent graphene electrodes. The mobility of OFETs increases with crystallization time up to 2 orders of magnitude higher than spin casted P3HT. Moreover, OPV devices with an efficiency of 1.9% were fabricated using MLG graphene as buffer layer in the anode. The increment in PCE can be possibly explained by the removal of PMMA residues on graphene with annealing.

## SUMMARY AND OUTLOOK

### 5.1 Crystallization of P3HT nanofibers from graphene surfaces

A method for selective crystallization of P3HT NFs from graphene surfaces in solution was demonstrated. The rate of crystal nucleation is found to be highly dependent on the underlying substrate. Microscopy measurements confirmed that the NFs grow out-of-plane in solution growth but collapse into an in-plane orientation upon solvent removal, due presumably to capillary forces. Moreover, through seeded crystallization of P3HT short NFs can be extended. However, but this process is hindered by aggregation and adsorption onto the container's wall during crystallization. P3HT-P3TEGT was shown to produce more uniform seeds and promises to mitigate the mentioned issues with pristine P3HT.

Motivated by a previous study that observed the influence of polarizability on the adsorption of small molecules onto graphene surfaces,<sup>68</sup> it will be interesting to modify the polarizability of the graphene coated substrates using self-assembled monolayers (SAMs). Since  $\pi$ - $\pi$  and van der Waals interactions between P3HT and graphene have been seen to play an important role in the P3HT configuration,<sup>56</sup> a systematic study with a variety of SAMs is proposed to determine the importance of the van der Waals interactions. Using selective crystallization of P3HT on graphene substrates modified with SAMs will provide guidance on what are the most important intermolecular interactions to obtain fast crystallization with the precise orientation, without interference of preformed structures adsorbing in solution. We hypothesize that the stronger van der Waals interactions, due to the higher polarizability of the substrate, will yield a faster crystallization of P3HT on graphene. The length of the SAM will increase the polarizability of the surface. Therefore, going from silanized surface with hexyl to a tetradecyl chains will promote nucleation as the length of the alkyl chain increases. Similarly,

fluorinated chains with the same length will yield an increment in the nucleation kinetics. In a recent study the work function of gold (111) was demonstrated to not change significantly when increasing the chain length of hydrogenated aliphatic SAMs.<sup>139</sup> The same conclusion is valid for fluorinated aliphatic SAMs with an even number of fluorinated carbons. Therefore, it will be possible to decouple the effects of van der Waals interactions from changes in charge transfer due to modifications from different work functions of graphene, since accordingly to a previous study<sup>140</sup> the work function of the substrate increases with the addition of a perfluoroalkyl SAM.

Results suggest that the crystallization and orientation effects of graphene on P3HT is due to the strong  $\pi$ - $\pi$  interactions, thus this method should be reproducible to others conjugated polymers. Using P3HT as a proof of concept, it will be exciting to extend this investigation to the following higher performance materials, commercially available and crystalline: poly[2,5-bis(3-tetradecylthiophen-2-yl)thieno[3,2-b]thiophene] (PBTTT) and poly[(5,6-difluoro-2,1,3-benzothiadiazol-4,7-diyl)-alt-(3,3''-di(2-octyldodecyl)-2,2';5',2'';5'',2'''-quaterthiophen-5,5'''-diyl)] (PffBT4T-2OD).

It is also important to show that conjugated polymers can be processed in aqueous solutions or greener solvents.<sup>141</sup> Therefore, to provide crystallization conditions with more polar solvents than *m*-xylene, metastable solutions of P3HT-P3TEGT can be generated in a mixture of chlorobenzene and methanol. These metastable solutions will be employed to extend pre-formed seed and crystallize NFs on graphene. Finally, high resolution imaging of the P3TEGT-P3HT chains crystallizing on HOPG can elucidate the chain conformation on the crystals, through a systematic study of the ratio of the P3HT-P3TEGT blocks.

## 5.2 Formation mechanism of P3HT nanofibers crystallized from graphene

The hysteresis in the crystallization of P3HT increases with molecular weight and plateaus possibly due to the larger interfacial energy required to generate bigger nuclei. With the

increment in the amount crystalline P3HT, the reduction in the Avrami exponent and the faster crystallization kinetics upon addition of graphene it was demonstrated that graphene serves as a good nucleating agent for one-dimensional crystallization of P3HT. *In situ* AFM results point to a formation of Form I P3HT crystals on HOPG. The NFs crystallize from a wetting layer capable of reorganizing into crystals with a face-on orientation. P3HT films crystallized from graphene MoO<sub>3</sub> are initially composed of face-on oriented structures but transition into edge-on as the film grows thicker. It was shown that the face-on conformation is partially preserved by embedding the P3HT structures in an ICBA matrix. Moreover, PBTTT was shown to selectively crystallize on graphene. And AFM suggests that PBTTT is less interdigitated ( $26.4 \pm 0.3 \text{ \AA}$ ) in the domains organized on HOPG than when crystallized in the bulk ( $21.5 \text{ \AA}$ ), which can be attributed to a metastable phase.

Despite that it is evident that the P3HT crystals are Form I, it will be of great addition to perform coarse grain simulations on this system. Through calculations of the lowest energy configuration of P3HT with respect of the crystallographic axes of HOPG, the epitaxial crystallization could be confirmed. Moreover, a systematic study of electron diffraction on the (100) reflection of P3HT crystallized from graphene flakes at different incident angles can provide further confirmation of epitaxial relation between the two materials. To illustrate the generalizability of this crystallization, this study could be repeated for highly crystalline polymers such PBTTT and poly[(5,6-difluoro-2,1,3-benzothiadiazol-4,7-diyl)-alt-(3,3''-di(2-octyldodecyl)-2,2';5',2'';5'',2'''-quaterthiophen-5,5'''-diyl)] (PffBT4T-2OD).

### 5.3 Selective crystallization of P3HT nanofibers for graphene-based electronics

It was found that P3HT crystallizes into NFs from graphene-based electrodes in a similar way as from HOPG. P3HT NFs grow sufficiently long ( $\sim 1 \text{ \mu m}$ ) to connect adjacent graphene electrodes. The mobility of OFETs increases with crystallization time up to 2 orders of magnitude



higher than spin casted P3HT. Moreover, MLG graphene was integrated in the anode of OPV cell yielding a PCE = 1.9%.

To demonstrate the advantages of selective crystallization of NFs from graphene, future work can focus on fabricating flexible and transparent electronic devices. Given the mechanical strength of graphene-based electrodes, flexible transistors can be fabricated through selective crystallization of P3HT. Using an azide containing P3HT, it will be possible to generate mechanical and chemical resistant flexible platform for building complex circuits and/or sensors. Moreover, as shown previously other polymers such as PBTTT are suitable for selective crystallization of NFs on graphene electrodes, suggesting the generality of the method and route to deliver more efficient OFETs. The 10 nm spin casted graphene films have transmittance of 69% at 550 nm, thus it is possible to generate highly transparent electrodes by minimizing the thickness of graphene electrodes while maintaining film homogeneity.

The influence of the underlying substrate on the P3HT crystallization from graphene is of great interest as it can impact the performance of organic electronics. More specifically, the work function of the substrate can be optimized as an anode for OPV cells. Typically, developments in OPV devices choose substrates only for their ease of processing and work function (WF). Graphene can function in a OPV cell as hole transport layer (HTL)<sup>121</sup> or active material.<sup>84</sup> Therefore, increasing the amount of oxygen moieties (“oxidation level”) in graphene will lower the injection barrier of holes from the polymer to the anode, due to the higher WF of graphene oxide<sup>142</sup>. Lock and coworkers<sup>143</sup> have shown the ability of NEXAFS to detect the bonding types and functionality occurring on low Z-elements, thus it is possible to determine the oxidation level in graphene.

From a previous study,<sup>112</sup> it is expected that having the  $\pi$  electrons exposed to the surface creates a higher electrostatic potential in a face-on orientation compared to the edge-on orientation. Consequently, a face-on orientation will yield a higher HOMO (increasing ionization

potential) than an edge-on orientation. The main limiting factor for employing graphene as a HEL is its low work function (4.5 eV). Therefore, the oxidation level of graphene will lower the injection barrier of holes from the polymer to the anode, due to the higher work function of reduced graphene oxide. Although UV-ozone will generate defects (*e.g.*, vacancies, cracks and oxidized groups) on graphene and reduce polymer face-on orientation and crystallinity, we hypothesize that the impact will be dominated by an increment in hole transport due to the low barrier energy between graphene and the polymer. This work will permit polymer-based active layers to be deposited with morphological control, impacting the design rules for organic electronic devices.

## BIBLIOGRAPHY

- (1) Jacobson, M. Z.; Delucchi, M. A. *Energy Policy* **2011**, *39* (3), 1154–1169.
- (2) Green, M. A.; Emery, K.; Hishikawa, Y.; Warta, W.; Dunlop, E. D. *Prog. Photovoltaics Res. Appl.* **2014**, *22* (7), 701–710.
- (3) SAS Output [https://www.eia.gov/electricity/annual/html/epa\\_08\\_04.html](https://www.eia.gov/electricity/annual/html/epa_08_04.html) (accessed Apr 5, 2017).
- (4) Shockley, W.; Queisser, H. J. *J. Appl. Phys.* **1961**, *32* (3), 510.
- (5) Krebs, F. C.; Tromholt, T.; Jørgensen, M. *Nanoscale* **2010**, *2* (6), 873–886.
- (6) Park, H. J.; Kang, M.-G.; Ahn, S. H.; Guo, L. J. *Adv. Mater.* **2010**, *22* (35), E247-53.
- (7) Oh, J. Y.; Shin, M.; Lee, T. II; Jang, W. S.; Lee, Y.-J.; Kim, C. S.; Kang, J.-W.; Myoung, J.-M.; Baik, H. K.; Jeong, U. *Macromolecules* **2013**, *46* (9), 3534–3543.
- (8) Huang, Y.; Kramer, E. J.; Heeger, A. J.; Bazan, G. C. *Chem. Rev.* **2014**, *114* (14), 7006–7043.
- (9) Green, M. A.; Emery, K.; Hishikawa, Y.; Warta, W.; Dunlop, E. D. **2013**, No. version 41, 1–11.
- (10) Diao, Y.; Shaw, L.; Bao, Z.; Mannsfeld, S. C. B. *Energy Environ. Sci.* **2014**, *7* (7), 2145–2159.
- (11) Green, M. A.; Emery, K.; Hishikawa, Y.; Warta, W.; Dunlop, E. D.; Levi, D. H.; Ho-Baillie, A. W. Y. *Prog. Photovoltaics Res. Appl.* **2017**, *25* (1), 3–13.
- (12) Slota, J. E.; He, X.; Huck, W. T. S. *Nano Today* **2010**, *5* (3), 231–242.
- (13) Wang, M.; Wudl, F. *J. Mater. Chem.* **2012**, *22* (46), 24297–24314.
- (14) Yu, J.; Zheng, Y.; Huang, J. *Polymers (Basel)*. **2014**, *6* (9), 2473–2509.
- (15) Moore, G. E. *IEEE Solid-State Circuits Newsl.* **2006**, *20* (3), 33–35.
- (16) Sariciftci, N. S.; Heeger, A. J. Conjugated polymer - acceptor heterojunctions; diodes, photodiodes, and photovoltaic cells. US5331183 A, July 19, 1994.
- (17) Duong, D. T.; Ho, V.; Shang, Z.; Mollinger, S.; Mannsfeld, S. C. B.; Dacuña, J.; Toney, M. F.; Segalman, R.; Salleo, A. *Adv. Funct. Mater.* **2014**, *24* (18), 4515–4521.
- (18) Kim, J.-H.; Kim, M.; Jinnai, H.; Shin, T. J.; Kim, H.; Park, J. H.; Jo, S. B.; Cho, K. *ACS Appl. Mater. Interfaces* **2014**, *6* (8), 5640–5650.
- (19) García, G.; Timón, V.; Hernández-Laguna, A.; Navarro, A.; Fernández-Gómez, M. *Phys. Chem. Chem. Phys.* **2011**, *13* (21), 10091–10099.
- (20) Sirringhaus, H.; Brown, P. J.; Friend, R. H.; Nielsen, M. M.; Bechgaard, K.; Langeveld-Voss, B. M. W.; Spiering, A. J. H.; Janssen, R. A. J.; Meijer, E. W.; Herwig, P.; de

- Leeuw, D. M. *Nature* **1999**, *401* (6754), 685–688.
- (21) Clarke, T. M.; Durrant, J. R. *Chem. Rev.* **2010**, *110* (11), 6736–6767.
- (22) Facchetti, A. *Chem. Mater.* **2011**, *23* (3), 733–758.
- (23) Brédas, J.-L.; Cornil, J.; Heeger, A. J. *Adv. Mater.* **1996**, *8* (5), 447–452.
- (24) Yao, Y.; Dong, H.; Hu, W. *Polym. Chem.* **2013**, *4* (20), 5197–5205.
- (25) Skrypnychuk, V.; Boulanger, N.; Yu, V.; Hilke, M.; Mannsfeld, S. C. B.; Toney, M. F.; Barbero, D. R. *Adv. Funct. Mater.* **2014**, 664–670.
- (26) Zhang, Y.; Diao, Y.; Lee, H.; Mirabito, T. J.; Johnson, R. W.; Puodziukynaite, E.; John, J.; Carter, K. R.; Emrick, T.; Mannsfeld, S. C. B.; Briseno, A. L. *Nano Lett.* **2014**, *14* (10), 5547–5554.
- (27) Wang, C.; Jimison, L. H.; Goris, L.; McCulloch, I.; Heeney, M.; Ziegler, A.; Salleo, A. *Adv. Mater.* **2010**, *22* (6), 697–701.
- (28) McCulloch, I.; Heeney, M.; Bailey, C.; Genevicius, K.; Macdonald, I.; Shkunov, M.; Sparrowe, D.; Tierney, S.; Wagner, R.; Zhang, W.; Chabinyc, M. L.; Kline, R. J.; McGehee, M. D.; Toney, M. F. *Nat. Mater.* **2006**, *5* (4), 328–333.
- (29) Willot, P.; Steverlynck, J.; Moerman, D.; Leclère, P.; Lazzaroni, R.; Koeckelberghs, G. *Polym. Chem.* **2013**, *4* (9), 2662.
- (30) Brinkmann, M. *J. Polym. Sci. Part B Polym. Phys.* **2011**, *49* (17), 1218–1233.
- (31) Lee, Y. J.; Kim, S. H.; Yang, H.; Jang, M.; Hwang, S. S.; Lee, H. S.; Baek, K.-Y. *J. Phys. Chem. C* **2011**, *115* (10), 4228–4234.
- (32) Kim, H. J.; Paek, K.; Yang, H.; Cho, C.-H.; Kim, J.-S.; Lee, W.; Kim, B. J. *Macromolecules* **2013**, *46* (21), 8472–8478.
- (33) Lee, I.-H.; Amaladass, P.; Yoon, K.-Y.; Shin, S.; Kim, Y.-J.; Kim, I.; Lee, E.; Choi, T.-L. *J. Am. Chem. Soc.* **2013**, No. 1, 2–5.
- (34) Verilhac, J.-M.; LeBlevenec, G.; Djurado, D.; Rieutord, F.; Chouiki, M.; Travers, J.-P.; Pron, A. *Synth. Met.* **2006**, *156* (11–13), 815–823.
- (35) Yang, X.; Uddin, A. *Renew. Sustain. Energy Rev.* **2014**, *30*, 324–336.
- (36) Kozub, D. R.; Vakhshouri, K.; Orme, L. M.; Wang, C.; Hexemer, A.; Gomez, E. D. *Macromolecules* **2011**, *44* (14), 5722–5726.
- (37) Verploegen, E.; Mondal, R.; Bettinger, C. J.; Sok, S.; Toney, M. F.; Bao, Z. *Adv. Funct. Mater.* **2010**, *20* (20), 3519–3529.
- (38) Yang, H. In *Organic Field-Effect Transistors*; Optical Science and Engineering; CRC Press, 2007; pp 371–401.
- (39) Zhang, R.; Li, B.; Iovu, M. C.; Jeffries-EL, M.; Sauv e, G.; Cooper, J.; Jia, S.; Tristram-

- Nagle, S.; Smilgies, D. M.; Lambeth, D. N.; McCullough, R. D.; Kowalewski, T. *J. Am. Chem. Soc.* **2006**, *128* (11), 3480–3481.
- (40) Nagarjuna, G.; Venkataraman, D. *J. Polym. Sci. Part B Polym. Phys.* **2012**, *50* (15), 1045–1056.
- (41) Wang, S.; Kiersnowski, A.; Pisula, W.; Müllen, K. *J. Am. Chem. Soc.* **2012**, *134* (9), 4015–4018.
- (42) Lee, M. J.; Gupta, D.; Zhao, N.; Heeney, M.; McCulloch, I.; Siringhaus, H. *Adv. Funct. Mater.* **2011**, *21* (5), 932–940.
- (43) Biniek, L.; Pouget, S.; Djurado, D.; Gonthier, E.; Tremel, K.; Kayunkid, N.; Zaborova, E.; Crespo-Monteiro, N.; Boyron, O.; Leclerc, N.; Ludwigs, S.; Brinkmann, M. *Macromolecules* **2014**, *47* (12), 3871–3879.
- (44) Hartmann, L.; Tremel, K.; Uttiya, S.; Crossland, E.; Ludwigs, S.; Kayunkid, N.; Vergnat, C.; Brinkmann, M. *Adv. Funct. Mater.* **2011**, *21* (21), 4047–4057.
- (45) Kim, J. S.; Lee, J. H.; Park, J. H.; Shim, C.; Sim, M.; Cho, K. *Adv. Funct. Mater.* **2011**, *21* (3), 480–486.
- (46) Liu, J.; Arif, M.; Zou, J.; Khondaker, S. I.; Zhai, L. *Macromolecules* **2009**, *42* (24), 9390–9393.
- (47) Oh, J. Y.; Shin, M.; Lee, T. Il; Jang, W. S.; Min, Y.; Myoung, J.; Baik, H. K.; Jeong, U. *Macromolecules* **2012**, *45* (18), 7504–7513.
- (48) Rahimi, K.; Botiz, I.; Stingelin, N.; Kayunkid, N.; Sommer, M.; Koch, F. P. V.; Nguyen, H.; Coulembier, O.; Dubois, P.; Brinkmann, M.; Reiter, G. *Angew. Chem. Int. Ed. Engl.* **2012**, *51* (44), 11131–11135.
- (49) Gwyther, J.; Gilroy, J. B.; Rupar, P. A.; Lunn, D. J.; Kynaston, E.; Patra, S. K.; Whittell, G. R.; Winnik, M. A.; Manners, I. *Chemistry* **2013**, *19* (28), 9186–9197.
- (50) Patra, S. K.; Ahmed, R.; Whittell, G. R.; Lunn, D. J.; Dunphy, E. L.; Winnik, M. A.; Manners, I. *J. Am. Chem. Soc.* **2011**, *133* (23), 8842–8845.
- (51) Qian, J.; Li, X.; Lunn, D. J.; Gwyther, J.; Hudson, Z. M.; Kynaston, E.; Rupar, P. A.; Winnik, M. A.; Manners, I. *J. Am. Chem. Soc.* **2014**, *136* (11), 4121–4124.
- (52) Qian, J.; Lu, Y.; Chia, A.; Zhang, M.; Rupar, P. A.; Gunari, N.; Walker, G. C.; Cambridge, G.; He, F.; Guerin, G.; Manners, I.; Winnik, M. A. *ACS Nano* **2013**, *7* (5), 3754–3766.
- (53) Niles, E. T.; Roehling, J. D.; Yamagata, H.; Wise, A. J.; Spano, F. C.; Moulé, A. J.; Grey, J. K. *J. Phys. Chem. Lett.* **2012**, *3* (2), 259–263.
- (54) Chunder, A.; Liu, J.; Zhai, L. *Macromol. Rapid Commun.* **2010**, *31* (4), 380–384.
- (55) Zhou, X.; Chen, Z.; Qu, Y.; Su, Q.; Yang, X. *RSC Adv.* **2013**, *3* (13), 4254–4260.

- (56) Kim, D. H.; Lee, H. S.; Shin, H.-J.; Bae, Y.-S.; Lee, K.-H.; Kim, S.-W.; Choi, D.; Choi, J.-Y. *Soft Matter* **2013**, *9* (22), 5355–5360.
- (57) Gomez De Arco, L.; Zhang, Y.; Schlenker, C. W.; Ryu, K.; Thompson, M. E.; Zhou, C. *ACS Nano* **2010**, *4* (5), 2865–2873.
- (58) Hammer, B. A. G.; Bokel, F.; Hayward, R. C.; Emrick, T. *Chem. Mater.* **2011**, *23* (18), 4250–4256.
- (59) Loewe, R. S.; Ewbank, P. C.; Liu, J.; Zhai, L.; McCullough, R. D. *Macromolecules* **2001**, *34* (13), 4324–4333.
- (60) Li, X.; Cai, W.; An, J.; Kim, S.; Nah, J.; Yang, D.; Piner, R.; Velamakanni, A.; Jung, I.; Tutuc, E.; Banerjee, S. K.; Colombo, L.; Ruoff, R. S. *Science* **2009**, *324* (5932), 1312–1314.
- (61) Nieuwendaal, R. C.; Snyder, C. R.; DeLongchamp, D. M. *ACS Macro Lett.* **2014**, *3* (2), 130–135.
- (62) Koch, F. P. V.; Heeney, M.; Smith, P. *J. Am. Chem. Soc.* **2013**, *135* (37), 13699–13709.
- (63) Zhokhavets, U.; Gobsch, G.; Hoppe, H.; Sariciftci, N. S. *Thin Solid Films* **2004**, *451–452*, 69–73.
- (64) Thulstrup, E. W.; Thulstrup, P. W. *Acta Chim. Slov.* **2005**, *52*, 371–383.
- (65) Ma, Y.; Qi, B.; Ren, Y.; Ungar, G.; Hobbs, J. K.; Hu, W. *J. Phys. Chem. B* **2009**, *113* (41), 13485–13490.
- (66) *Handbook of Chemistry and Physics*, 95th ed.; Haynes, W. M., Thomas, B., Lide, D. R., Eds.; CRC Press, 2014.
- (67) Gerfin, T.; Grätzel, M. *J. Appl. Phys.* **1996**, *79* (3), 1722–1729.
- (68) Shokri, R.; Vonau, F.; Cranney, M.; Aubel, D.; Narladkar, A.; Isare, B.; Bouteiller, L.; Simon, L.; Reiter, G. *J. Phys. Chem. C* **2012**, *116* (40), 21594–21600.
- (69) Holdcroft, S. *J. Polym. Sci. Part B Polym. Phys.* **1991**, *29* (13), 1585–1588.
- (70) Abd Wahab, F.; Sulaiman, K.; Huang, N. M. *J. Electron. Mater.* **2013**, *42* (9), 2739–2742.
- (71) Mena-Osteritz, E.; Meyer, A.; Langeveld-Voss, B. M. W. B.; Janssen, R. A. J. R.; Meijer, E. W. E.; Bäuerle, P. *Angew. Chem. Int. Ed. Engl.* **2000**, *39* (15), 2679–2684.
- (72) Roman, B.; Bico, J. *J. Phys. Condens. Matter* **2010**, *22* (49), 493101–493116.
- (73) Savagatrup, S.; Makaram, A. S.; Burke, D. J.; Lipomi, D. J. *Adv. Funct. Mater.* **2014**, *24* (8), 1169–1181.
- (74) Lee, E.; Hammer, B.; Kim, J.-K.; Page, Z.; Emrick, T.; Hayward, R. C. *J. Am. Chem. Soc.* **2011**, *133* (27), 10390–10393.

- (75) Kouijzer, S.; Michels, J. J.; van den Berg, M.; Gevaerts, V. S.; Turbiez, M.; Wienk, M. M.; Janssen, R. A. J. *J. Am. Chem. Soc.* **2013**, *135* (32), 12057–12067.
- (76) Güldal, N. S.; Kassar, T.; Berlinghof, M.; Unruh, T.; Brabec, C. J. *J. Mater. Res.* **2017**, *32* (10), 1855–1879.
- (77) Koerner, C.; Elschner, C.; Miller, N. C.; Fitzner, R.; Selzer, F.; Reinold, E.; Bäuerle, P.; Toney, M. F.; McGehee, M. D.; Leo, K.; Riede, M. *Org. Electron. physics, Mater. Appl.* **2012**, *13* (4), 623–631.
- (78) Krebs, F. C. *Sol. Energy Mater. Sol. Cells* **2009**, *93* (4), 394–412.
- (79) Diao, Y.; Myerson, A. S.; Hatton, T. A.; Trout, B. L. *Langmuir* **2011**, *27* (9), 5324–5334.
- (80) Treat, N. D.; Nekuda Malik, J. A.; Reid, O.; Yu, L.; Shuttle, C. G.; Rumbles, G.; Hawker, C. J.; Chabinyk, M. L.; Smith, P.; Stingelin, N. *Nat. Mater.* **2013**, *12* (7), 628–633.
- (81) Bu, L.; Pentzer, E.; Bokel, F.; Emrick, T.; Hayward, R. *ACS Nano* **2012**, No. 12, 10924–10929.
- (82) Liu, J.; Moo-Young, J.; McInnis, M.; Pasquinelli, M. A.; Zhai, L. *Macromolecules* **2014**, *47* (2), 705–712.
- (83) Acevedo-Cartagena, D. E.; Zhu, J.; Trabanino, E.; Pentzer, E.; Emrick, T.; Nonnenmann, S. S.; Briseno, A. L.; Hayward, R. C. *ACS Macro Lett.* **2015**, *4* (5), 483–487.
- (84) Yu, F.; Kuppala, V. K. *Mater. Lett.* **2013**, *99*, 72–75.
- (85) Skrypnichuk, V.; Boulanger, N.; Yu, V.; Hilke, M.; Toney, M. F.; Barbero, D. R. *J. Mater. Chem. C* **2016**, *4* (19), 4143–4149.
- (86) Ma, X.; Guo, Y.; Wang, T.; Su, Z. *J. Chem. Phys.* **2013**, *139* (1), 14701.
- (87) Grévin, B.; Rannou, P.; Payerne, R.; Pron, A.; Travers, J. P. *Adv. Mater.* **2003**, *15* (11), 881–884.
- (88) Grévin, B.; Rannou, P.; Payerne, R.; Pron, A.; Travers, J. P. *J. Chem. Phys.* **2003**, *118* (15), 7097.
- (89) Kim, D. H.; Han, J. T.; Park, Y. D.; Jang, Y.; Cho, J. H.; Hwang, M.; Cho, K. *Adv. Mater.* **2006**, *18* (6), 719–723.
- (90) Guo, Y.; Ma, X.; Su, Z. *Macromolecules* **2013**, *46* (7), 2733–2739.
- (91) Kraack, H.; Deutsch, M.; Sirota, E. B. *Macromolecules* **2000**, *33* (16), 6174–6184.
- (92) Pak, J.; Wunderlich, B. *Macromolecules* **2001**, *34* (13), 4492–4503.
- (93) Strobl, G. *Prog. Polym. Sci.* **2006**, *31* (4), 398–442.
- (94) Meyer, H.; Müller-Plathe, F. *J. Chem. Phys.* **2001**, *115* (17), 7807.

- (95) Kraack, H.; Sirota, E. B.; Deutsch, M. *Polymer (Guildf)*. **2001**, *42* (19), 8225–8233.
- (96) *Polymer Crystallization*; Reiter, G., Sommer, J.-U., Eds.; Lecture Notes in Physics; Springer Berlin Heidelberg: Berlin, Heidelberg, 2003; Vol. 606.
- (97) Kim, J.-S.; Kim, J.-H.; Lee, W.; Yu, H.; Kim, H. J.; Song, I.; Shin, M.; Oh, J. H.; Jeong, U.; Kim, T.-S.; Kim, B. J. *Macromolecules* **2015**, *48* (13), 4339–4346.
- (98) Remy, R.; Weiss, E. D.; Nguyen, N. A.; Wei, S.; Campos, L. M.; Kowalewski, T.; Mackay, M. E. *J. Polym. Sci. Part B Polym. Phys.* **2014**, *52* (22), 1469–1475.
- (99) Liu, J.; Loewe, R. S.; McCullough, R. D. *Macromolecules* **1999**, *32* (18), 5777–5785.
- (100) Avrami, M. *J. Chem. Phys.* **1939**, *7* (12), 1103–1112.
- (101) Hiemmenz, P. C.; Lodge, T. P. *Polymer Chemistry, Second Edition - CRC Press Book*, 2nd ed.; CRC Press, 2007.
- (102) Malik, S.; Nandi, A. K. *J. Polym. Sci. Part B Polym. Phys.* **2002**, *40* (18), 2073–2085.
- (103) Yang, Z.; Lu, H. *J. Appl. Polym. Sci.* **2013**, *128* (1), 802–810.
- (104) Luo, Y.; Santos, F. A.; Wagner, T. W.; Tsoi, E.; Zhang, S. *J. Phys. Chem. B* **2014**, *118* (22), 6038–6046.
- (105) Van Houselt, A.; Zandvliet, H. J. W. *Rev. Mod. Phys.* **2010**, *82* (2), 1593–1605.
- (106) Canet-Ferrer, J.; Coronado, E.; Forment-Aliaga, A.; Pinilla-Cienfuegos, E. *Nanotechnology* **2014**, *25* (39), 395703.
- (107) Kayunkid, N.; Uttiya, S.; Brinkmann, M. *Macromolecules* **2010**, *43* (11), 4961–4967.
- (108) Yu, M.; Ren, X.; Ma, L.; Wu, Y. *Nat. Commun.* **2014**, *5*, 5111.
- (109) Mena-Osteritz, E. *Adv. Mater.* **2002**, *14* (8), 609.
- (110) Wunderlich, B. In *Macromolecular Physics*; Elsevier, 1973; pp 178–379.
- (111) Ishii, H.; Sugiyama, K.; Ito, E.; Seki, K. *Adv. Mater.* **1999**, *11* (8), 605–625.
- (112) Duhm, S.; Heimel, G.; Salzmann, I.; Glowatzki, H.; Johnson, R. L.; Vollmer, A.; Rabe, J. P.; Koch, N. *Nat. Mater.* **2008**, *7* (4), 326–332.
- (113) Tsoi, W. C.; Spencer, S. J.; Yang, L.; Ballantyne, A. M.; Nicholson, P. G.; Turnbull, A.; Shard, A. G.; Murphy, C. E.; Bradley, D. D. C.; Nelson, J.; Kim, J.-S. *Macromolecules* **2011**, *44* (8), 2944–2952.
- (114) DeLongchamp, D. M.; Kline, R. J.; Fischer, D. a; Richter, L. J.; Toney, M. F. *Adv. Mater.* **2011**, *23* (3), 319–337.
- (115) Kim, D. H.; Jang, Y.; Park, Y. D.; Cho, K. *Langmuir* **2005**, *21* (8), 3203–3206.
- (116) Wang, S.; Tang, J.-C.; Zhao, L.-H.; Png, R.-Q.; Wong, L.-Y.; Chia, P.-J.; Chan, H. S. O.;



- Ho, P. K.-H.; Chua, L.-L. *Appl. Phys. Lett.* **2008**, *93* (16), 162103.
- (117) Miller, N. C.; Sweetnam, S.; Hoke, E. T.; Gysel, R.; Miller, C. E.; Bartelt, J. A.; Xie, X.; Toney, M. F.; McGehee, M. D. *Nano Lett.* **2012**, *12* (3), 1566–1570.
- (118) Menard, E.; Meitl, M. A.; Sun, Y.; Park, J. U.; Shir, D. J. L.; Nam, Y. S.; Jeon, S.; Rogers, J. A. *Chemical Reviews*. American Chemical Society 2007, pp 1117–1160.
- (119) Xu, W.; Hu, Z.; Liu, H.; Lan, L.; Peng, J.; Wang, J.; Cao, Y. *Sci. Rep.* **2016**, *6* (July), 1–7.
- (120) Yang, J.; Yan, D.; Jones, T. S. *Chem. Rev.* **2015**, *115* (11), 5570–5603.
- (121) Jo, S. B.; Kim, H. H.; Lee, H.; Kang, B.; Lee, S.; Sim, M.; Kim, M.; Lee, W. H.; Cho, K. *ACS Nano* **2015**, *9* (8), 8206–8219.
- (122) Wang, Y.; Torres, J. A.; Stieg, A. Z.; Jiang, S.; Yeung, M. T.; Rubin, Y.; Chaudhuri, S.; Duan, X.; Kaner, R. B. *ACS Nano* **2015**, *9* (10), 9486–9496.
- (123) Liu, S.; Wang, W. M.; Briseno, A. L.; Mannsfeld, S. C. B.; Bao, Z. *Adv. Mater.* **2009**, *21* (12), 1217–1232.
- (124) Hamilton, R.; Smith, J.; Ogier, S.; Heeney, M.; Anthony, J. E.; McCulloch, I.; Veres, J.; Bradley, D. D. C.; Anthopoulos, T. D. *Adv. Mater.* **2009**, *21* (10–11), 1166–1171.
- (125) Dimitrakopoulos, C. D.; Malenfant, P. R. L. *Adv. Mater.* **2002**, *14* (2), 99–117.
- (126) Tsao, H. N.; Müllen, K. *Chem. Soc. Rev.* **2010**, *39* (7), 2372–2386.
- (127) *P3HT Revisited – From Molecular Scale to Solar Cell Devices*; Ludwigs, S., Ed.; Advances in Polymer Science; Springer Berlin Heidelberg: Berlin, Heidelberg, 2014; Vol. 265.
- (128) Huang, W.; Markwart, J. C.; Briseno, A. L.; Hayward, R. C. *ACS Nano* **2016**, *10* (9), 8610–8619.
- (129) Kim, D. H.; Park, Y. D.; Jang, Y.; Yang, H.; Kim, Y. H.; Han, J. I.; Moon, D. G.; Park, S.; Chang, T.; Chang, C.; Joo, M.; Ryu, C. Y.; Cho, K. *Adv. Funct. Mater.* **2005**, *15* (1), 77–82.
- (130) Guo, Y.; Jiang, L.; Ma, X.; Hu, W.; Su, Z. *Polym. Chem.* **2013**, *4* (16), 4308.
- (131) Bae, S.; Kim, H.; Lee, Y.; Xu, X.; Park, J.-S.; Zheng, Y.; Balakrishnan, J.; Lei, T.; Kim, H. R.; Song, Y. Il; Kim, Y.-J.; Kim, K. S.; Ozyilmaz, B.; Ahn, J.-H.; Hong, B. H.; Iijima, S. *Nat. Nanotechnol.* **2010**, *5* (8), 574–578.
- (132) Liang, Y. T.; Hersam, M. C. *J. Am. Chem. Soc.* **2010**, *132* (50), 17661–17663.
- (133) Hyun, W. J.; Secor, E. B.; Hersam, M. C.; Frisbie, C. D.; Francis, L. F. *Adv. Mater.* **2015**, *27* (1), 109–115.
- (134) Søndergaard, R. R.; Hösel, M.; Krebs, F. C. *J. Polym. Sci. Part B Polym. Phys.* **2013**, *51* (1), 16–34.

- (135) Kim, H. H.; Chung, Y.; Lee, E.; Lee, S. K.; Cho, K. *Adv. Mater.* **2014**, *26* (20), 3213–3217.
- (136) Tiwari, S.; Takashima, W.; Balasubramanian, S. K.; Miyajima, S.; Nagamatsu, S.; Pandey, S. S.; Prakash, R. *Jpn. J. Appl. Phys.* **2014**, *53* (2), 21601.
- (137) Kalita, G.; Wakita, K.; Umeno, M.; Hayashi, Y.; Tanemura, M. In *2012 38th IEEE Photovoltaic Specialists Conference*; IEEE, 2012; pp 003137–003141.
- (138) Wang, Y.; Tong, S. W.; Xu, X. F.; Ozyilmaz, B.; Loh, K. P. *Adv. Mater.* **2011**, *23* (13), 1514–1518.
- (139) Osella, S.; Cornil, D.; Cornil, J. *Phys. Chem. Chem. Phys.* **2014**, *16* (7), 2866–2873.
- (140) Kim, J. S.; Park, J. H.; Lee, J. H.; Jo, J.; Kim, D.-Y.; Cho, K. *Appl. Phys. Lett.* **2007**, *91* (11), 112111.
- (141) Kim, H. J.; Skinner, M.; Yu, H.; Oh, J. H.; Briseno, A. L.; Emrick, T.; Kim, B. J.; Hayward, R. C. *Nano Lett.* **2015**, *15* (9), 5689–5695.
- (142) Kwon, K. C.; Dong, W. J.; Jung, G. H.; Ham, J.; Lee, J.-L.; Kim, S. Y. *Sol. Energy Mater. Sol. Cells* **2013**, *109*, 148–154.
- (143) Lock, E. H.; Delongchamp, D. M.; Schmucker, S. W.; Simpkins, B.; Laskoski, M.; Mulvaney, S. P.; Hines, D. R.; Baraket, M.; Hernandez, S. C.; Robinson, J. T.; Sheehan, P. E.; Jaye, C.; Fisher, D. A.; Walton, S. G. *Carbon N. Y.* **2015**, *86*, 288–300.